

EXPERIMENTAL MEASUREMENT OF THERMAL  
CHARACTERISTICS OF TWO-PHASE SEGMENTED  
FLOW IN MINICHANNEL HEAT SINKS

NICHOLAS GILL JANES







# **Experimental Measurement of Thermal Characteristics of Two-Phase Segmented Flow in Minichannel Heat Sinks**

A thesis  
submitted to the Memorial University of Newfoundland  
in fulfilment of the requirements for the degree of

Master  
In  
Mechanical Engineering

2013

by

©Nicholas Gill Janes

# Abstract

Experiments were conducted to measure the heat transfer characteristics of non-boiling two-phase segmented flow in two different miniature heat sinks. The heat sinks were manufactured to have a square wave flow path (termed Square Sink) and a spiral flow path (termed Spiral Sink).

The working fluids used in the experiments were water, canola oil and air. Single phase water and oil were examined first, and the results were used as a basis for comparison of the two-phase flow results. Two-phase flow experiments using water-air and oil-air were then conducted. The flow rates of the water-air and oil-air phases were varied between a range of values during each experiment and the system pressure and temperatures were recorded at each combination of flow rates.

The experimental data was used to calculate the value of dimensionless heat transfer  $q^*$  and dimensionless length  $L^*$ , which were used to compare the thermal performance from each experiment. The two-phase flow experiments for the square heat sink resulted in a dimensionless heat transfer enhancement of 24% for water-air containing long liquid slugs, 39.5% for water-air containing short liquid slugs and 1% for oil-air. The two-phase flow experiments for the spiral heat sink resulted in a dimensionless heat transfer enhancement of 14% for water-air containing short slugs.

The effects of liquid slug length and void fraction were examined. The effect of liquid slug length was shown to increase the dimensionless heat transfer as the slug length decreased. The effect of void fraction was found to be a controlling factor due to its impact on liquid slug length, which in turn affects dimensionless heat transfer. Finally the efficiencies of the square sink and spiral sinks were compared and it was shown that the spiral sink was most efficient when power requirements are considered.

# Acknowledgements

First and foremost I would like to thank my supervisor, Professor Yuri Muzychka. This body of work would not have been possible without his support, guidance, supervision, useful suggestions and especially his patience. His passion and enthusiasm in the area of micro-fluidics made this work enjoyable and interesting.

I would also like to thank my parents Harold Janes and Daphne Gill, my brother Christian Janes and my friends John and Alanna Downton. These people supported me throughout my studies and encouraged me when I needed it.

This work was supported by Natural Sciences and Engineering Research Council of Canada (NSERC). I am appreciative for the support given by this organization.

**To my grandfather, Sam Gill**

# Table of Contents

<b>Abstract</b>	i
<b>Acknowledgements</b>	ii
<b>List of Tables</b>	4
<b>List of Figures</b>	5
<b>Nomenclature</b>	7
<b>Chapter 1 – Introduction</b>	11
1.1 Introduction	11
1.2 Two-Phase Flow	11
1.3 Flow Patterns and Flow Maps	12
1.4 Segmented Flow	13
1.5 Mini-channel Heat Sinks	15
1.6 Research Objectives	16
1.7 Thesis Outline	17
<b>Chapter 2 – Literature Review</b>	18
2.1 Introduction	18
2.2 Literature Review	18
<b>Chapter 3 – Experimental Methods</b>	42
3.1 Introduction	42
3.2 Experimental Objectives	42
3.3 Miniature Heat Sinks	43
3.4 Experimental Apparatus, Assembly, and Operation	45
3.4.1 Introduction	45
3.4.2 Experimental Apparatus	45
3.4.2.1 Pumps	45

3.4.2.2 Thermocouples	46
3.4.2.3 Pressure Transducers	47
3.4.2.4 Heaters	48
3.4.2.5 Power Supply	48
3.4.2.6 Hydraulic Components	49
3.4.2.7 Data Acquisition System	50
3.4.2.8 Camera	50
3.4.2.9 Fluids	51
3.4.3 Experimental Assembly	52
3.4.4 Experimental Operation	55
3.5 Experimental Procedure	56
3.6 Sensor Calibration	58
3.6.1 Thermocouple Calibration	58
3.6.2 Pressure Transducer Calibration	58
3.6.3 Thermal Resistance Check	60
3.7 Experimental Uncertainty	61
3.8 Summary	65
<b>Chapter 4 – Experimental Results</b>	<b>66</b>
4.1 Introduction	66
4.2 Data Reduction	66
4.3 Experimental Results	72
4.3.1 Introduction	72
4.3.2 Square Sink Results	72
4.3.3 Spiral Sink Results	81
4.3.4 Effect of Slug Length	88
4.3.5 Effect of Flow Direction in Spiral Sink	90
4.3.6 Comparison of Single and Two-Phase Flow	92
4.3.7 Effect of Void Fraction	95
4.3.8 Effect of Liquid Film Thickness	97

4.3.9 Comparison of the Square Sink and Spiral Sink	99
4.4 Summary	101
<b>Chapter 5 – Conclusion and Recommendations</b>	102
5.1 Summary of Present Study	102
5.2 Recommendations for Future Work	103
<b>References</b>	106
<b>Appendix A – Heat Sink Technical Drawings</b>	112
<b>Appendix B – Experimental Plots</b>	117

## List of Tables

Table 2.1 – Values of Chisholm Constant C .....	22
Table 3.1 – Ice Bath Thermocouple Calibration Results .....	58
Table 3.2 – PX409-005DWU5V Pressure Transducer Calibration Worksheet .....	60
Table 3.3 – Uncertainty in Experimental Measurements .....	61
Table 3.4 – Calculated Uncertainty in Parameters .....	65
Table 4.1 – Effect of Slug Length on Heat Transfer Enhancement .....	89
Table 4.2 – Comparison of Single and Two-Phase Flow .....	93
Table 4.3 – Liquid Film Thickness and Thermal Boundary Layer Thickness for Oil-Air Segmented Flow in Square Sink .....	97
Table 4.4 – Liquid Film Thickness and Thermal Boundary Layer Thickness for Water-Air Segmented Flow in Square Sink .....	98





# Nomenclature

$A$	Area, $m^2$
$A_s$	Surface area, $m^2$
$C$	Chisholm constant
$C$	Model constant – Eq. (2.31)
$Ca$	Capillary number = $V_1\mu_1/\sigma$
$c$	Concentration, $mol/m^3$ – Eq. (2.11), (2.12), (2.13)
$c$	Capacitance, F – Eq. (2.25), (2.26), (2.27)
$c_p$	Heat capacity, $J/kg\cdot K$
$D$	Diameter, m
$D_h$	Hydraulic diameter, m
$dp/dz$	Pressure gradient, $Pa/m$
$f$	Fanning friction factor
$G$	Mass flux, $kg/m^2\cdot s$
$Gz$	Graetz number = $(\pi/4) Re Pr (D/L)$
$h$	Heat transfer coefficient, $W/m^2\cdot K$
$H$	Channel height, m
$J$	Rate of transfer, $mol/m$
$k$	Thermal conductivity, $W/m\cdot K$
$L$	Channel length, m
$L^*$	Dimensionless length
$\dot{m}$	Mass flow rate, $kg/s$
$Nu$	Nusselt number = $h/k$
$Nu_{fr}$	Nusselt number for fully developed flow
$n$	Droplet ratio – Eq. (2.26), (2.27)
$n$	Blending parameter – Eq. (2.43)
$P$	Power, W
$\Delta P$	Differential pressure, Pa
$\Delta P^*$	Normalized pressure

$p$	Fitting parameter
$Pe$	Peclet number = $Re Pr$
$Pr$	Prandtl number, = $\mu c_p / k$
$Q$	Flow rate, $m^3/s$
$q$	Heat transfer rate, W
$q^*$	Dimensionless heat transfer
$r$	Radius, m
$R$	Result – Eq. (3.5) to (3.17)
$R$	Resistance, $\Omega$ – Eq. (3.1)
$R^*$	Coiled aspect ratio = $D_i/D_c$
$R_L$	Liquid holdup
$Re$	Reynolds number = $\rho V D_H/\mu_m$
$T$	Temperature, K
$u$	Velocity, m/s
$V$	Voltage, V - Eq. (2.25), (3.1)
$W$	Channel width, m
$w_R$	Uncertainty in results – Eq. (3.5) to (3.17)
$x$	Mass quality
$x_i$	Independent measured quantity – Eq. (3.5) to (3.17)
$X$	Lockhart-Martinelli parameter
$z^*$	Dimensionless position for thermally developing flow

### Greek Symbols

$\phi_l$	Liquid two-phase flow multiplier
$\phi_g$	Gas two-phase flow multiplier
$\alpha_l$	Liquid fraction
$\alpha_g$	Void fraction
$\varepsilon$	Aspect ratio
$\gamma$	Shape factor

$\zeta$	Arbitrary length scale
$\rho$	Density, kg/m <sup>3</sup>
$\delta$	Film thickness, m
$\delta_t$	Thermal boundary layer thickness, m
$\mu$	Dynamic viscosity, N·s/m <sup>2</sup>

### Subscripts

<i>a, ave</i>	Average
<i>b</i>	Bubble
<i>c</i>	Coil
<i>CH3</i>	Thermocouple channel 3
<i>CH4</i>	Thermocouple channel 4
<i>CH5</i>	Thermocouple channel 5
<i>CH6</i>	Thermocouple channel 6
<i>drop</i>	Droplet
<i>Dev</i>	Developed flow region
<i>Ent</i>	Entrance region
<i>eq</i>	Equivalent
<i>g</i>	Gas phase
<i>i</i>	Inlet
<i>l</i>	Liquid phase
<i>lower</i>	Lower bound
<i>ln</i>	Logarithmic mean
<i>LS</i>	Liquid slug
<i>o</i>	Outlet
<i>p</i>	Graetz plug flow
<i>SP</i>	Single-phase
<i>s</i>	Slug flow
<i>sur</i>	Surroundings

*TP* Two-phase  
*t* Tube  
*upper* Upper bound  
*w* Wall  
*x* Local value

# **Chapter – 1**

## **Introduction**

### **1.1 Introduction**

This thesis is related to experimental work examining the potential heat transfer characteristics of non-boiling two-phase segmented flow in mini-channel heat sinks. In this application gas-liquid segmented flows are studied and the thermal performance of these flows is compared to that of continuous single phase flow. The working fluids are water, canola oil and air. Water-air and oil-air combinations have been examined. Two specifically designed heat sinks were tested with the combinations of fluids listed above. The first was a square pattern heat sink and the second was a spiral pattern heat sink. The resulting dimensionless heat transfer data for two-phase segmented flow in these heat sinks are compared to single phase data to assess the performance of this mode of operation on the overall convective heat transfer rate.

### **1.2 Two-Phase Flow**

In fluid mechanics, two-phase flow occurs in a system containing two phases (usually gas-liquid) with a meniscus (or interface) separating the two phases. However, two-phase flow is not limited to just gas-liquid flows, it can also refer to solid-liquid, solid-gas, or liquid-liquid flows. The latter being the case of two immiscible liquids (i.e. water and oil). Two-phase flows have numerous applications and occur in chemical industry processes, petroleum industry processes, refrigeration and air-conditioning processes, bio-medical systems, etc. The fluid system may be macro-scale, mini-scale, or micro-scale depending upon the application. Recently two-phase flows have found use in many microfluidic systems such as LOC (lab-on-a-chip) devices, MEMS (micro

electromechanical systems) and nanofluidic systems. A great deal of research has been conducted over the past sixty years on two-phase flow. Initial research focused on macro-scale flows while recent research focused on micro-scale and mini-scale flows. However, almost always, the research on two-phase flow concentrated on classification of flow, via flow patterns and flow mapping, correlations for frictional pressure drop, and correlations for modes of transport (heat and mass).

Many models have been developed analytically and theoretically to predict the two-phase frictional pressure drop and transport characteristics. These parameters are of importance to engineers working with two-phase flow systems. The models for two-phase flow can be classified into two separate categories: homogenous flow models and separated flow models. The homogenous flow model uses effective fluid properties that are determined from the properties of both phases in the flow. Properties such as viscosity and density are determined through effective property models, then the frictional pressure drop and transport characteristics are calculated using equations for single phase flow. Often times the homogenous flow model is referred to as zero-slip flow model. The separated flow model approach tries to account for the fact that both phases have different thermophysical properties and flow with different velocities. Often the separated flow model approach is termed the slip solution.

### **1.3 Flow Patterns and Flow Maps**

Many tools have been developed through theory and experimental research to help with the classification of two-phase flow. Flow patterns and flow maps are two fundamental examples of such tools. A flow pattern is used to identify the state of a two-phase flow at a given instant. Examples of different observed flow patterns are: bubbly flow, annular flow, churn flow, plug flow (Taylor flow) and stratified flow. Each flow pattern visually appears much different from the rest but the transition regions from one pattern to the next are harder to identify. Several different flow patterns that occur during two-phase flow are illustrated in Figure 1.1.

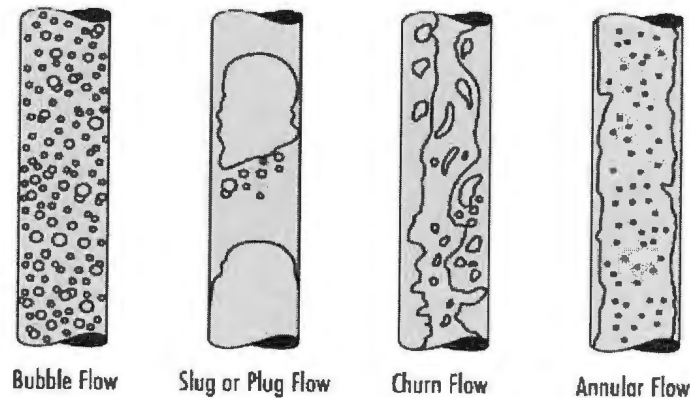


Figure 1.1 – Several two-phase flow patterns. [www.waterworld.com]

A flow map is used to predict the type of flow pattern that would occur as a result of the phase velocities and system geometry. The flow map has a major disadvantage in that it is not universal across systems and they usually vary from one publication to another due to issues related to micro-channel geometries. Kawaji and Chung (2004) developed several flow maps for circular and square micro-channels containing two-phase gas-liquid flow. Recently, Hassan et al. (2005) compared a number of flow map transition criteria using 1475 experimental data points and proposed universal flow maps for horizontal and vertical micro-channels. Four types of flow patterns were identified in this universal flow map: bubbly flow, intermittent flow, churn flow and annular flow. The intermittent flows are dominated by surface tension effects. Such flow patterns are known today as plug flow, slug flow and segmented flow. The universal flow map developed by Hassan et al. (2005) can be considered the best predictor of flow patterns in micro-channels and mini-channels.

### 1.4 Segmented Flow

Two-phase segmented flow is a flow pattern that has been examined extensively over the past ten years. It is characterized by splitting the fluid stream up into a series of shorter elements or plugs. One phase is termed the carrier or base fluid while the second phase is termed the segmenting media or dispersed phase. Many researchers refer to segmented gas-liquid flow as Taylor plug flow. This is due to the work of Taylor (1961) who

examined plug flows from the perspective of understanding film thickness and deposition at the wall. Traditionally, plug flow (Taylor flow) was the earliest form of the segmented flow pattern, but due to surface tension being a non-dominant factor in macro-scale studies at the time, it was near impossible to create a steady train of plugs with thin liquid film. However, as research shifted focus towards micro-scale systems where surface tension was a dominating factor, segmented flow became easy to produce and examine. A two-phase segmented flow of water-oil is illustrated in Figure 1.2. The water phase is dyed red to ease visual identification of each phase.

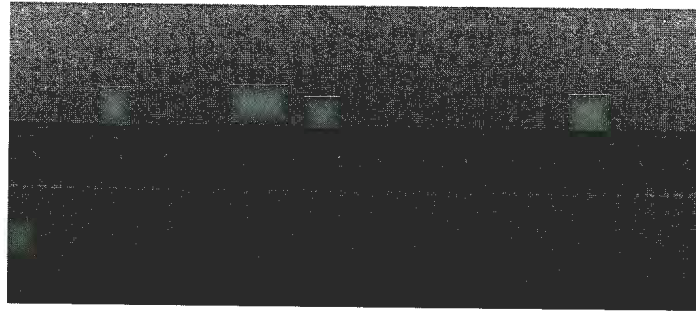


*Figure 1.2 – Two-phase segmented flow of water-oil.*

It has long been known that within liquid plugs of segmented flow, internal circulations arise as a result of gas-liquid, solid-liquid or liquid-liquid interfaces. These internal circulations are shown in Figure 1.3. It has been hypothesized that thermal enhancement occurs in segmented flows due to two different mechanisms. One mechanism is the internal circulations within the liquid plugs, while the other mechanism results from the increased velocity that the liquid plugs experience as a result of reduced liquid fraction for a constant mass flow rate. The latter was shown to be impossible by Muzychka et al. (2009) using simple heat transfer theory. This leaves only the internal circulation mechanism to explain the thermal enhancement resulting from segmented flow.

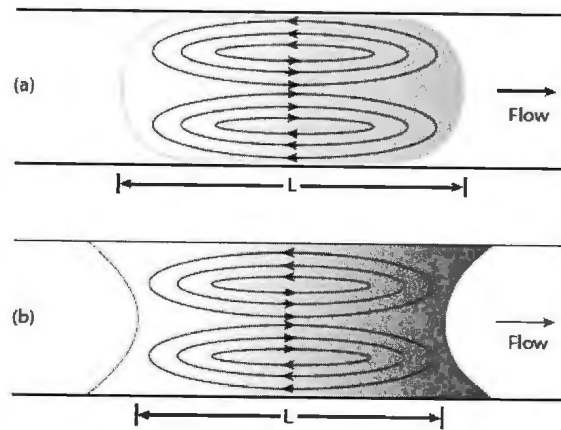


Figure 1.3 – Liquid plug internal circulations a) hydrophobic and b) hydrophilic [Muzychka et al. (2009)]

## 1.5 Mini-Channel Heat Sinks

Micro-scale and mini-scale devices have recently become a great topic of interest and were investigated by Wang et al. (1995), Zhang et al. (2002), Garimella et al. (2006) and Bahrami et al. (2008). The frictional pressure drop and transport characteristics of single phase flow in these devices were the focus of the above studies with the exception of Zhang et al. (2002) who examined boiling flows in micro-channels. For further information the reader is directed to Hassan (2008) who published an extensive review on progress made in this area in the past decade. It should be noted that to date no experimental studies have been conducted utilizing a two-phase segmented flow as a possible means of cooling a heated micro-scale or mini-scale device, i.e. heat sinks.

Two mini-channel heat sinks were designed and fabricated for the current study. The two different heat sink designs are illustrated in Figure 1.4. One heat sink was fabricated to have a square wave flow path. It contains a series of meandering channels with 90 degree bends. The second heat sink was fabricated to have a spiral flow path. This spiral has no 90 degree bends and falls under the coiled design methodology, which was examined by Horvath et al. (1973). The two heat sinks will be used to examine the thermal performance of using a segmented flow as the coolant. Also the thermal performance of

the spiral heat sink is to be compared to that of the square wave heat sink. These two designs have a 1mm x 1mm x 213mm channel geometry.

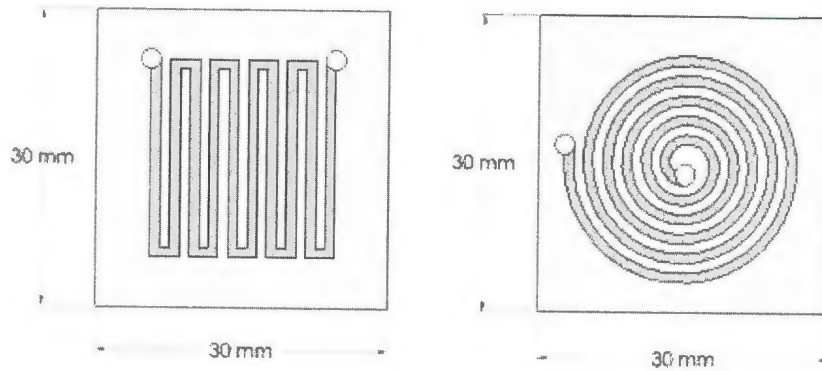


*Figure 1.4 – Mini-channel heat sinks: Square (left) and Spiral (right).*

## **1.6 Research Objectives**

The overall objective of the present study is to examine the thermal performance of non-boiling two-phase segmented flow used for cooling mini-channel heat sinks. Two-phase segmented flows of water-air and oil-air are to be conducted. The single phase flows of water and oil will be conducted, then the thermal performances of the segmented flows and the single phase flows will be compared. The thermal performance of the spiralling heat sink will be compared with the thermal performance of the square wave heat sink. Since no investigations to date have utilized two-phase segmented flow in mini-channel heat sinks, the results of such an investigation are both interesting and important.

In order to reach the overall research objective several smaller objectives must be clarified. Since the overall goal is to examine two-phase segmented flow, first preparations must be taken in order to generate steady uniform slug trains. This means one objective is to experiment with the generation of segmented flow. This objective requires two steps: research into how other investigators have successfully created

segmented flow and experimentation with the creation of segmented flow until the process is understood and can be reliably re-created.

Another research objective is the conceptual design and fabrication of the two mini-channel heat sinks. Since both heat sinks are to be compared considerations must be made so that the comparison process is fairly easy. Design parameters such as channel width and length are important factors as well as the material used. The exact way that the heat sinks will generate heat is also a concern for this objective to be met.

## **1.7 Thesis Outline**

This thesis contains five chapters. These are:

- Chapter 1 introduces the concept of using non-boiling two-phase segmented flow as a working fluid in mini-channel heat sink, presents a background on two-phase flow, flow patterns, flow mapping, mini-channel heat sinks and describes the research objectives for the present study.
- Chapter 2 provides a literature review of two-phase flow investigations spanning the last sixty years, focusing primarily on segmented flow research.
- Chapter 3 describes the design and fabrication of two mini-channel heat sinks, details the experimental setup and procedure, as well as calibration of equipment.
- Chapter 4 details the reduction of data into standard non-dimensional forms and presents the experimental results for the use segmented flow in cooling two mini-channel heat sinks.
- Chapter 5 summarizes the current study and presents recommendations for future work.

## Chapter – 2

### Literature Review

#### 2.1 Introduction

This chapter reviews the experimental and numerical research on general two-phase flows and two-phase segmented flows. The improvements to frictional pressure drop and transport correlations developed through research have been chronologically organized and presented here.

#### 2.2 Literature Review

Lockhart and Martinelli (1949) conducted two-phase flow experiments with air and liquids flowing inside pipes with varying diameters. The diameters ranged from 0.0586 inches to 1.017 inches and liquids including benzene, kerosene, water and various oils were considered. Four types of isothermal two-phase, two-component flow were identified, these were: turbulent liquid – turbulent gas, laminar liquid – turbulent gas, turbulent liquid – laminar gas, and laminar liquid – laminar gas. Lockhart and Martinelli (1949) correlate the two-phase pressure drop resulting from these four flow mechanisms to the Martinelli parameter  $X$  given in Eq. (2.1):

$$X^2 = \frac{\left(\frac{\Delta P}{L}\right)_l}{\left(\frac{\Delta P}{L}\right)_g} \quad (2.1)$$

Eq. (2.1) related the Martinelli parameter  $X$  to the ratio of both single phase pressure drops as if they were flowing in the pipe alone. Lockhart and Martinelli (1949) present their correlation graphically for all four of the flow mechanisms identified. Knowing the value of the Martinelli Parameter  $X$ , the Lockhart-Martinelli plots can be used to determine the two-phase flow multipliers for liquid and gas phases given by Eq. (2.2) and (2.3):

$$\phi_l^2 = \frac{\left(\frac{\Delta P}{L}\right)_{TP}}{\left(\frac{\Delta P}{L}\right)_l} \quad (2.2)$$

$$\phi_g^2 = \frac{\left(\frac{\Delta P}{L}\right)_{TP}}{\left(\frac{\Delta P}{L}\right)_g} \quad (2.3)$$

When the flow multiplier for either phase is determined, then the two-phase frictional pressure drop can be calculated using either Eq. (2.2) or (2.3), respectively. Additionally, Lockhart and Martinelli (1949) showed that the liquid fraction  $\alpha_l$  and void fraction  $\alpha_g$  are also correlated to the Martinelli parameter  $X$ . It should be noted that no design equations for predicting two-phase pressure drop were developed, only the graphical correlation was given.

Taylor (1961) conducted experiments examining plug flow from the perspective of understanding film thickness or fluid deposition at the wall of a tube. Fluids used consisted of Glycerine and strong sucrose solution (golden syrup) diluted with water till its viscosity was 28 poise at 20°C. Glass tubes with 2 mm and 3 mm internal diameter having lengths of 4 feet were used as test sections. A gas bubble was released into the test section and the amount of film left after the bubble had translated down the tube was measured.

Taylor's (1961) results were presented graphically by plotting parameter  $m$  (the liquid left in the tube) versus Capillary number. The experiments were conducted over a wide

range of Capillary number being  $0 < Ca < 2.0$ . It was clearly shown that as the Capillary number increased, so does the liquid film. The relationship is not linear and at higher values of Capillary number ( $Ca > 0.56$ ) the parameter  $m$  reaches a limiting value ( $m \approx 0.5$ ). Since Taylor's (1961) study, many researchers have referred to segmented gas-liquid flow as Taylor plug flow. An important characteristic identified by Taylor (1961) is the presence of a pair of circulation zones within liquid plugs. These zones result from the presence of the liquid/gas or liquid/liquid interface. The circulations affect the flow in a manner which promotes radial transport of heat and mass in addition to boundary layer renewal, since fresh fluid is constantly being transported to the leading edge of the liquid plug.

Oliver and Wright (1964) conducted a series of measurements to investigate the effect of plug flow on heat transfer and friction in laminar flow. They surmised that the internal circulation would increase the heat transfer coefficient significantly and therefore the Graetz-Leveque theory, Shah and London (1978), could not be applied to plug flow. The experiments consisted of single and two-phase flow within 0.25 inch test sections with lengths of 3 and 4 feet. The liquids used are 56.5% glycerol in water, 88% glycerol in water, 0.75% sodium carboxymethylcellulose (SCMC) in water, 1.5% SCMC in water, 0.5% Polyox in water and 2.0% Celacol solution. The gas used was air. The results are presented graphically as plots of Nusselt number versus Graetz number and the ratio of two-phase flow to single phase flow Nusselt number versus void fraction. Oliver and Wright (1964) concluded that the effect due to void fraction is independent of plug length but that circulation effects would be strongest for shorter plugs. It should be noted that Oliver and Wright (1964) attributed the increase in heat transfer coefficient to both the effects of internal circulations and increased liquid velocity. A simple model for two-phase plug flow heat transfer coefficient based upon experimental data and a modification of the Graetz-Leveque model was developed and given by Eq. (2.4):

$$Nu_{TP} = Nu_{SP} \left( \frac{1.20}{R_L^{0.36}} - \frac{0.20}{R_L} \right) \quad (2.4)$$

Hughmark (1965) developed a correlation for the estimation of hold-up (void fraction) in horizontal slug flow. This correlation was based on the relationship of bubble velocity and liquid slug Reynolds number. The bubble velocity during slug flow is reported by Hughmark (1965) as Eq. (2.5):

$$u_b = K_2 \left( \frac{Q_l + Q_g}{A} \right) \quad (2.5)$$

Where the variable  $K_2$  is a function of liquid Reynolds number and is reported to be constant with a value of 0.22 when the Reynolds number is greater than 400,000. Note that this would be well within the turbulent regime for the liquid phase. Hughmark (1965) gives the liquid Reynolds number as Eq. (2.6):

$$Re_l = \left( \frac{Q_l + Q_g}{A} \right) \frac{\rho_l}{\mu_l} \quad (2.6)$$

In addition to the correlation for void fraction in horizontal slug flow, Hughmark (1965) developed a simple model for slug flow heat transfer based upon the momentum-heat transfer analogy for turbulent flow and the Graetz-Leveque equation for laminar flow. The simple model developed is shown by Eq. (2.7):

$$\frac{h_{TP} D \sqrt{Re_l}}{k_l} = 1.75 \left( \frac{Q_l c_p}{R_L k_l L} \right)^{\frac{1}{3}} \left( \frac{\mu}{\mu_w} \right)^{0.14} \quad (2.7)$$

Hughmark (1965) compared the model given by Eq. (2.7) to the experimental data of Oliver and Wright (1964) and the average absolute deviation between experimental data and the model was found to be 8.4%.

Eighteen years after Lockhart and Martinelli's (1949) ground breaking correlation, Chisholm (1967) developed an equation for predicting two-phase frictional pressure drop. This is given by Eq. (2.8):

$$\phi_l^2 = 1 + \frac{C}{X} + \frac{1}{X^2} \quad (2.8)$$

Eq. (2.8) relates the two-phase multiplier for liquid to the Martinelli parameter, the mass quality and the constant C. The value of constant C depends on the type of flow and is summarized in Table 2.1.

**Table 2.1 – Values of Chisholm Constant C.**

Turbulent – Turbulent Flow	C = 20
Laminar – Turbulent Flow	C = 12
Turbulent – Laminar Flow	C = 10
Laminar – Laminar Flow	C = 5

Oliver and Young Hoon (1968) tested isothermal flow of Newtonian and non-Newtonian pseudoplastic fluids during slug flow. It is stated that circulation or streamline deflection exists inside the liquid slugs depending on the liquid film thickness around a bubble being greater or less than 0.294 R, where R is the radius of the pipe. Oliver and Young Hoon (1968) experimented by using 85% glycerol in water as Newtonian and 1.5% SCMC and 1.3% Polyox WSR 301 in water as two non-Newtonian fluids.

Slug flow and annular flow were developed in a 0.25 inch glass test section. To measure void fraction, quick-close valves were placed before and after this test section. These valves were simultaneously closed and the fraction of the tube occupied by trapped liquid after it had drained in the vertical position was measured. A camera was mounted on a movable platform so that slugs could be photographed. Graphite particles were

introduced as tracer particles. Oliver and Young Hoon (1968) report that the streamline pattern in Newtonian slug flow is characterized by a circulation while only streamline deflections occur in the non-Newtonian slug flows. The data obtained were compared to Lockhart and Martinelli's (1949) plots and satisfactory correlation was found for Newtonian fluids, but the two non-Newtonian cases fell well below the calculated values. Oliver and Young Hoon (1968) conducted several heat transfer experiments utilizing Newtonian and non-Newtonian fluids in slug flow and annular flow. Using the same fluids as previously mentioned, they were run through a heat exchanger test section with 0.25 inch ID. Outlet and inlet temperatures were measured, as well as six surface temperatures along the heat exchanger. Oliver and Young Hoon (1968) plotted the results as Graetz number versus Nusselt number. The definition for Graetz number and two-phase flow Reynolds number used are given by equations (2.9) and (2.10).

$$Gz = \frac{\pi}{4} Re_{TP} Pr \frac{D}{L} \quad (2.9)$$

$$Re_{TP} = \left( \frac{Q_l + Q_g}{A} \right) \frac{D\rho_l}{\mu_l} \quad (2.10)$$

One important aspect of Oliver and Young Hoon's (1968) experiment is that the liquid slug length was varied. Several liquid slug lengths were used for a given set of liquid and gas flow rates. The results show that for 85% glycerol solutions (i.e. Newtonian fluids) the heat transfer coefficient for short slugs was over 2.5 times higher than those obtained using long slugs. Therefore it was concluded that liquid slug length is a variable in controlling heat transfer in two-phase slug flow.

Horvath et al. (1973) conducted experiments measuring the radial transport in homogenous flow and two-phase slug flow. An open tubular heterogeneous enzyme reactor 60 cm long having a 2.32 mm internal diameter was utilized and a substrate solution was used as a working fluid. The length to diameter aspect ratio of this setup was  $L/D = 260$ . Homogenous flow experiments were conducted to measure the radial mass

transport to the substrate solution. Then an average Nusselt number for the single phase flow was calculated according to Eq. (2.11):

$$J = \overline{Nu} D \pi L c_{ln} \quad (2.11)$$

In Eq. (2.11),  $J$  is the overall rate of reaction,  $\overline{Nu}$  is the average Nusselt number,  $D$  is the tube diameter,  $L$  is the tube length, and  $c_{ln}$  is the logarithmic mean concentration of the reactant which is given by Eq. (2.12):

$$c_{ln} = \frac{(c_i - c_{w,i}) - (c_o - c_{w,o})}{\ln\left(\frac{c_i - c_{w,i}}{c_o - c_{w,o}}\right)} \quad (2.12)$$

After the homogenous flow experiments, Horvath et al. (1973) tested two-phase plug flows and measured the radial mass transport again. The average Nusselt number for the two-phase plug flow was calculated using a modified version of Eq. (2.11), given by Eq. (2.13):

$$J = \overline{Nu} D \pi L (1 - \varepsilon) c_{ln} \quad (2.13)$$

The variable introduced in Eq. (2.13) is the void fraction which Horvath et al. (1973) denotes as  $\varepsilon$  (normally denoted  $\alpha_g$  in a two-phase flow). It was found that when comparing the radial transport in plug flow to single phase flow for small values of Reynolds number, Schmidt number and dimensionless tube length, that the Nusselt number significantly increased. For  $30 < Re < 250$ , the Nusselt number in single phase flow is between 10 and 20. However, in plug flow with relatively long slugs the Nusselt number is 2 to 3 times higher than that of single phase flow. For slug flow with short slugs the Nusselt number was much higher reaching a value of 150 in the same range of Reynolds numbers. Horvath et al. (1973) compared the slug flow results to previous studies on turbulent flow conducted by Bennett and Myers (1962). The Nusselt number in

turbulent flow when Reynolds number had a value of 3000 was 100. Therefore the results indicate that radial mixing generated in plug flow approach those usually obtained only in turbulent flow.

In addition to the straight tube reactor experiments, Horvath et al. (1973) conducted experiments with homogenous and two-phase slug flow in a coiled reactor. The overall rate of reaction was measured, then a average Nusselt number was calculated, but for the coiled reactor the Nusselt number was also dependent upon the ratio of the tube diameter to the coiled diameter given by Eq. (2.14):

$$R^* = \frac{D_t}{D_c} \quad (2.14)$$

In Eq. (2.14), the variable  $D_t$  is the tube diameter,  $D_c$  is the coil diameter, and  $R^*$  is the coiled aspect ratio. Horvath et al. (1973) found that coiling the tube greatly increases the radial transport due to the presence of a secondary flow in the cross-sectional plane generated by centrifugal forces. Furthermore, it is reported that for plug flow in coiled tubes the two secondary flows (circulation within liquid plugs and circulation in the cross-sectional plane) act together synergetically. Due to the super-positioning of both flow patterns a double helical circulation results.

Horvath et al. (1973) reports that for relatively low Reynolds number and void fraction, coiling can yield 80-100% increase in average Nusselt number. The data are presented in a plot of average Nusselt number versus dimensionless plug length for both non-coiled and coiled experiments. It can be seen that for a dimensionless plug length value of 10, a straight tube reactor resulted in a average Nusselt number of 34, while the coiled tube reactor with a coiled aspect ratio of 0.012 resulted in a average Nusselt number of 64.

Vrentas et al. (1978) studied the characteristics of a plug flow field induced by solid spheres in a tube of liquid. This experimental study was among the first published detailing solid-liquid slug flow. Vrentas et al. (1978) states the principal disadvantage of

gas-liquid slug flows is that the plug flow field depends on the properties of both fluids and on other experimental variables. It becomes hard to create steady plug flows which fill up the entire cross-section of a tube, leaving a thin liquid film. Alternatively, the film thickness for solid-liquid slug flow can be controlled independently by choosing an appropriate sphere size in relation to the tube diameter. This is the major advantage of solid-liquid slug flow over gas-liquid plug flow.

The major disadvantages of solid-liquid plug flow are also reported by Vrentas et al. (1978). First, the increased pressure drop across the tube for liquid slugs of all sizes results in a increased power requirement. Therefore liquid film thickness and slug length must be chosen to optimize such a solid-liquid slug flow system. Second, provisions for recycling and maintenance of the spheres must be made where this is not a concern for gas-liquid systems.

Several theoretical assumptions are made by Vrentas et al. (1978) so that the analysis of the solid-liquid slug flow is equivalent to the calculation of the velocity and temperature fields in a cylindrical cavity with a uniformly translating wall. The Nusselt number is then defined for an ideal heat exchanger, as Eq. (2.15):

$$Nu = \frac{(h_a)_l D}{k} = \frac{Pe T_a r}{L(2 - T_a)} \quad (2.15)$$

In Eq. (2.15),  $T_a$  is the dimensionless average fluid temperature. Vrentas et al. (1978) utilized a horizontal heat exchanger, which was fed by a gear pump for experiments. The length to diameter aspect ratio of the setup was  $L/D = 128$ . Dow Corning 210 silicone oil was used as the working fluid. Two grades with 100 cSt and 1000 cSt viscosities were chosen. Stainless steel spheres were introduced after the pump at regulated intervals. The spheres and fluid flowed in a 0.95 cm ID tube and the spheres were sized so that there was less than a 0.0025 cm clearance between sphere and tube wall. A reciprocating piston was used to transfer the spheres between the exit and the entrance of the heat exchanger. Freon TF ( $CCl_2F-CClF_2$ ) vapour was utilized to maintain a constant wall temperature as

it condensed. The exit temperature of the fluid was not reliable when data were collected so all heat transfer coefficients reported by Vrentas et al. (1978) are based on heat flows deduced from measured condensation rates.

Vrentas et al. (1978) presents the experimental results graphically. Peclet number is plotted versus Nusselt number for a range of dimensionless plug lengths. The single phase flow of silicone oil is also plotted on this graph and the Nusselt number used for this flow was given by Eq. (2.16):

$$\text{Nu} = 1.62 \left( \text{Pe} \frac{D}{L} \right)^{\frac{1}{3}} \quad (2.16)$$

The plot ranges from  $4 < \text{Pe} < 18$  and 3 values for dimensionless slug length are shown, these values being 21, 77 and 122. For a value of Peclet number equal to 10, the single phase flow results in a Nusselt number of 6.90. For the same value of Peclet number the Nusselt numbers for 21, 77, and 122 dimensionless plug length values are 14.2, 17.0, and 19.9 respectively. It is clearly seen from the results that as dimensionless plug length decreases (i.e. making the liquid slugs shorter) the Nusselt number increases. Another interesting note is that for single phase flow the Nusselt number is a non-linear function of Peclet number, but for plug flows in this experiment, the Nusselt number had almost near linear relationship with Peclet number.

Muzychka and Yovanovich (2004) developed a general model for predicting the heat transfer coefficient in the combined entry region of non-circular ducts. The model was developed by combining the solution for a flat plate with a model developed for the Graetz flow problem. The model developed for the Graetz flow problem was developed by combining a model for fully developed flow with the Leveque approximation. The fully developed flow model is given in Eq. (2.17):

$$\text{Nu}_{\sqrt{A}} = c_1 \left( \frac{f \text{Re}_{\sqrt{A}}}{8\sqrt{\pi} \varepsilon^\gamma} \right) \quad (2.17)$$

In Eq. (2.17),  $c_1 = 3.24$  for uniform wall temperature (UWT) boundary condition and  $c_1 = 3.86$  for uniform wall flux (UWF) boundary condition. The parameter  $\gamma$  is chosen based on the channel geometry, although upper and lower bounds of this parameter are fixed at values of  $1/10$  and  $-3/10$ . The fully developed flow model predicted available data within a  $\pm 10\%$ . The Leveque approximation which is valid where the thermal boundary layer develops in the region near the wall where the velocity profile is linear is given by Eq. (2.18):

$$\text{Nu}_\zeta = c_2 c_3 \left( \frac{f \text{Re}_\zeta}{z^*} \right)^{\frac{1}{3}} \quad (2.18)$$

The model given by Eq. (2.18) predicts both average Nusselt and local Nusselt numbers. The value of  $c_2$  is 1 for local conditions and  $3/2$  for average conditions. The symbol  $\zeta$  indicates the dimensionless parameters are based on some arbitrary length scale. The value of  $c_3$  is 0.427 for UWT condition and 0.517 for UWF condition. Muzychka and Yovanovich (2004) combine Eq. (2.17) and (2.18) using the Churchill and Usagi (1972) asymptotic correlation method. This method resulted in a model predicting the Graetz flow problem and is given by Eq. (2.19):

$$\text{Nu}_{\sqrt{A}} = \left[ \left( c_2 c_3 \left( \frac{f \text{Re}_{\sqrt{A}}}{z^*} \right)^{\frac{1}{3}} \right)^5 + \left( c_1 \left( \frac{f \text{Re}_{\sqrt{A}}}{8\sqrt{\pi} \varepsilon^\gamma} \right) \right)^5 \right]^{\frac{1}{5}} \quad (2.19)$$

The values for all constants that appear in Eq. (2.19) are summarized in a table presented by Muzychka and Yovanovich (2004). The general model for predicting the heat transfer coefficient for the combined entry region is then developed by combining Eq. (2.19) with the solution for a flat plate. Applying the same asymptotic correlation as before, the general model is presented in Eq. (2.20):

$$\text{Nu}_{\sqrt{A}}(z^*) = \left[ \left( \frac{c_4 f(\text{Pr})}{\sqrt{z^*}} \right)^m + \left\{ c_2 c_3 \left( \frac{f \text{Re}_{\sqrt{A}}}{z^*} \right)^{\frac{1}{3}} \right\}^5 + \left\{ c_1 \left( \frac{f \text{Re}_{\sqrt{A}}}{8\sqrt{\pi \epsilon^\gamma}} \right) \right\}^5 \right]^{\frac{1}{m}} \quad (2.20)$$

The parameter  $m$ , in Eq. (2.20) is a function of Prandtl number and is given by Eq. (2.21).

$$m = 2.27 + 1.65 \text{Pr}^{\frac{1}{3}} \quad (2.21)$$

The general model developed and given by Eq. (2.20) is valid for  $0.1 < \text{Pr} < \infty$ ,  $0 < z^* < \infty$ , both uniform wall temperature (UWT) and uniform wall flux (UWF), and for local and average Nusselt numbers. Muzychka and Yovanovich (2004) compared the model to available data and the model agreed within  $\pm 15\%$  for most non-circular ducts.

Kreutzer et al. (2005) aimed to develop a pressure drop model for segmented flow (Taylor Flow) in capillaries that takes the plug and bubble length into account and allows the plug length to be determined from experimental pressure drop data. Experiments were conducted in a capillary tube with 2.3 mm internal diameter. A special inlet was constructed from a tapered channel and hypodermic needle which allowed the liquid plug and bubble lengths to be varied. Segmented flows consisting of air-water, air-decane, and air-tetradecane were examined. The gas and liquid superficial velocities were varied from 0.04 m/s to 0.3 m/s. Kreutzer et al. (2005) found numerically and experimentally that for plug flow with  $\text{Re} \gg 1$ , the extra pressure terms may be taken into account using the ratio of Capillary number to Reynolds number given as  $(\text{Ca}/\text{Re})$ . The model developed is given in Eq. (2.22):

$$f = \frac{16}{\text{Re}} \left( 1 + 0.17 \frac{1}{L_s^*} \left( \frac{\text{Ca}}{\text{Re}} \right)^{0.33} \right) \quad (2.22)$$

Additionally, Kreutzer et al. (2005) also modelled the plug flow numerically using the CFD code FIDAP. When numerical data was compared to the experimental data a correlation was constructed by replacing the 0.17 in Eq. (2.22) with 0.07. The difference

in experimental and numerical data is not attributed to experimental error, but is explained by the Marangoni effect which deals with impurities in the experimental fluids. Note that when Eq. (2.22) is used to model single phase flow, the  $L^*_s$  is equal to infinity and the right term in the brackets approaches zero. The model then becomes the Hagen - Poiseuille flow solution for laminar flow in a pipe given by Eq. (2.23):

$$f = \frac{16}{Re} \quad (2.23)$$

Lakehal et al. (2006) conducted computational microfluidics flow simulations to examine heat transfer in small tubes. The simulations were performed using the CMFD code TransAT<sup>®</sup> developed at ASCOMP. Three flow patterns were studied at various flow rates in a 1 mm internal diameter pipe, there were identified as: bubbly flow, slug flow, and bubbly-train slug. The wall condition was taken to be uniform wall temperature (UWT) and the flow pattern effects on heat transfer were studied. The wall temperature was set to 340 K and the inflow temperature was set to 300 K.

Results from Lakehal et al. (2006) show that the overall heat removal rate in two-phase flow is higher than in single phase flow. A simple model for two-phase slug flow heat transfer is presented and given by Eq. (2.24):

$$Nu \approx Nu_w + C Pr_l^{0.4} Re_{LS}^{\frac{4}{5}} \quad (2.24)$$

The  $Nu_w$  in Eq. (2.24) is the fully developed single phase Nusselt number which is 3.67 for uniform wall temperature (UWT) condition and 4.36 for uniform wall flux (UWF) condition.  $C$  in Eq. (2.24) is a model constant and has a value of 0.022. The model is valid for segmented flow in micro-scale devices where  $L \approx 0$  mm and  $Pr > 1$  liquids. Lakehal et al. (2006) describes the model in Eq. (2.24) as being a guideline to be used by engineers for design purposes.

Yu et al. (2007) conducted experiments and numerical simulations to examine bubble shape, size and formation mechanisms during segmented flow in micro-channels. These mechanisms were investigated for different flow rates, different mixer geometries, and varying Capillary numbers. Yu et al. (2007) examined two different mixer geometries. One was a cross-shaped mixer with liquid channels perpendicular to the main channel, while the other was a converging mixer, where liquid inlets were  $45^\circ$  to the main channel. All channels were square cross-section, with a  $125\ \mu\text{m}$  and  $250\ \mu\text{m}$  side length. The fluids used were air, sucrose solution with viscosity of 30 cP, glucose solution with viscosity of 60 cP, and mineral oil with a viscosity of 75 cP. Simulations were conducted using Lattice Boltzmann method (LBM). One advantage of this method is that for two-phase flows, the phase separation took place spontaneously in non-ideal fluid or between two immiscible fluid components, without the need to track the interface. The simulations were carried out in most cases using 600 grid points over the channel length, however to reduce simulation time 300 grid points were used for short channels. Yu et al. (2007) presented experimental and LBM simulation results visually as pictures for several combinations of flow rate and Capillary number. The combinations used were:  $Ca = 0.007$  with  $Q_g:Q_l = 1:1$ ,  $Ca = 0.017$  with  $Q_g:Q_l = 1:2$ , and  $Ca = 0.035$  with  $Q_g:Q_l = 1:4$ . The differences between the two mixer geometries are also shown visually as pictures. It is reported that larger gas to liquid flow rate ratio lead to longer gas bubbles. Maintaining the same flow rate ratio, but decreasing the Capillary number by changing fluids yielded a longer gas bubble. The mixer geometry had some effects on bubble length and spacing between bubbles. The converging channel geometry lead to longer liquid plugs between bubbles at  $Ca = 0.035$  with  $Q_g:Q_l = 1:4$  but the bubble size was similar in both cases. However, for the other two combinations of Capillary number and flow rate ratio, the converging channel mixer lead to longer gas bubbles and longer liquid plugs. Yu et al. (2007) states that the LBM simulation had discrepancies in the results when compared to experimental data investigating the mixer geometry. This was explained by the simulation being unable to completely capture the wetting conditions between the fluid and channel wall and the flow in narrow liquid film between the bubble and channel wall.

Mohseni and Baird (2007) investigated the use of electrowetting on dielectric (EWOD) as a driving force for a new method of cooling micro-devices that is termed digitized heat transfer (DHT). EWOD is used for transporting droplets of electrically conductive liquid metal alloys by the application of an electric field normal to the direction of flow. The EWOD force is generated by lining a micro-channel with electrodes and sequentially firing them such that a slugs leading edge is continually between grounded electrodes. Mohseni and Baird (2007) state this is a excellent way to generate two-phase segmented flow of liquid metal alloys which typically have orders of magnitude higher thermal conductivities than non-metallic liquids such as water and oils. The liquid metal alloy of Galinstan is suggested as an excellent candidate for a EWOD micro-cooling device since it is inexpensive, non-toxic, readily available, and has 65 times less thermal resistance than water. Mohseni and Baird (2007) derive simple equations for EWOD applications. One such simple equation is for EWOD droplet velocity given by Eq. (2.25):

$$\overline{u}_{\text{drop}} = \frac{cV^2 H}{24\mu L} \quad (2.25)$$

In Eq. (2.25),  $\overline{u}_{\text{drop}}$  is the average bulk velocity of a droplet,  $c$  is the capacitance per unit area of the dielectric layers,  $V$  is the applied voltage,  $H$  is the height of the channel and  $L$  is the length of the channel. Simple expressions for heat transfer characteristics for uniform wall temperature (UWT) and uniform wall flux (UWF) conditions are also presented. For the UWT condition the expression for overall heat transfer is given by Eq. (2.26):

$$q = \rho_l n V H W c (T_w - T_i) \quad (2.26)$$

In Eq. (2.26),  $n$  is the droplet ratio,  $W$  is the channel width, and  $\rho_l$  is the liquid metal alloys density. For the UWF condition an expression for outlet temperature is given by Eq. (2.27):

$$T_o = \frac{q_w}{\rho_l n V H W c} + T_i \quad (2.27)$$

Awad and Muzychka (2007) developed simple expressions for the upper and lower bounds for two-phase frictional pressure gradient in mini-channels and micro-channels. The lower bound is based on Ali et al. (1993) correlation for laminar-laminar flow which is given by Eq. (2.28):

$$\left(\frac{dp}{dz}\right)_{f,lower} = \frac{32G(1-x)\mu_l}{D^2\rho_l} \left[ 1 + \left(\frac{x}{1-x}\right) \left(\frac{\rho_l}{\rho_g}\right) \left(\frac{\mu_g}{\mu_l}\right) \right] \quad (2.28)$$

The upper bound is based on the Chisholm correlation for laminar-laminar flow and is given by Eq. (2.29):

$$\left(\frac{dp}{dz}\right)_{f,upper} = \frac{32G(1-x)\mu_l}{D^2\rho_l} \left[ 1 + 5\left(\frac{x}{1-x}\right)^{0.5} \left(\frac{\rho_l}{\rho_g}\right)^{0.5} \left(\frac{\mu_g}{\mu_l}\right)^{0.5} + \left(\frac{x}{1-x}\right) \left(\frac{\rho_l}{\rho_g}\right) \left(\frac{\mu_g}{\mu_l}\right) \right] \quad (2.29)$$

Awad and Muzychka (2007) then develop a average or mean bound based on the arithmetic mean of the lower bound and upper bound, this mean bound is given by equation (2.30).

$$\left(\frac{dp}{dz}\right)_{f,ave} = \frac{32G(1-x)\mu_l}{D^2\rho_l} \left[ 1 + 2.5\left(\frac{x}{1-x}\right)^{0.5} \left(\frac{\rho_l}{\rho_g}\right)^{0.5} \left(\frac{\mu_g}{\mu_l}\right)^{0.5} + \left(\frac{x}{1-x}\right) \left(\frac{\rho_l}{\rho_g}\right) \left(\frac{\mu_g}{\mu_l}\right) \right] \quad (2.30)$$

Note that the mean model given by Eq. (2.30) is equivalent to the Chisholm correlation with a value of  $C = 2.5$ . The mean model is then compared to published data graphically by plotting the two-phase flow multiplier for liquid versus the Martinelli parameter. Data published by Lee and Lee (2001), Chung and Kawaji (2004) and Kawaji et al. (2005) are plotted and the mean bound predicts the data with a root mean square (RMS) error of 17.91%, 19.29%, and 10.49%, respectively.

Fries et al. (2008) examined segmented flow in a rectangular micro-channel using Laser Induced Fluorescence (LIF) and confocal Laser Scanning Microscopy (LSM). The microfluidic channel used had a length of 2 m and a height equal to the width of  $200 \pm 2$   $\mu\text{m}$ . As fluids, ethanol, water, glycerol in aqueous solution at different concentrations and nitrogen were used. Fries et al. (2008) varied the flow rates from 20 - 60  $\mu\text{L}/\text{min}$  for the liquid phase and 30 - 100  $\mu\text{L}/\text{min}$  for the gas phase. The corresponding superficial velocities for these flow rates are 0.008 - 0.025 m/s for the liquid phase and 0.013 - 0.042 m/s for the gas phase. The liquid plug length, gas bubble length, pressure drop, and film thickness over the range of superficial velocities were examined.

Fries et al. (2008) reports that in analyzing the liquid plug lengths over the complete channel length resulted in constant plug length, except for ethanol. It was found that in general, the plug length increases with increasing superficial liquid velocity at a constant gas flow rate. When the gas bubble length was examined there was elongation of the bubbles due to the pressure drop in the channel. The gas bubble length is plotted graphically versus the reactor length for ethanol-nitrogen. It is shown that the gas bubble length depends on the pressure and for a constant superficial gas velocity of 0.042 m/s, on the superficial liquid velocity: an increase in the liquid flow rate results in a decrease of the gas bubble length. The gas bubble elongation is caused only by the pressure drop, no coalescence was observed in any experiment.

The pressure drop results are shown graphically as a plot of pressure drop versus the squared sum of superficial velocities. Increasing the velocity leads to an enhanced pressure drop, this increase in pressure drop is linear to the square of the sum of the superficial velocities. It is also shown that less viscous fluids give smaller pressure drop values than fluids with higher viscosity, which is to be expected. Fries et al. (2008) compares the measured pressure drop to six different models. The first three models are: homogenous model with fanning friction factor  $f = 16/\text{Re}$ , the Bretherton (1961) model and the Kreutzer et al. (2005) model which include correction factors for the extra pressure in plug flow. The homogenous model was shown to drastically under-predict the data while the Bretherton (1961) model was shown to describe the results best.

The Kreutzer et al. (2005) model under-predicted the data as well but the reason for this was Kreutzer et al. (2005) examined circular channels whereas the current study examined rectangular channels. In addition to these first three models, Fries et al. (2008) further compares pressure drop data to three models based on Lockhart and Martinelli (1949) theory. These three models are the Chisholm (1967) model, the Lee and Lee (2001) model and the Mishima (1996) model. It is shown that good agreements are made with models based on micro-channels whereas the models developed for macro-scale over-predict the pressure drop measurements.

Fries et al. (2008) measured the film thickness using LSM. The results for the film thickness measurements are compared graphically with correlations from literature including those proposed by Kreutzer et al (2005), Bretherton (1961) and Kolb and Cerro (1991). It was found that at higher Capillary number the gas bubbles elongate and the measurements are more comparable to literature. For smaller Capillary number ( $Ca < 0.001$ ) the corner film thickness is nearly independent from Capillary number. It was confirmed that for  $Ca < 0.01$  no significant change in film thickness occurred for reducing the Capillary number. This agreed with the measurements done by Kolb and Cerro (1991).

Narayanan and Lakehal (2008) examined the Nusselt number and pressure drop for bubble and plug flow through simulations conducted using the CMFD code TransAT<sup>®</sup> developed at ASCOMP. Simulations were performed under axisymmetric conditions for single and two-phase flows for zero-gravity, down-flow and up-flow configurations. The simulations were compared to experimental data produced by Chen et al. (2002) who investigated air-water two-phase flow at various flow speeds in a closed loop pipe having 1 mm and 1.5 mm internal diameter.

Narayanan and Lakehal (2008) report that for bubbly flow the average Nusselt number of 10.7 is obtained for all three cases with different orientations with respect to gravity. For plug flows, the average Nusselt number of 15 is obtained, however a discernible trend is

present with respect to gravity orientation. The down-flow case has a 4% higher average Nusselt number as compared to the zero-gravity case. The results are presented graphically by plotting local Nusselt number versus dimensionless channel length. For bubbly flow, the local Nusselt number smoothly goes through a maximum at the center of the bubble where the liquid layer is squeezed. For the plug flow, the maximum value of local Nusselt number occurs at the rear end of the plug where the gap between the interface and the wall is very small. Orientation with respect to gravity plays a role in shifting the location of breakup upstream for the up-flow case, which results in larger breakup frequency. However, the Nusselt numbers obtained are of similar magnitudes to those obtained by Monde and Mitsutake (1995) and Ua-Arayaporn et al. (2005). Overall the average Nusselt numbers from Narayanan and Lakehal (2008) simulations transport 3 to 4 times more heat than single phase flows. Furthermore, Narayanan and Lakehal (2008) propose a simple model for Nusselt number for practical applications. This model is given by Eq. (2.31):

$$\text{Nu} \approx \text{Nu}_w C \text{Pr}^{0.4} \text{Re}_{LS}^{\frac{4}{5}} \quad (2.31)$$

In Eq. (2.31),  $\text{Nu}_w$  is the Nusselt number for fully developed single phase flow having a value of 3.67 for uniform wall temperature (UWT) and 4.36 for uniform wall flux (UWF),  $C$  is a model constant that was computed for best fit with data and has a value of 0.022. Note that the Reynolds number is based on the liquid plug length. This model can be used to determine the Nusselt number in similar situations involving well defined gas inclusions such as bubbles and slugs evolving in microfluidic devices, where  $L > 1$  mm and  $\text{Pr} > 1$  liquids. The model was shown to fit remarkably well with the simulated Nusselt data. Additionally, Narayanan and Lakehal (2008) examine the pressure drop and results are plotted graphically as pressure drop versus local channel position. The pressure drop was found to be higher in the case of up-flow as compared to zero-gravity and down-flow cases in that order. Bubbly flow was observed to have a lower pressure drop than single phase flow (except the up-flow case) and slug flow has a 14 - 15 % larger pressure drop than the single phase flow.

Muzychka and Awad (2008) present three different methods for two-phase flow modelling in mini-channels and micro-channels. The first method is a series of effective property models for homogenous flows that consist of models for viscosity, density, fanning friction factor, and Reynolds number. The second method was a new asymptotic model for the two-phase frictional multipliers. This is developed using the asymptotic analysis method introduced by Churchill and Usagi (1972). This asymptotic model is given by Eq. (2.32) and (2.33):

$$\phi_l^2 = \left[ 1 + \left( \frac{1}{X^2} \right)^p \right]^{\frac{1}{p}} \quad (2.32)$$

$$\phi_g^2 = \left[ 1 + (X^2)^p \right]^{\frac{1}{p}} \quad (2.33)$$

The parameter  $p$  that appears in Eq. (2.32) and (2.33) has a value chosen which minimizes the root mean square (RMS) error between the model predictions and published data. The third method presented by Muzychka and Awad (2008) for modelling two-phase flow in mini-channels and micro-channels is a rational bounds model for two-phase frictional pressure gradient. This model was developed by Awad and Muzychka (2007) and was detailed previously in this literature review. The effective property models for viscosity are compared to published data from Ungar and Cornwell (1992), Tran et al. (2000), Cavallini et al. (2005) and Field and Hrnjak (2007). The effective viscosity model that best predicted the experimental data was the Maxwell Eucken II model. This model has the lowest RMS error of 16.47% and is given by Eq. (2.34):

$$\mu_m = \mu_g \frac{2\mu_g + \mu_l - 2(\mu_g - \mu_l)(1-x)}{2\mu_g + \mu_l + (\mu_g - \mu_l)(1-x)} \quad (2.34)$$

The asymptotic models and mean bounds model developed by Muzychka and Awad (2008) given by Eq. (2.32), (2.33) and (2.30) are compared to published data graphically by plotting the two-phase flow multipliers versus the Martinelli parameter  $X$ . The fitting parameter  $p$  was chosen to be 0.5 for comparison with data. The published data used in

comparing Eq. (2.32) was Lee and Lee (2001) data, Chung and Kawaji (2004) data and Kawaji et al. (2005) data. The published data used in comparing Eq. (2.33) was Kawaji et al. (2005) data and Ohtake et al. (2005) data. The mean bounds model given by Eq. (2.30) was compared to all five data sets. The asymptotic model predicted liquid two-phase flow multiplier with RMS errors of 14.07%, 16.09% and 11.34%, while the mean bounds model predicted the data with a RMS error of 17.91%, 19.29%, and 10.49% respectively. The asymptotic model predicted gas two-phase flow multiplier with RMS error of 17.36% and 24.16%, while the mean bounds model had RMS errors of 14.87% and 28.04% respectively. The asymptotic models overall show best prediction of data when compared to the performance of the mean bounds model.

Muzychka et al. (2009) reviewed classic Graetz flow problems and heat transfer characteristics. Two models were developed using the asymptotic characteristics of plug and poiseulle flows for the constant wall boundary condition. These models were created using the Churchill-Usagi asymptotic correlation method for thermally developing Graetz flow. For slug flow the model for dimensionless heat transfer is given by Eq. (2.35) and the poiseulle flow model for dimensionless heat transfer is given by Eq. (2.36):

$$q^* = \left[ \left( \frac{1.128}{\sqrt{L^*}} \right)^2 + \left( \frac{1}{4L^*} \right)^2 \right]^{\frac{1}{2}} \quad (2.35)$$

$$q^* = \left[ \left( \frac{1.614}{L^{*\frac{1}{3}}} \right)^{\frac{3}{2}} + \left( \frac{1}{4L^*} \right)^{\frac{3}{2}} \right]^{\frac{2}{3}} \quad (2.36)$$

In Eq. (2.35) and (2.36),  $q^*$  is the dimensionless heat transfer and  $L^*$  is the dimensionless length. Muzychka et al. (2009) use the models in Eq. (2.35) and (2.36) and simple heat transfer theory to prove that the only way thermal enhancement can be achieved is if and only if a change in local velocity profile can be induced through segmentation. Thus clearly showing that the circulations present in liquid plugs during plug flow are the only mechanism that leads to heat transfer enhancement. The dimensionless heat transfer and

dimensionless length are then redefined to take into account the plug length and void fraction, these definitions are given by Eq. (2.37) and (2.38):

$$q^* = \frac{q/(\alpha_1 A) D_h}{k(T_w - T_i)} \quad (2.37)$$

$$L^* = \frac{(L_s/D)}{Pe_D} \quad (2.38)$$

Muzychka et al. (2009) then compare these new definitions of dimensionless heat transfer and dimensionless length given by Eq. (2.37) and (2.38) to published data. The comparison is made graphically by plotting dimensionless heat transfer versus dimensionless length. The data used were produced by Oliver and Young Hoon (1968), Horvath (1973), Vrentas (1978), Narayanan and Lakehal (2008), and Prothero and Burton (1961). These plots clearly indicate that better scaling of the dimensionless data is obtained when true wetted surface area and plug length are considered. Furthermore, Muzychka et al. (2009) proposes a model for predicting heat transfer for laminar gas-liquid segmented flow based on the wetted surface area given by Eq. (2.39):

$$q^* = \left[ \left( \frac{1.614}{L_s^{*\frac{1}{3}}} \right)^{-\frac{3}{2}} + \left( \frac{1}{4L_s^*} \right)^{-\frac{3}{2}} \right]^{-\frac{2}{3}} \quad (2.39)$$

Where  $L_s^*$  is the dimensionless plug length given by Eq. (2.40):

$$L_s^* = \frac{\pi \alpha_1 L_s k}{4 \dot{m}_1 c_p} \quad (2.40)$$

Walsh et al. (2009) conducted a investigation of segmented flow under uniform wall heat flux (UWF) condition. Experiments consisted of testing segmented flow in a heated section of stainless steel tube that was 2 m in length having a 1.5 mm internal diameter.

The temperature measurements were taken using four k-type thermocouples and a FLIR Systems (IR) camera. Walsh et al. (2009) presents a plot of time averaged mean wall temperature rise versus distance from the entrance of the tube for single phase flow and three segmented flows with slug length to diameter ratios of 1.6, 5.7 and 14.3. The general trends observed are that: shorter slugs provide augmented heat transfer over the entire test section; moderate length slugs can result in a degradation of heat transfer rates within early entrance region but augment in fully developed regions; and long length slugs can result in a degradation of heat transfer rates throughout the system. This is the first time that heat transfer rates for segmented flows with entrance region details were published.

Furthermore, Walsh et al. (2009) present a plot of local Nusselt number normalized by the liquid wetted region versus the inverse Graetz parameter  $x^*$ . This plot clearly shows that slug flow can degrade heat transfer within the entrance region but will typically augment heat transfer within the fully developed region. It was found that in transitioning from the entrance region to the fully developed region, the local Nusselt number oscillated about the fully developed limit with a period equal to the length of one internal liquid plug circulation. The maximum augmentation shown in this plot is a 700% enhancement over the fully developed continuous Graetz flow limit, this was for the shorter slugs with slug length to diameter ratio 1.6. Walsh et al. (2009) develops a model to predict local Nusselt number in segmented flows which consisted of deriving expressions for both the developing and fully developed regions. The entrance region asymptote was derived by taking the mean between the plug flow and poiseulle flow limits and is given by Eq. (2.41):

$$Nu_{x(s,Ent)} = Nu_{x(p,Ent)} + \frac{D}{L_s} [Nu_{(pl,Ent)} - Nu_{(p,Ent)}] \quad (2.41)$$

The fully developed flow limit is derived by adding the enhancement due to slug flow to the poiseulle flow limit and is given by Eq. (2.42):

$$\text{Nu}_{x(s,\text{Dev})} = \text{Nu}_{x(p,\text{Dev})} + 31.5 \left( \frac{D}{L_s} \right)^{\frac{1}{2}} \quad (2.42)$$

Walsh et al. (2009) then combine the two asymptotic limits in Eq. (2.41) and (2.42) using the Churchill-Usagi asymptotic correlation method. The final model created is given by Eq. (2.43):

$$\text{Nu}_{x(s)} = \left\{ \left( \text{Nu}_{x(s,\text{Ent})} \right)^{\frac{1}{n}} + \left( \text{Nu}_{x(s,\text{Dev})} \right)^{\frac{1}{n}} \right\}^n \quad (2.43)$$

The blending parameter  $n$  in Eq. (2.43) was given a value of 10 and the model showed excellent agreement with experimental data when presented graphically. Overall, Walsh et al.'s (2009) findings provide greater understanding of the physics of segmented flow.

## **Chapter – 3**

### **Experimental Methods**

#### **3.1 Introduction**

This chapter details the design of two miniature heat sinks as well as the experimental setup used for measuring the heat transfer characteristics of a two-phase segmented flow in these sinks. First, experimental objectives will be discussed, followed by a detailed description of the conceptual design and fabrication of the two heat sinks. The experimental apparatus, assembly, operation, and procedures will then be presented. Experiments carried out to calibrate the equipment will also be included. Finally, a discussion on experimental uncertainty will be addressed.

#### **3.2 Experimental Objectives**

The main objectives of the experiment are to measure and determine the heat transfer characteristics of two-phase flow in a miniature heat transfer system. The focus will be on the comparison of single phase flow to two-phase flow, in particular segmented two phase flow. Attention will also be given to how results vary according to changes in flow path geometry. Hence, it was decided that two distinct test units would be conceived. For the purpose of this experiment the most suitable design would be two miniature heat sinks. These designs would have varying flow path geometries, while maintaining the same cross-sectional area and total path length, which is beneficial when conducting a comparison of both heat sinks.

### 3.3 Miniature heat sinks

Two miniature heat sinks were designed using SolidWorks 2007 computer aided design software. The designs were submitted to Memorial Technical Services (Mechanical Division) for fabrication. Each heat sink was comprised of two parts of stainless steel (thermal conductivity  $k = 16 \text{ W/m}\cdot\text{k}$ ) with dimensions of 30 mm x 30 mm x 3.5 mm. Each stainless steel part was polished to a mirror finish on one face. The technical drawing for the heat sinks are in Appendix A.

The first part is a base plate in which a custom designed fluid path was machine cut into the polished surface. The second part functions as a cover plate. The cover plate has small grooves machine cut in the non-polished face to house thermocouples. These thermocouples are installed in five specific positions in order to measure the center and average temperature of the heat sink. In the first heat sink a square wave pattern was machined. This heat sink will be termed the Square Sink. In the second heat sink a spiral pattern was machined. This heat sink will be termed the Spiral Sink. The flow path designs are illustrated in Figure 3.1.

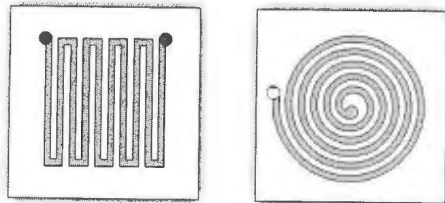


*Figure 3.1 – Flow path designs: Square and Spiral.*

The aforementioned patterns were designed with the equivalent cross sectional area and total path length. The channel cross sectional area is a 1 mm x 1 mm square and the total path length is 213 mm. The fabricated base plates are illustrated in Figure 3.2.

The base plate and the cover plate are oriented such that the polished faces mate together. Two strip heaters are then attached to the external faces of the base and cover plates. These strip heaters provide symmetrical and constant heat flux to the sink. A hand-

tightened C-clamp is used to provide adequate compressive force to the heat sink, eliminating system leakage and maintaining the proper fluid flow within the channel.

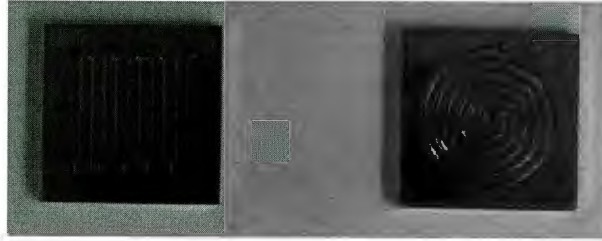


*Figure 3.2 – Fabricated base plates: Square and Spiral.*

The fluid inlet and outlet ports were positioned differently for both heat sinks. In the Square Sink, the inlet and outlet ports were located solely on the base plate. However, in the Spiral Sink the inlet port was located on the cover plate whereas the outlet port was located on the base plate. This was due to clearance issues regarding the thickness of the base plate. All ports were 2 mm in diameter and threaded using a 2/64 inch imperial tap. The ports were threaded so that a 1/16 inch two-way hose barb could be inserted and securely fastened. The Square Sink and Spiral Sink cover plates are illustrated in Figure 3.3.

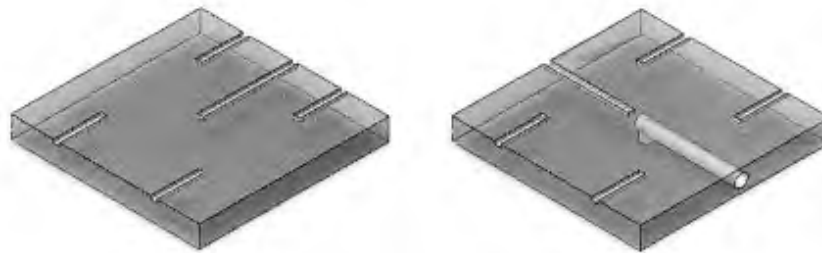


*Figure 3.3 – Cover plate designs: Square and Spiral.*

It is clearly observed that the Spiral Sink cover plate (on the right of Figure 3.3) differs from the Square Sink cover plate (on the left in Figure 3.3) in that it contains an additional conduit which supplies fluid to the center of the spiral channel on the base plate. The five thermocouple grooves are visible in each cover plate. Four of the thermocouples are located at the center of each quadrant, used to measure average surface

temperature. The fifth thermocouple is located at the center of each cover plate, used to measure center temperature. The technical drawings for both sinks are provided in Appendix A.

## **3.4 Experimental Apparatus, Assembly and Operation**

### **3.4.1 Introduction**

This section will examine the apparatus, assembly and operation of the experimental setup utilized to measure the heat transfer characteristics and the pressure drop across the heat sinks. First, details will be given about each individual component of the system, including its particular role and technical aspects. Next, the complete construction of custom-made apparatus as well as experimental assembly will be reviewed. Last, the operation of the experimental setup will be discussed.

### **3.4.2 Experimental Apparatus**

#### **3.4.2.1 Pumps**

Two identical pumps are used for the single and two-phase flow experiments. These are HARVARD Syringe Pump Model 33. These pumps are dual (or twin) syringe pump models meaning they can be equipped with two syringes. The HARVARD Syringe Pump Model 33 is illustrated in Figure 3.4. The pump operates off 115 VAC supply and can deliver up to 53.346 ml/min with a 50 ml syringe, is capable of pressures up to 99.5 psi with a 20 ml syringe with an accuracy of  $\pm 1.0\%$ . The pump operates in one of two modes, proportional or continuous. In proportional mode the syringes may have different diameters and rates while in continuous mode both syringes use the same diameter and rate.



Figure 3.4 – HARVARD Syringe Pump Model 33.

For the single phase and two-phase flow experiments, the pump will be equipped with two 60 ml syringes, will be used in continuous mode with diameter set to 26.82 mm (this is the internal diameter of the 60 mm syringes measured with a telescopic gauge).

### 3.4.2.2 Thermocouples

A total of seven copper constantan 30 gage thermocouples are used to measure the inlet, outlet, and five surface temperatures during the single and two-phase flow experiments. The seven thermocouples are connected to the DAQ on channels 2 to 8 and the locations of each thermocouple with regards to DAQ channel and cover plate position are detailed in Figure 3.5. The inlet and outlet are CH7 and CH8. The thermocouples have an accuracy of  $\pm 0.1$  °C. The inlet and outlet thermocouples had to be custom-made using a T-junction. The details of this are found in Section 3.3.3. The thermocouples are calibrated and checked using a constant temperature bath of ice and water, the details of this are found in Section 3.5.

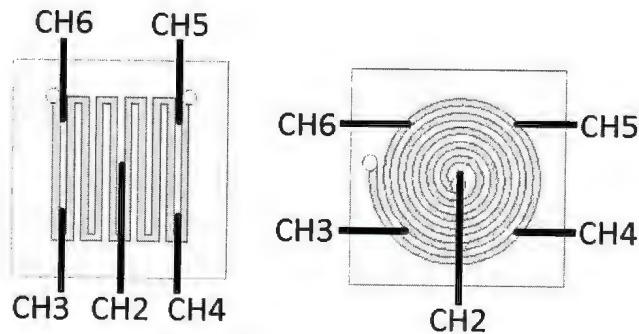
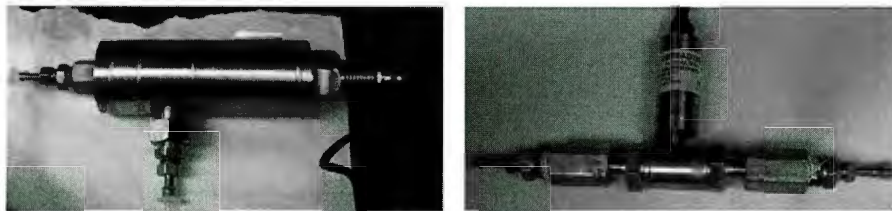


Figure 3.5 – Thermocouple location and channel assignment.

### 3.4.2.3 Pressure Transducers

Two pressure transducers were used to measure the differential pressure drop across the inlet and outlet of the heat sinks. The first was an OMEGADYNE PX81D0-050DI model pressure transducer which was used for experiments with the Square Sink. This pressure transducer is rated for 0-50 psid with an electrical supply of 25-30 VDC and has a current output of 4 to 20 mAmps. It was calibrated by OMEGADYNE INC. using standards set by the United States National Institute of Standards Technology (NIST). While the pressure transducer's high end pressure readings follow a linear trend, the low end pressure readings do not follow a linear trend. Therefore, a calibration curve was developed to account for this deviation. The details of this calibration are found in Section 3.5.



*Figure 3.6 – PX81D0-050DI (left) and PX409-005DWU5V (right).*

The reason for the switch in pressure transducers was due to the non-linear nature of the PX81D0-050DI model, therefore it was decided to order a new transducer but utilize the previous model until the new one arrived. The second pressure transducer used in experiments was a OMEGADYNE PX409-005DWU5V model. This pressure transducer was used in experiments with the Spiral Sink. This pressure transducer is rated for 0-5 psid with an electrical supply of 24 VDC and has a voltage output of 0 to 5 VDC. It was calibrated by OMEGADYNE INC. using standards set by the United States National Institute of Standards Technology (NIST). The calibration worksheet was included with the packaged unit, and is given in Section 3.5. Both of the OMEGADYNE transducers used for experiments have an accuracy of  $\pm 1\%$ . The transducers are shown in Figure 3.6.

#### 3.4.2.4 Heaters

Each heat sink was equipped with two WATLOW heating strips to provide a symmetric and constant heat flux. The dimensions of each heating strip are 25 mm x 25 mm. They are positioned with the same orientation on opposing sides of the heat sink using pressure sensitive adhesive (PSA). The heating strips required an excitation of 28 VDC to provide a constant 5 W of heat. Reducing the input voltage to the heater simply reduces the power output. The power is related to the resistance and voltage drop across the heater given by Eq. (3.1):

$$P = \frac{V^2}{R} \quad (3.1)$$

where P is power, V is voltage and R is resistance. Two heating strip power wires were connected in parallel yielding an equivalent resistant of 83.50  $\Omega$  for the Square Sink and 79.40  $\Omega$  for the Spiral Sink. The wiring diagram for the heaters is shown in Figure 3.7.

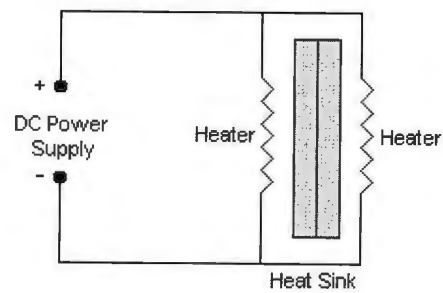


Figure 3.7 – Wiring diagram for WATLOW heating strips.

#### 3.4.2.5 Power Supply

Two EXTECH 382200 series power supplies were used to provide excitation to the heating strips and the pressure transducer. These power supplies are variable DC output with a range of 0 - 30 VDC and current output of 0 – 1 amp. The accuracy of the power supplies was  $\pm 1.0\%$ . The two power supplies are shown in Figure 3.8.



*Figure 3.8 – EXTECH 382200 power supplies.*

### **3.4.2.6 Hydraulic Components**

The hydraulic components consist of various parts shown in Figure 3.9. These components include several T-junctions, valves, connectors, and tubing. All the luer-lock connectors were sized for the 1/16 inch ID Nalgene tubing. For the generation of two-phase segmented flow a PEEK 0.020 inch T-junction was used to create long liquid slugs while a 0.0625 inch stainless steel T-junction was used to create short liquid slugs. All components were obtained from Cole-Parmer LABCOR Inc.

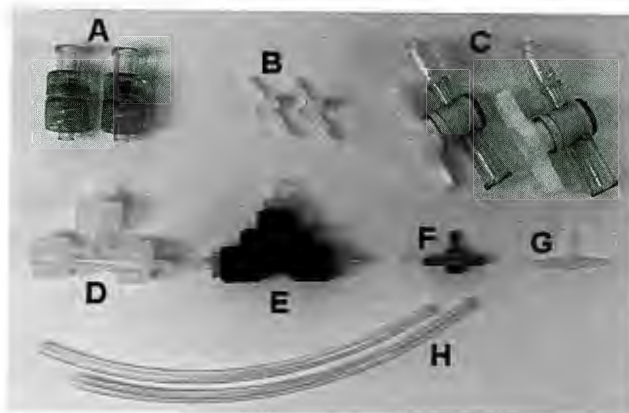


*Figure 3.9 – Hydraulic components: (a) check valves, (b) two-way connector, (c) shut-off valve, (d) 0.165 inch T-junction, (e) PEEK 0.020 inch T-junction, (f) 0.0625 inch stainless steel T-junction, (g) 0.03125 inch T-junction, (h) 1/16 inch ID Nalgene tubing.*

### 3.4.2.7 Data Acquisition System

The data acquisition is carried out using a KEITHLEY 2700 Data Acquisition System. It is capable of simultaneously reading and recording 25 channels. The KEITHLEY 2700 interfaces with a computer via RS232 serial cable, and XLINX Start-Up Software version 2.1.0 was used to communicate with the unit. For the purpose of measuring temperatures and pressure during the single and two-phase flow experiments, seven thermocouple wires with quick connect blocks as well as one wire for the pressure transducer signal were connected to the KEITHLEY 2700. The XLINX software was setup to read the thermocouples as T-type (in °C) and read the pressure transducer channel as current input (in mA). The KEITHLEY 2700 DAQ is shown in Figure 3.10.

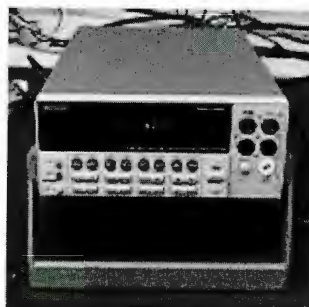


*Figure 3.10 – KEITHLEY 2700 Data Acquisition System.*

### 3.4.2.8 Camera

The camera used for taking photographs of the two-phase segmented flow during each experimental run was a SONY Handycam model HDR-FX7. The camera is capable of high definition picture and video. During video recording the data is stored on a HDV cassette however still photographs are stored on a memory card. The photographs were transferred from a memory card to a computer for slug length analysis after each experiment. Each photograph had a ruler in the field of view for measurement reference. The accuracy used in uncertainty analysis for measurements taken from the high definition photographs was  $\pm 0.2$  mm.

### 3.4.2.9 Fluids

The working fluids used in all experiments were water, canola oil, and air. The properties for water were calculated using the following expressions,

$$\rho_{\text{water}} = -342.584 + 164.103 T^{0.5} - 5.01225 T$$

$$c_{p_{\text{water}}} = 3805070 - 1028080 T^{0.5} + 111160 T - 6005.26 T^{\frac{3}{2}} + 162.081 T^2 - 1.7482 T^{\frac{5}{2}}$$

$$k_{\text{water}} = -2.76131 + 0.340118 T^{0.5} - 0.00838245 T$$

$$\mu_{\text{water}} = (31.6371 - 6.37804 T^{0.5} + 0.485827 T - 0.016519 T^{\frac{3}{2}} + 0.000211278 T^2)^3$$

The benchmarking of single phase water using the above expressions for the properties in the reduction of data led to excellent agreement between experimental measurements and theory (shown in Chapter 4). The properties for canola oil were taken from Przybylski (2000). The density was measured at room temperature to be  $902.3 \text{ kg/m}^3$  and found to agree very well with the reported value at  $25 \text{ C}$  of  $910 \text{ kg/m}^3$ . Similarly, a simple capillary tube test was undertaken to test the viscosity at room temperature at several flow rates, and near room temperature values typical of the experiment. At  $25 \text{ C}$ , the viscosity was found to be  $0.053 \text{ Pa}\cdot\text{s}$ . Again, this single point was in excellent agreement with the reported data of  $0.059 \text{ Pa}\cdot\text{s}$ . The mean reported value of specific heat,  $1913 \text{ J/kgK}$  was also used for reduction of data. However, the thermal conductivity based on experiments was found to be much lower than the reported value given by Przybylski (2000). Since the benchmarking with water was found to provide very good results when compared to theory, the thermal conductivity of the oil was found by minimizing the error between the present single phase measurements and the Graetz theory. This yielded a value of  $0.089 \text{ W/mK}$ , which was about one half the value reported by Przybylski (2000).

### 3.4.3 Experimental Assembly

When fabrication of the two heat sinks was complete, assembly immediately began. The Square Sink cover plate was secured to a table and then five thermocouple wires were placed into the grooves as shown in Figure 3.11. Each thermocouple was then surrounded by Omegabond 101 epoxy adhesive, which was spread uniformly over the groove void around the inserted thermocouple. The cover plate was then left so that the adhesive compound would fully cure, which took approximately 24 hours. When the adhesive was hardened, the cover plate was unsecured from the table and could be handled normally without the thermocouples dislodging from their respective grooves.

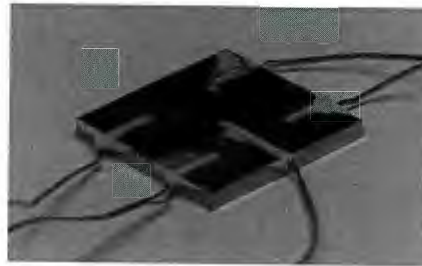


*Figure 3.11 – Cover plate with secured thermocouples.*

Two Watlow peel-and-stick heating strips were then applied to the cover plate and base plate. Care was given to the placement of these heaters to ensure they were positioned in the center of each plate, so that the heat flux provided would be approximately symmetric from the bottom of the sink to the top. The base plate can be seen in Figure 3.12 with the Watlow heating strip applied to its bottom surface.

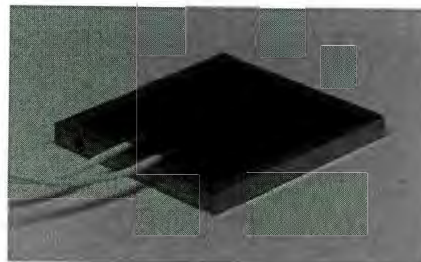


*Figure 3.12 – Watlow heating strip applied to the Square Sink base plate.*

After the heaters were applied, the Square Sink cover plate and base plate were then aligned, polished surface to polished surface. The Square Sink was then placed within the confinement of a C-clamp and two pieces of Plexiglass were placed on either side of the heat sink between the sink and clamp. The C-clamp was then hand-tightened to provide adequate compression to ensure the Square Sink was sealed. A polyurethane coating was then applied to the exposed seams on the edges of the Square Sink to ensure that any micro voids would be eliminated. With the Square Sink clamped, two 1/16 inch two-way hose barb connectors were screwed into the threaded inlet and outlet ports on the sink. Where the barbed connectors were fastened to the Square Sink more polyurethane was applied to ensure the inlet and outlet ports would not leak. The full assembly of the Square Sink can be seen in Figure 3.13.

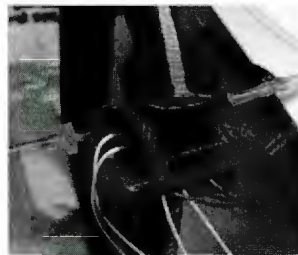


*Figure 3.13 – Square Sink assembly.*

To measure the inlet and outlet temperatures of the single phase or two-phase fluid, two custom-made temperature probes had to be created. A plastic T-junction with 1/16 inch hose barbs was used in the construction of these temperature probes. T-type thermocouple wire was inserted into the center inlet on the T-junction. The thermocouple was positioned until the wire tip was penetrating halfway into the fluid stream, if the stream were moving between the inlets that are axially in line with one another. Once the thermocouple was in position, polyurethane glue was used to secure the wire in place. It was left to cure for a period of 6 hours. Thereafter, heat shrink was placed over the glued section and heated so that it tightened around the wire and central inlet of the T-junction. This would ensure that the custom made probe would not leak. The custom-made temperature probe is illustrated in Figure 3.14.

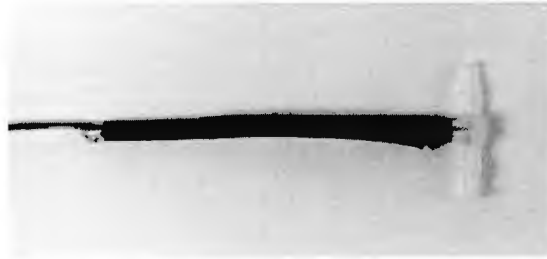


*Figure 3.14 – Custom-made temperature probe.*

When construction of two temperature probes was complete a 10 mm length of tubing was used to connect each temperature probe to the inlet and outlet of the heat sink. All the tubing used had a 1/16 inch inner diameter (1.58 mm). Another 10 mm length of tubing was used to connect each temperature probe to a pressure transducer T-junction. The fluid would flow axially along the T-junction and the pressure transducer would be connected using the same tubing to the perpendicular inlet on the T-junction. The pressure transducer was connected with the high pressure side on the heat sink inlet and the low pressure side on the heat sink outlet. A 20 cm length of tubing was attached to the open end of the pressure T-junction on the outlet of the heat sink. This length of tubing simply ran into a discharge tank. On the inlet side of the heat sink, a 30 cm length of tubing was attached to the pressure T-junction. This 30 cm length of tubing was laid across a white background. This region serves as a flow visualization and measurement section. A ruler was placed parallel and in close proximity to the tubing, as to allow any photographs taken to have a measurement reference. When comparing experimental results to theoretical results, the slug lengths of the liquid phase and gas phase must be determined from these photographs.

The 30 cm length of tubing used for the visualization area then connected to one of two T-junctions. The first T-junction had an orifice size of 0.020 inches and was used for creating longer slugs during two-phase flow. The second T-junction had an orifice size of 0.0625 inches and was used for creating shorter slugs during two-phase flow. Two syringe pumps were then connected via tubing to the remaining two axial and perpendicular inlets on this T-junction. Two one-way check valves were put into place just before the T-junction to ensure no backflow was possible, thus eliminating the

possibly of cross contamination of fluid supplies. The syringe pumps were each equipped with two 60 ml syringes (for 120 ml capacity per pump). One pump was charged with 120 ml of water, while the second pump was charged with 120 ml of either air or oil.

Two Extech DC power supplies were connected to the Watlow heater and pressure transducer power wires. A Tenma digital multi-meter was connected in parallel over the heater power wires to monitor the voltage across the unit. The seven thermocouple signal wires (inlet, outlet, and five surface thermocouples) and the pressure transducer signal wire were connected to the Keithley 2700 data acquisition unit. The data acquisition unit was then connected to a computer and XLINX Start-up Software version 2.1.0 was installed. The software was setup to monitor the seven thermocouple and pressure transducer signals and record the readings 10 times over an interval of 10 seconds. Upon completion of all previous instructions, the experimental assembly was complete and ready for testing. The schematic of the experimental assembly is illustrated in Figure 3.15. When assembling the Spiral Sink the same procedure indicated for the Square Sink was followed.

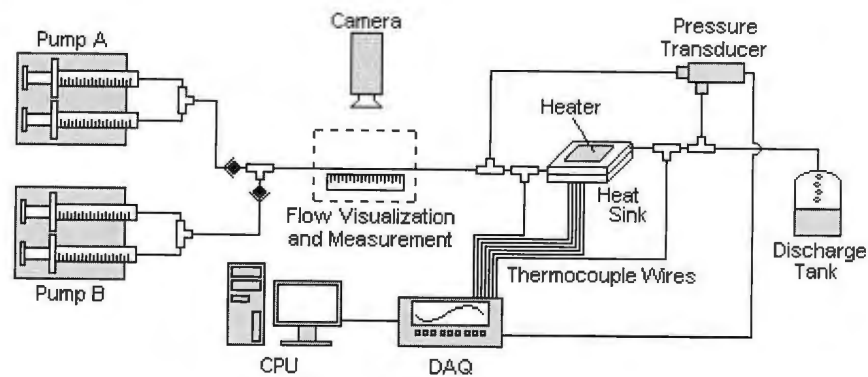


*Figure 3.15 – Experimental Schematic.*

### **3.4.4 Experimental Operation**

The schematic of the experimental assembly is shown in Figure 3.15. Two dual syringe pumps are utilized to produce single phase and two-phase flow. It was decided to use two pumps – as opposed to one – in order to increase fluid capacity. An increased fluid

capacity allows for longer experimental studies at higher flow rates. The syringe pumps were each charged with two 60 ml syringes. During single phase flow experiments both syringe pumps contain the same fluid. However, during two-phase flow experiments each syringe pump contains a different fluid (ie water, oil, or air). When the experiment is initiated the syringe pumps transfer the fluid into a 1/16 inch tube. The fluid travels along the tube, passing through check valves installed along the line. Upon clearing the check valves, the two fluids proceed to meet at a T-junction. For two-phase flow experiments this T-junction has a small orifice to ensure proper segmented flow maturity. The fluid continues through a flow visualization and measurement section. A camera records images of the flow within this section, which are processed after each experimental run. Pressure transducer and thermocouple junctions precede the fluid's entrance into the heat sink. Upon entry, the fluid is forced to conform to the distinct flow path of that particular sink. Upon exit, the fluid encounters another set of pressure transducer and thermocouple junctions. After passing completely through the system, the fluid is discharged into a container.

During operation the system is allowed to come to a steady state condition with regards to center surface temperature of the sink being constant. When this steady state condition is achieved, the CPU connected to the DAQ is used to record 10 discrete data readings over a 10 second interval. With the pressure and temperature readings recorded for the experimental run, the dimensionless heat transfer characteristics and pressure drop can hence be calculated and compared to theory.

### **3.5 Experimental Procedure**

The experimental procedure began with the testing of the Square Sink. First, single phase water was tested by running 17 different flow rates ranging from 2.50 ml/min to 120 ml/min. For each flow rate the system was provided with 10.0 Watts of power and the center temperature (channel 2 on the DAQ) was allowed to reach a steady state condition. Typically this took 2 to 3 minutes per run. Once steady state was achieved the DAQ collected 10 data readings from each sensor over a period of 10 seconds.

Second, single phase canola oil was tested. The same procedure previously described was applied for single phase oil but because of the high viscosity and Prandtl number of the fluid, the power input and flow rates were reduced. The oil was instead tested at 12 different flow rates ranging from 1.0 ml/min to 20.0 ml/min with a power input of 2.5 Watts. Thirdly, the two-phase segmented flow of oil-air was tested over 15 runs using the 0.020 inch T-junction. The oil flow rate ranged from 2.0 ml/min to 4.0 ml/min while the air flow rate ranged from 0.0 ml/min to 4.0 ml/min. The power was set for 2.5 Watts for the oil-air runs. Finally, water-air two-phase segmented flow was tested over 11 runs using the 0.020 inch T-junction. The water flow rate ranged from 2 ml/min to 4 ml/min and the air flow rate ranged from 0.0 ml/min to 4.0 ml/min. The power input was 2.5 Watts for the water-air runs.

Additionally, a T-junction with an orifice size of 0.0625 inches that allowed for the creation of shorter slugs was obtained. The Square Sink was again tested with two-phase segmented flow of water-air over 23 runs. The water flow rate ranged from 3.0 ml/min to 10.0 ml/min and the air flow rate ranged from 0.0 ml/min to 10.0 ml/min. The power input for these series of tests was 2.5 Watts. It should be noted that for all the Square Sink experiments the PX81D0-050DI model pressure transducer was used.

After the Square Sink was tested, the Spiral Sink was installed in the system. The PX409-005DWU5V pressure transducer was available at this time and it was much better suited for the application so it was also installed and the PX81D0-050DI model was taken out. The 0.0625 inch T-junction was used for all experimental runs with the Spiral Sink since it lead to the creation of shorter slug lengths. Single phase flow of water was tested first over 17 runs with the flow entering the middle of the spiral and exiting on the side of the sink. The water flow rate ranged from 2.50 ml/min to 120.0 ml/min. Secondly, single phase water was repeated but this time the flow entered the side of the sink and exited in the middle. The same flow rates were used and the power input for both single phase tests was 7.5 Watts. Finally, two-phase segmented flow of water-air was tested over 23 runs,

again for both directions. The water flow rate ranged from 3.0 ml/min to 10.0 ml/min and the air flow rate ranged from 0.0 ml/min to 10.0 ml/min. The power input to the Spiral Sink for the two-phase segmented flow runs was 2.5 Watts.

### 3.6 Sensor Calibration

#### 3.6.1 Thermocouple Calibration

The seven thermocouples for each heat sink were calibrated using a constant temperature bath of ice and water. The results of this calibration are shown in Table 3.1 for both heat sink thermocouples. While in the ice bath, the data acquisition unit was programmed to adjust the seven thermocouples for each heat sink to 0 °C in order to calibrate them.

**Table 3.1**  
**Ice bath thermocouple calibration results.**

DAQ Channel #	Square Sink	Spiral Sink
2 (center)	0.00 °C	0.05 °C
3 (quadrant)	0.05 °C	0.00 °C
4 (quadrant)	0.00 °C	0.10 °C
5 (quadrant)	0.10 °C	0.00 °C
6 (quadrant)	0.00 °C	0.00 °C
7 (inlet)	0.00 °C	0.00 °C
8 (outlet)	0.00 °C	0.00 °C

#### 3.6.2 Pressure Transducer Calibration

The PX81D0-050DI model pressure transducer operated with a non-linear trend in the range of pressures experienced during testing. Therefore it was necessary to create a calibration curve for this range of pressure. A 1.0 m length of tubing with 1/16 inch internal diameter was placed between both high and low junctions of the pressure

transducer. The pressure drop over this length of tubing for laminar flow can be calculated using Eq. (3.2):

$$\Delta P = 4f \frac{L}{D} \frac{1}{2} \rho u^2 \quad (3.2)$$

where the fanning friction factor  $f$  is given by Eq. (3.3):

$$f = \frac{16}{\text{Re}_{D_h}} \quad (3.3)$$

Single phase water was pumped through the tube at different flow rates ranging from 0 ml/min to 120 ml/min. The current output from the PX81D0-050DI pressure transducer was recorded then the pressure calculated using the equation above was used to create a calibration curve. This calibration curve is given by the following expression,

$$\Delta P = -4 \times 10^6 I^2 + 53506 I - 146.11$$

where  $I$  is the current output from the pressure transducer in milliamps and  $\Delta P$  is the differential pressure drop corresponding to that current output in kPa. The manufacturer did not list the accuracy of the PX81D0-050DI pressure transducer in this non-linear range, so it was taken to be the same as in the linear range, being  $\pm 1\%$ .

The PX409-005DWU5V pressure transducer came with a pre-existing calibration chart that was verified to be correct. The calibration chart is given in Table 3.2.

**Table 3.2**

**PX409-005DWU5V pressure transducer calibration worksheet.**

Pressure PSID	OUTPUT VDC
0.0	-0.004
2.5	2.500
5.0	5.002
2.5	2.500
0.0	-0.003

### **3.6.3 Thermal Resistance Check**

Two experiments were conducted using each heat sink to test the thermal resistance from the sink to the surroundings. These experiments consisted of setting the power input to a given sink at a fixed value, then measuring the steady state heat sink temperature corresponding to that power input. The power inputs tested were 0.5 Watts and 1.0 Watts. When the steady state sink temperature was obtained the room temperature was recorded and the thermal resistance to surroundings could be calculated using Eq. (3.4):

$$R_{sur} = \frac{T_{ave} - T_{sur}}{Q_{in}} \quad (3.4)$$

where  $T_{sur}$  is the room temperature,  $Q_{in}$  is the power input and  $T_{ave}$  is the average sink temperature. For the Square Sink when the power input was 0.5 Watts the thermal resistance was calculated to be 22.7 K/W and when the power input was 1.0 Watts the thermal resistance was calculated to be 23.3 K/W. For the purposes of calculating bulk heat transfer to working fluid through a system energy balance the thermal resistance will be taken as approximately 23.0 K/W for the Square Sink. For the Spiral Sink when the power input was 0.5 Watts the thermal resistance was calculated to be 19.9 K/W and when the power input was 1.0 Watts the thermal resistance was calculated to be 20.1 K/W. For the purposes of calculating bulk heat transfer to working fluid through a system energy balance the thermal resistance will be taken as approximately 20.0 K/W for the Spiral Sink.

### 3.7 Experimental Uncertainty

The experimental uncertainty in the dimensionless heat transfer  $q^*$ , Nusselt number, Reynolds number, Prandtl number, Peclet number, differential pressure and dimensionless length  $L^*$  depends on the uncertainty in the experimental measurement of temperature, flow rate, pressure and system tolerance. The uncertainty in experimental measurements are given in Table 3.3.

**Table 3.3**  
**Uncertainty in Experimental Measurements.**

Measurement	Uncertainty
Temperature - [°C]	$\pm 0.1$ °C
Differential Pressure - [Pa]	$\pm 1\%$
Flow Rate - [ml/min]	$\pm 1\%$
Dimension Tolerance [mm]	$\pm 0.02$ mm
Fluid Properties	$\pm 0.5\%$
Measurement of Images [mm]	$\pm 0.2$ mm

The experimental uncertainties for this experiment were determined using the root sum square method outline by Kline and McClintock (1953). The uncertainty analysis is carried out at two different  $\Delta T$  values. This temperature difference is across the outlet and inlet of the system. Since both heat sinks used have the same overall channel length and all other features are similar, only one need be used for calculation of uncertainty. The two-phase segmented flow of water will be used in uncertainty analysis and the two values of temperature difference used will be  $\Delta T = 3.12$  °C and  $\Delta T = 8.11$  °C. The root sum square method assumes a calculated result  $R$  is a given function of independent measured variables  $x_1, x_2, x_3, \dots, x_n$ , which is shown in Eq. (3.5):

$$R = R(x_1, x_2, x_3, \dots, x_n) \quad (3.5)$$

From Eq. (3.5), the total uncertainty in the result  $R$  is given by  $w_R$  and the uncertainties in the independent measured variables are given by  $w_1, w_2, w_3, \dots, w_n$  and the relationship between these is given by Eq. (3.6):

$$w_R = \left[ \left( \frac{\partial R}{\partial x_1} w_1 \right)^2 + \left( \frac{\partial R}{\partial x_2} w_2 \right)^2 + \left( \frac{\partial R}{\partial x_3} w_3 \right)^2 + \dots + \left( \frac{\partial R}{\partial x_n} w_n \right)^2 \right]^{\frac{1}{2}} \quad (3.6)$$

Applying this method to each of the parameters above, expressions for the uncertainty due to experimental measurements can be calculated. The overall uncertainty in Reynolds number is determined from Eq. (3.7):

$$\frac{\delta Re_{D_H}}{Re_{D_H}} = \left[ \left( \frac{\delta \rho}{\rho} \right)^2 + \left( \frac{\delta \mu}{\mu} \right)^2 + \left( \frac{\delta D_H}{D_H} \right)^2 + \left( \frac{\delta Q}{Q} \right)^2 + \left( \frac{\delta \alpha}{\alpha} \right)^2 + 2 \left( \frac{\delta D}{D} \right)^2 \right]^{\frac{1}{2}} \quad (3.7)$$

The overall uncertainty in Prandtl number is determined from Eq. (3.8):

$$\frac{\delta Pr}{Pr} = \left[ \left( \frac{\delta c_p}{c_p} \right)^2 + \left( \frac{\delta \mu}{\mu} \right)^2 + \left( \frac{\delta k}{k} \right)^2 \right]^{\frac{1}{2}} \quad (3.8)$$

The overall uncertainty in temperature difference is determined from Eq. (3.9):

$$\frac{\delta \Delta T}{\Delta T} = \left[ \left( \frac{\delta T_i}{T_i} \right)^2 + \left( \frac{\delta T_o}{T_o} \right)^2 \right]^{\frac{1}{2}} \quad (3.9)$$

The overall uncertainty in the average surface temperature is determined from Eq. (3.10):

$$\frac{\delta \bar{T}_s}{\bar{T}_s} = \left[ \left( \frac{\delta T_{CH3}}{T_{CH3}} \right)^2 + \left( \frac{\delta T_{CH4}}{T_{CH4}} \right)^2 + \left( \frac{\delta T_{CH5}}{T_{CH5}} \right)^2 + \left( \frac{\delta T_{CH6}}{T_{CH6}} \right)^2 \right]^{\frac{1}{2}} \quad (3.10)$$

The overall uncertainty in the void fraction (and liquid fraction) is determined from Eq. (3.11)

$$\frac{\delta \alpha}{\alpha} = \left[ \left( \frac{\delta L_{l,s}}{L_{l,s}} \right)^2 + \left( \frac{\delta L_{g,s}}{L_{g,s}} \right)^2 \right]^{\frac{1}{2}} \quad (3.11)$$

The overall uncertainty in the bulk heat transfer to the liquid is determined from Eq. (3.12):

$$\frac{\delta Q_{bulk}}{Q_{bulk}} = \left[ \left( \frac{\delta Q}{Q} \right)^2 + \left( \frac{\delta \Delta T}{\Delta T} \right)^2 + \left( \frac{\delta c_p}{c_p} \right)^2 + \left( \frac{\delta \rho}{\rho} \right)^2 \right]^{\frac{1}{2}} \quad (3.12)$$

The overall uncertainty in the dimensionless heat transfer is determined from Eq. (3.13):

$$\frac{\delta q^*}{q^*} = \left[ \left( \frac{\delta k}{k} \right)^2 + \left( \frac{\delta \bar{T}_s}{\bar{T}_s} \right)^2 + \left( \frac{\delta T_i}{T_i} \right)^2 + \left( \frac{\delta D_H}{D_H} \right)^2 + \left( \frac{\delta Q_{bulk}}{Q_{bulk}} \right)^2 + \left( \frac{\delta \alpha}{\alpha} \right)^2 + 4 \left( \frac{\delta D}{D} \right)^2 + \left( \frac{\delta L}{L} \right)^2 \right]^{\frac{1}{2}} \quad (3.13)$$

The overall uncertainty in the  $\Delta T_{LMTD}$  is determined from Eq. (3.14):

$$\frac{\delta \Delta T_{LMTD}}{\Delta T_{LMTD}} = \left[ \left( \frac{\delta T_i}{T_i} \right)^2 + \left( \frac{\delta T_o}{T_o} \right)^2 + \left( \frac{\delta \bar{T}_s}{\bar{T}_s} \right)^2 \right]^{\frac{1}{2}} \quad (3.14)$$

The overall uncertainty in the Nusselt number is determined from Eq. (3.15):

$$\frac{\delta Nu}{Nu} = \left[ \left( \frac{\delta k}{k} \right)^2 + \left( \frac{\delta \Delta T_{LMTD}}{\Delta T_{LMTD}} \right)^2 + \left( \frac{\delta D_H}{D_H} \right)^2 + \left( \frac{\delta Q_{bulk}}{Q_{bulk}} \right)^2 + \left( \frac{\delta \alpha}{\alpha} \right)^2 + 4 \left( \frac{\delta D}{D} \right)^2 + \left( \frac{\delta L}{L} \right)^2 \right]^{\frac{1}{2}} \quad (3.15)$$

The overall uncertainty in the Peclet number is determined from Eq. (3.16):

$$\frac{\delta Pe}{Pe} = \left[ \left( \frac{\delta Re}{Re} \right)^2 + \left( \frac{\delta Pr}{Pr} \right)^2 \right]^{\frac{1}{2}} \quad (3.16)$$

The overall uncertainty in the dimensionless length is determined from Eq. (3.17):

$$\frac{\delta L^*}{L^*} = \left[ \left( \frac{\delta Pe}{Pe} \right)^2 + \left( \frac{\delta L}{L} \right)^2 + \left( \frac{\delta D}{D} \right)^2 \right]^{\frac{1}{2}} \quad (3.17)$$

Applying each of the above equations to the two data sets for  $\Delta T = 3.12 \text{ }^\circ\text{C}$  and  $\Delta T = 8.11 \text{ }^\circ\text{C}$ , the uncertainties for important parameters are given in Table 3.4. All parameters change between the two data sets with the exception of Prandtl number and differential pressure drop whose uncertainties do not vary between the data sets. It is shown in Table 3.4 that the uncertainties for all important parameters are lower when  $\Delta T = 8.11 \text{ }^\circ\text{C}$  than when  $\Delta T = 3.12 \text{ }^\circ\text{C}$ .

**Table 3.4**  
**Calculated Uncertainty in Parameters.**

Parameter	Uncertainty at $\Delta T=3.12$ °C	Uncertainty at $\Delta T=8.11$ °C
Re	7.28%	5.64%
Pr	0.87%	0.87%
$q^*$	7.91%	6.36%
$L^*$	7.60%	6.04%
Nu	7.92%	6.43%
$\Delta P$	1.00%	1.00%

### 3.8 Summary

This chapter presented details of the design and fabrication of two minichannel heat sinks, the experimental apparatus, assembly, operation and procedure and the calibration of the thermocouples and pressure transducers. A discussion on experimental uncertainty has also been addressed relating to the parameters used in data reduction in the next chapter.

# Chapter – 4

## Experimental Results

### 4.1 Introduction

This chapter will discuss the thermal performance results from the conducted experiments on single and two-phase flow. The data reduction procedures to determine the dimensionless heat transfer  $q^*$  and dimensionless length  $L^*$  will be detailed. The results for the Square Sink will be discussed followed by the results for the Spiral Sink and both heat sink thermal performances will be compared. The pressure drop over the Square Sink will also be compared to the pressure drop over the Spiral Sink during two-phase segmented flow. The effect of slug length, void fraction and liquid film on heat transfer enhancement will be discussed. All experimental data are presented graphically with respect to the dimensionless groups mentioned in Appendix B.

### 4.2 Data Reduction

This section will detail the reduction of experimental data into dimensionless groups so that thermal performances can be analyzed. The main dimensionless groups used in the comparison of thermal performances will be the dimensionless heat transfer given as  $q^*$  and the dimensionless length given as  $L^*$ . The results are available in Appendix B. The dimensionless heat transfer is given by Eq. (4.1):

$$q^* = \frac{\left( \frac{q_{\text{Bulk}}}{A_s \alpha_l} \right) D_h}{k_l (T_s - T_i)} \quad (4.1)$$

where  $q^*$  is the dimensionless heat transfer,  $q_{\text{Bulk}}$  is the total heat transfer to the working fluid,  $A_s$  is the total inside surface area of the heat sink,  $\alpha_l$  is the liquid fraction,  $D_h$  is the hydraulic diameter of the channel,  $k_l$  is the liquid phase thermal conductivity,  $T_s$  is the average surface temperature of the heat sink and  $T_i$  is the inlet temperature of the coolant. The hydraulic diameter is given by Eq. (4.2):

$$D_h = \frac{4A}{P} \quad (4.2)$$

where  $A$  is the cross-sectional area and  $P$  is the perimeter of the cross-sectional area. Note that for a square shaped cross-sectional area, the hydraulic diameter simply becomes the side length of the square. This is the case for both the Square and Spiral Sinks since both cross-sections are the same size and shape. The bulk heat transfer to the working fluid is calculated one of two ways. The first method is calculating the heat transferred to the working fluid using Eq. (4.3):

$$q_{\text{Bulk}} = \dot{m} c_p (T_o - T_i) \quad (4.3)$$

where  $c_p$  is the specific heat of the working fluid,  $T_o$  is the outlet temperature of the working fluid and  $\dot{m}$  is the mass flow rate of the working fluid calculated by Eq. (4.4):

$$\dot{m} = \rho_l Q_l \quad (4.4)$$

where  $Q_l$  is the volumetric flow rate of liquid and  $\rho_l$  is the liquid density. The second way of calculating  $q_{\text{bulk}}$  would be to calculate the heat lost to the surroundings then subtract the losses from the power input to the heat sink. This would be expressed as Eq. (4.5):

$$q_{\text{Bulk}} = q_{\text{in}} - \left( \frac{T_s - T_{\text{sur}}}{R_{\text{sur}}} \right) \quad (4.5)$$

where  $q_{in}$  is the power input to the heat sink,  $T_{sur}$  is the room temperature and  $R_{sur}$  is the thermal resistance to the surroundings calculated through experiments detailed in Chapter 3. The comparison of both bulk heat transfers to the working fluid is important and will be made by comparing Eq. (4.3) to Eq. (4.5) for each set of experimental data. The reduction using Eq. (4.3) should be accurate for single phase flows since the thermocouples taking the temperature measurements are completely immersed in the working fluid at all times whereas the reduction using Eq. (4.5) should be more accurate for segmented flows since the thermocouples taking the temperature measurements are alternating between liquid slug and gas slug and therefore obtaining an average temperature.

The average surface temperature of each heat sink is taken from four thermocouple measurements. Each thermocouple is located in the center of each of the four quadrants on the cover plate of the heat sink. The average surface temperature of the heat sink is given as Eq. (4.6):

$$T_s = \frac{T_{CH3} + T_{CH4} + T_{CH5} + T_{CH6}}{4} \quad (4.6)$$

where the subscript notation indicates the respective channel that each thermocouple was interfaced to on the data acquisition unit. The liquid fraction is calculated from the digital photographs taken of segmented two-phase flow during experiments. The photographs were analyzed and the length of liquid and gas slugs in the segmented flow was measured. The liquid fraction was calculated using Eq. (4.7):

$$\alpha_l = \frac{L_l}{L_l + L_g} \quad (4.7)$$

where  $L_l$  and  $L_g$  are the lengths of the liquid and gas slugs.

The dimensionless length  $L^*$  is a measure of how thermally developed the flow is. Large values of dimensionless length correspond to the fluid being fully thermally developed.

thus the capacity for heat transfer is low. Small values of dimensionless length correspond to the fluid thermally developing, therefore the capacity for heat transfer is higher. The dimensionless length is defined as Eq. (4.8):

$$L^* = \frac{(L/D_h)}{Pe} \quad (4.8)$$

where  $L$  is the total channel length and  $Pe$  is the Peclet number defined to be the ratio of the rate of advection of a physical quantity by the flow to the rate of diffusion of the same quantity driven by an appropriate gradient. The Peclet number is given by Eq. (4.9):

$$Pe = Re_{D_h} Pr \quad (4.9)$$

where  $Re_{D_h}$  is the Reynolds number (using the hydraulic diameter as its length scale) and  $Pr$  is the Prandtl number. The Reynolds number represents the ratio of viscous forces to that of inertial forces and is given by Eq. (4.10):

$$Re_{D_h} = \frac{\rho_l u_l D_h}{\mu_l} \quad (4.10)$$

where  $u_l$  is the liquid velocity and  $\mu_l$  is the liquid viscosity. The liquid velocity is calculated using Eq. (4.11):

$$u_l = \frac{Q_l}{A \alpha_l} \quad (4.11)$$

The Prandtl number is defined as the ratio of momentum diffusivity and thermal diffusivity and is given by Eq. (4.12):

$$Pr = \frac{c_p \mu_l}{k_l} \quad (4.12)$$

The Nusselt number is defined as the overall dimensionless heat transfer coefficient and is based on the log mean temperature difference (LMTD). The expression for Nusselt number is given by Eq. (4.13):

$$\text{Nu} = \frac{\left( \frac{q_{\text{Bulk}}}{A_s \alpha_j} \right) D_h}{k_j \Delta T_{\text{LMTD}}} \quad (4.13)$$

where the log mean temperature difference (LMTD) is defined by Eq. (4.14):

$$\Delta T_{\text{LMTD}} = \frac{(T_s - T_o) - (T_s - T_i)}{\left( \ln \left( \frac{T_s - T_o}{T_s - T_i} \right) \right)} \quad (4.14)$$

During gas-liquid or liquid-liquid two-phase segmented flow a liquid film surrounds the gas or immiscible liquid phase. The dimensionless group termed the Capillary number controls the film thickness. This has been studied and verified by Taylor (1961), Yu et al. (2007) and Fries et al. (2008). The film thickness will be compared to the thermal boundary layer thickness for certain segmented flow experimental results. The Taylor model proposed for calculating the film thickness as a function of Capillary number is given by Eq. (4.15):

$$\frac{\delta}{r_{\text{eq}}} = \frac{1.34 \text{Ca}^{2/3}}{1 + 3.35 \text{Ca}^{2/3}} \quad (4.15)$$

where  $\delta$  is the film thickness,  $r_{\text{eq}}$  is the equivalent radius and  $\text{Ca}$  is the Capillary number that is defined as the relative effect of viscous forces versus surface tension acting across an interface between a liquid and a gas, or between two immiscible liquids. The Capillary number is defined by Eq. (4.16):

$$\text{Ca} = \frac{u_1 \mu_1}{\sigma} \quad (4.16)$$

where  $\sigma$  is the surface tension of the liquid. The model in Eq. (4.16) is valid for a range of Capillary numbers given as  $10^{-3} < Ca < 1.4$ . The equivalent radius appearing in Eq. (4.15) is calculated for a square channel cross-sectional area using Eq. (4.17):

$$r_{eq} = \frac{a}{\sqrt{\pi}} \quad (4.17)$$

where  $a$  is the side length of the square. An approximation for the thermal boundary layer thickness can be derived through the use of scaling analysis (order of magnitude analysis) presented by Bejan (2005). Given that the coefficient of heat transfer is proportional to ratio of conductivity to thermal boundary layer thickness, one can write the following:

$$h \approx \frac{k}{\delta_t}$$

Next the Nusselt number is proportional to the following expression:

$$Nu \approx \frac{h D_h}{k}$$

But substitution of the latter two expressions and the fully developed limit for Nusselt number, the approximation for thermal boundary layer thickness is obtained and is given by Eq. (4.18):

$$\delta_t = \frac{D_h L^* \frac{1}{3}}{1.55} \quad (4.18)$$

where  $\delta_t$  is the thickness of the thermal boundary layer at a given value of dimensionless length  $L^*$ . Analysis of the film thickness and thermal boundary layer thickness is important for viscous fluids such as oil and will be detailed later in this chapter.

## 4.3 Experimental Results

### 4.3.1 Introduction

This section will detail all the experimental results from single and two-phase flow experiments. The results will be presented graphically and conclusions will be drawn on the thermal performances. The results for the Square Sink will be presented followed by the results for the Spiral Sink. A discussion on the effect of slug length and void fraction will be presented followed by the comparison of overall efficiencies of the Square Sink and Spiral Sink taking into account pressure drop. While only several graphical results will be displayed in this chapter, all results can be found in Appendix B.

### 4.3.2 Square Sink Results

The first experiment run with the Square Sink was single phase flow of water. The flow rate was varied through 17 different values ranging from 2.25 ml/min to 120 ml/min and the liquid Reynolds numbers corresponding to this range of flow rates was  $69.4 < Re < 2262$ . Note that only the very last flow rate of 120 ml/min lead to a turbulent flow Reynolds number while all other 16 values were within the laminar flow regime. The input power to the heat sink was set at approximately 10.0 Watts initially, but was recorded at steady state condition for each flow rate due to a small drift in the initial value. The dimensionless parameters were calculated for all 17 data sets then plots of  $q^*$  vs.  $L^*$  and  $Nu$  vs.  $L^*$  were created. The dimensionless heat transfer  $q^*$  vs. dimensionless length  $L^*$  is shown in Figure 4.1. The solid line in Figure 4.1 corresponds to the model presented by Muzychka et al. (2009) for a channel with square cross-sectional area given by Eq. (4.19):

$$q^* = \left[ \left( \frac{1.55}{L^{*3}} \right)^{\frac{3}{2}} + \left( \frac{1}{4L^*} \right)^{\frac{3}{2}} \right]^{\frac{2}{3}} \quad (4.19)$$

The open circle data points correspond to using Eq. (4.3) for bulk heat transfer when calculating the dimensionless heat transfer  $q^*$  while the solid circle data points correspond to using Eq. (4.5) for bulk heat transfer when calculating  $q^*$ . As shown in Figure 4.1, the experimental data points follow the model trend very well. For small values of dimensionless length  $L^* < 0.04$  (corresponding to high flow rates and thermally developing flow) the data points pull away from the model. This trend may be explained by the fact that the mini-channel heat sink utilized had many bending channels with  $90^\circ$  turns whereas the model proposed by Muzychka et al. (2009) was for a straight channel with square cross-sectional area.

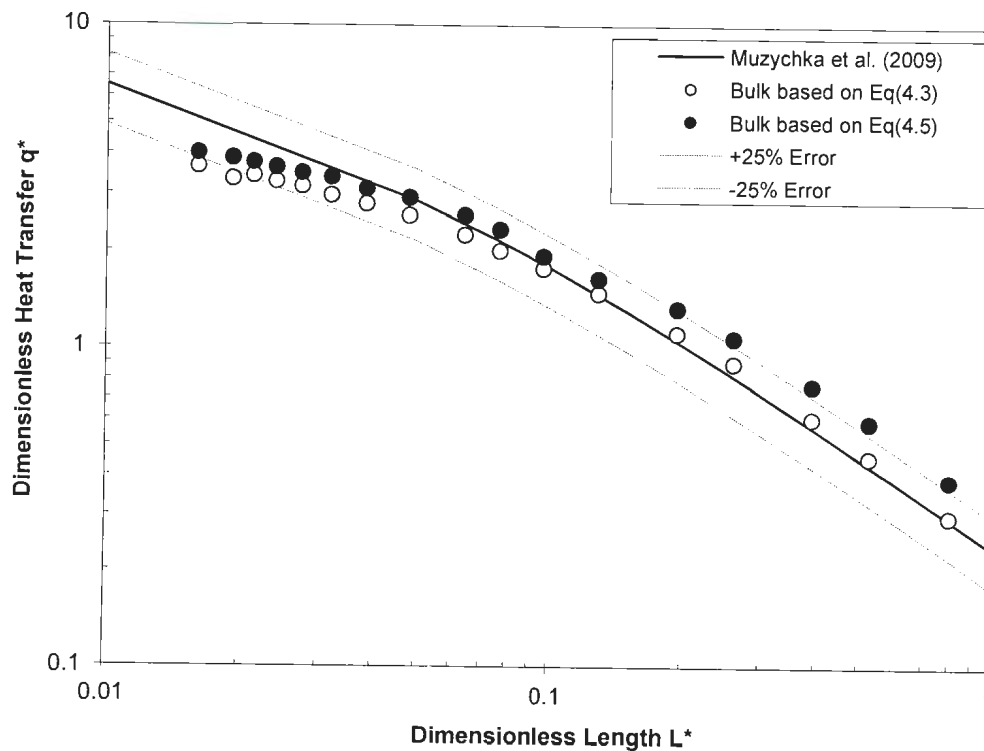


Figure 4.1 – Results for Single Phase Water in Square Sink.

For thermally developing flow perhaps the meandering channels affect the flow in such a way that lower heat transfer results. The remaining data points for  $L^* > 0.04$  fit the model nicely and large values of  $L^*$  using Eq. (4.3) as bulk heat transfer (the open circles) fall

directly on the model line (corresponding to low flow rates and thermally fully developed flow). A larger plot of Figure 4.1 is available in Appendix B.

The single phase flow results shown in Figure 4.1 serve two purposes, first they act as a means of comparison of two-phase segmented flow results to some relative base and secondly they were used to give some idea of how the heat sink system was performing. The fact that the open circle data points follow the model trend nicely for  $L^* > 0.04$  show that the system is performing properly and that experimental readings are correct within experimental uncertainty (discussed in Chapter 3). The open circle data based on data reduction using Eq. (4.3) are the more accurate of the two sets of data for single phase flow of water, since the inlet and outlet thermocouples are completely immersed at all times by the flow at a constant temperature once steady state was achieved. Therefore it is reasonable to assume the solid circle data based on Eq. (4.5) would over predict the model for single phase flow and it is shown clearly in Figure 4.1 that this is indeed the case.

The second set of experiments conducted using the Square Sink was two-phase segmented flow of water-air using the 0.020 inch T-junction for generating longer slug lengths. The flow rates of water and air were varied and 8 different combinations of flow rates were recorded. The water ranged from 2.0 ml/min to 4.0 ml/min and the air ranged from 1.0 ml/min to 4.0 ml/min. The liquid Reynolds number corresponding to the flow rates ranged from  $61 < Re < 155$  which was well within the laminar flow regime. These low flow rates were chosen so that the photographs obtained of the liquid slugs would not be blurred (as any higher flow rates would have lead to blurry images). Due to the lower flow rates, the power input to the heat sink was subsequently decreased to an initial value of 2.5 Watts and was recorded at each steady state condition for a given combination of flow rates. This was done to ensure the heat sink would not reach high temperatures (i.e. 90-100 °C). The results from the 8 experimental runs are presented as a plot of  $q^*$  vs.  $L^*$  in Figure 4.2. The open and solid circle data points again correspond to using Eq. (4.3) or Eq. (4.5) when calculating bulk heat transfer during reduction of data. It is important to

note that for two-phase segmented flow, the solid circle data points are more accurate of the two data sets, due to the fact that the outlet thermocouple is reading an average temperature of the slug flow rather than the actual constant temperature of the liquid phase.

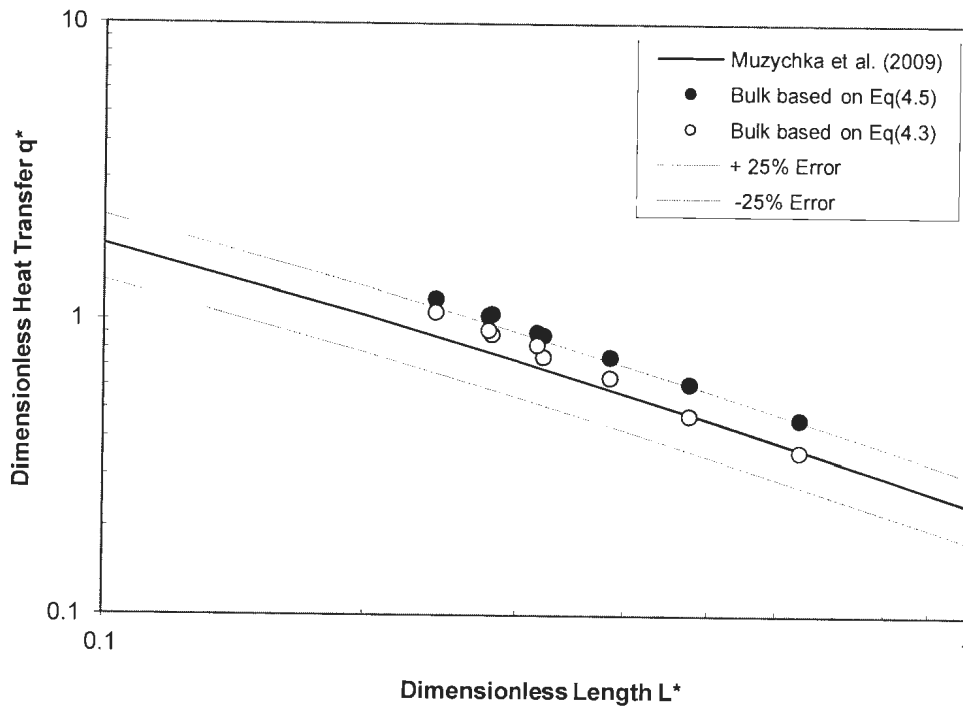


Figure 4.2 – Results for Two-Phase Water-Air (Long Slugs) in Square Sink.

As the slug of liquid passes over the thermocouple wire, the wire will increase in temperature, as the slug of gas passes over the thermocouple wire, it will decrease in temperature. Since the liquid phase is responsible for the heat transfer only the liquid phase temperature is important. Unfortunately there was no accurate method to measure the temperature of each liquid slug, therefore it was necessary to consider bulk heat transfer two ways using Eq. (4.3) and Eq. (4.5). It is clearly shown that in Figure 4.2 if the data points for either set of open or solid circles are considered; there is an enhancement in the dimensionless heat transfer. If the open circle data is analyzed alone, at high values of dimensionless length ( $L^* > 0.4$ ) it is shown that the segmented flow

performs according to the model, but for lower values of dimensionless length ( $L^* < 0.4$ ) the experimental data rises and becomes approximately 21% higher than the model.

If the solid circle data is considered, enhancement is shown for all data points. The highest level of enhancement shown for each set of data points is 21% for the open circles and 35% for the solid circles. The average enhancement over the model for each set of data is 11% for the open circles and 31% for the solid circles. As previously stated, in the analysis of the experimental data for segmented flow, it is suspected that reduction based on Eq. (4.5) is more accurate than reduction based on Eq. (4.3). In reality, the exact value is somewhere between the two data sets. If an estimation based on a mean average between the open and solid circle data was considered, then a mean average enhancement of 21% occurs when using two-phase segmented flow of water-air in the Square Sink. A larger plot of Figure 4.2 is available in Appendix B.

The third set of experiments conducted with the Square Sink was single phase flow of canola oil. The flow rate of oil was varied 10 times resulting in a range of flow rates from 3.0 ml/min to 20.0 ml/min. The Reynolds numbers corresponding to this range of flow rates are  $0.8 < Re < 5.6$  and are well within the laminar regime. The power input to the system was initially set at 2.5 Watts and was recorded at each steady state condition. The experimental results from the single phase oil are shown in Figure 4.3 as a plot of  $q^*$  vs.  $L^*$ .

The open and closed circle data points correspond to the use of Eq. (4.3) and Eq. (4.5) in the reduction of data. As with the single phase flow of water, the open circle data points are most likely the more accurate prediction of actual performance, since the thermocouples are completely immersed in the fluid at steady state. Analysis of the open circle data points in Figure 4.3 show good agreement with the model proposed by Muzychka et al. (2009) over most values of dimensionless length with the exception of

the data point at  $L^* = 0.04$ . At this value of dimensionless length the data point has a dimensionless heat transfer value that is 11% higher than the model.

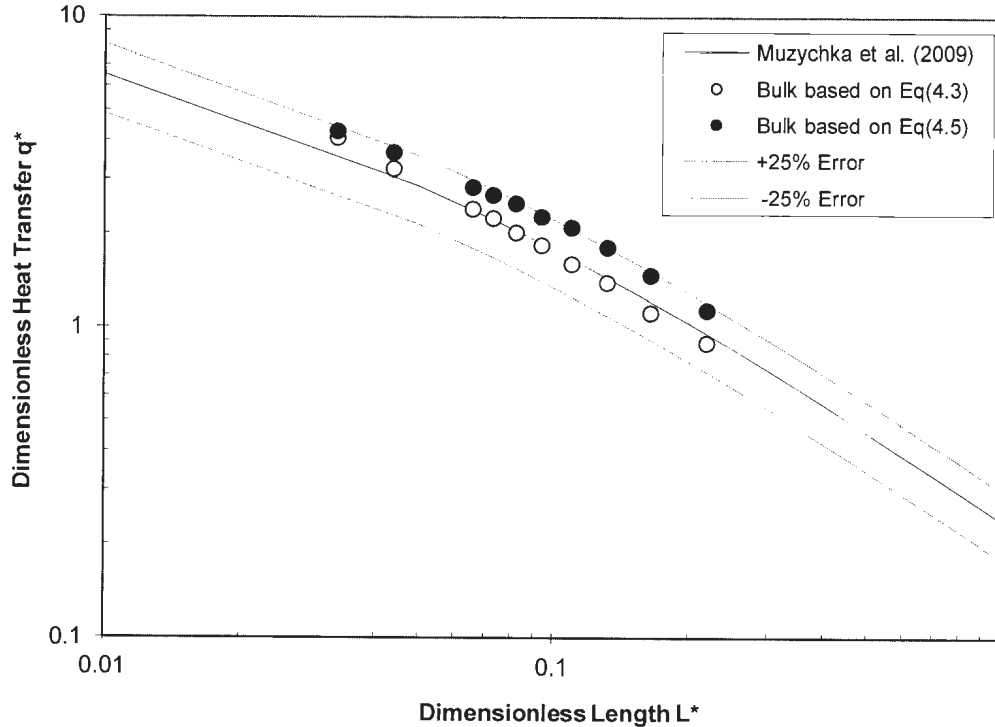


Figure 4.3 – Results for Single Phase Oil in Square Sink.

One reason for this difference may be due to the properties used for canola oil. The thermophysical properties for canola oil taken from Przybylski (2000) were listed at room temperature and no equations were given to calculate the properties given the temperature of the canola oil, therefore the properties used for data reduction were constant values for all data points. In reality the properties change slightly with the temperature and this could account for the minor differences seen between the open circle data points and the model. Overall the single phase canola oil results are in good agreement with the model when based on Eq. (4.3). As expected when the data is reduced based on Eq. (4.5) the model is over predicted, this was also seen with single phase flow of water. A larger plot of Figure 4.3 can be found in Appendix B.

The fourth set of experiments conducted on the Square Sink was two-phase segmented flow of oil-air using the 0.020 inch T-junction for generating longer slug lengths. The oil and air flow rates were varied to obtain 10 combinations of different flow rates. The oil flow rate ranged from 3.0 ml/min to 4.0 ml/min and the air flow rate ranged from 0.5 ml/min to 4.0 ml/min. The liquid Reynolds number corresponding to this range of oil flow rates was  $0.97 < Re < 2.5$  which was well within the laminar regime. Due to the lower oil flow rates, the power input to the heat sink was set to an initial value of 2.5 Watts and was recorded at each steady state condition for each given combination of flow rates. The results for the 10 experimental runs using oil-air are presented as a plot of  $q^*$  vs.  $L^*$  in Figure 4.4.

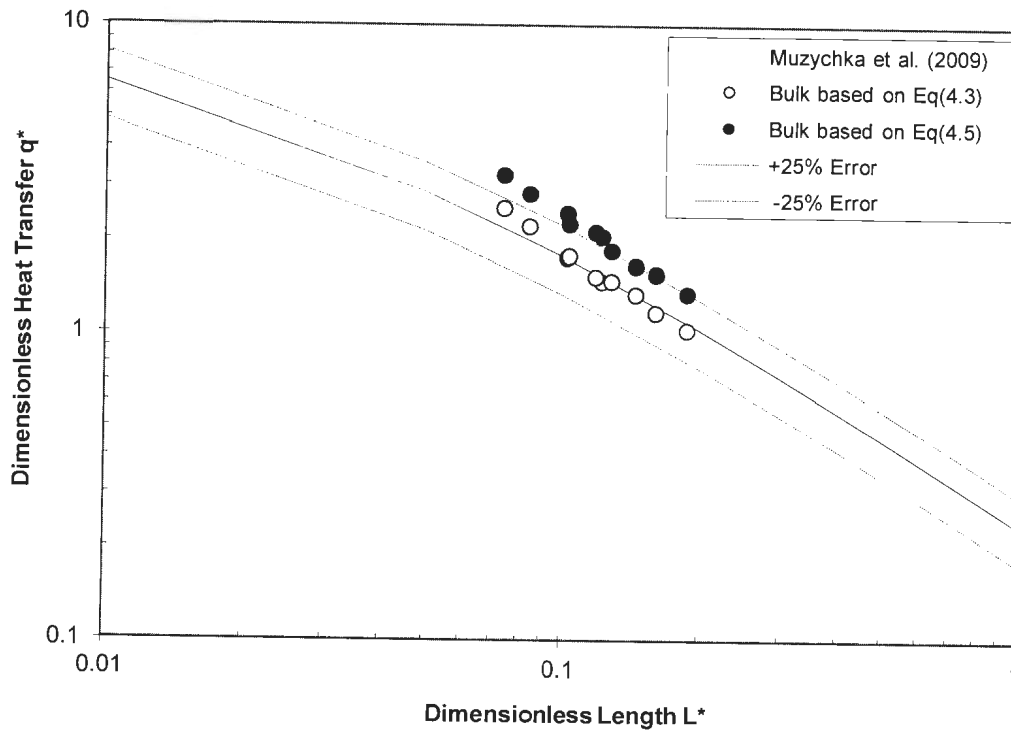


Figure 4.4 – Results for Two-Phase Oil-Air in Square Sink.

Again, the open and closed circle data in Figure 4.4 correspond to the use of Eq. (4.3) and Eq. (4.5) in the reduction of data. As with the two-phase segmented flow of water-air, the solid circle data points are likely the more accurate prediction of actual performance, since the thermocouples in slug flow are not constantly immersed in the liquid phase.

However this may not be entirely accurate for the oil phase either, since the thermal boundary layer is quite thin and may not penetrate through the liquid film surrounding the gas slugs, this will be detailed later. With the assumption that the thermal boundary layer is indeed thick enough to fully develop, then exact answer lies somewhere between the open and closed circle data. It is clear that the open circle data points fall close to the model proposed by Muzychka et al. (2009) with two exceptions, the two data points with dimensionless length  $L^* < 0.084$  fall above the model and respectively give an enhancement of 10% and 15%. Analysis of the solid circle data points results in enhancement over all values of dimensionless length, the highest enhancement being 47% when  $L^* = 0.074$ . The average enhancement over the model for each data set is 1% for the open circles and 32% for the solid circles. As previously stated, the true enhancement lies somewhere between, and the average mean enhancement when combining both data sets is 17%. A larger plot of Figure 4.4 is available in Appendix B.

The final experiment conducted using the Square Sink was again two-phase flow of water-air but this time the 0.0625 inch T-junction was used for creating shorter slug lengths. Comparing the results from both two-phase segmented water-air flow experiments (one using the 0.020 inch T-junction the other using the 0.0625 inch T-junction) will show the effect of slug length, this will be discussed later in this chapter. The flow rates of water and air were varied leading to 18 combinations of flow rates. The water flow rate ranged between 3.0 ml/min to 10.0 ml/min and the air flow rate ranged from 1.0 ml/min to 10.0 ml/min. The liquid Reynolds number corresponding to the range of water flow rates was  $79 < Re < 363$  which was within the laminar flow regime. The power input to the heat sink was set initially at 2.5 Watts and was recorded at each steady state condition. The results are presented as a plot of  $q^*$  vs.  $L^*$  given by Figure 4.5.

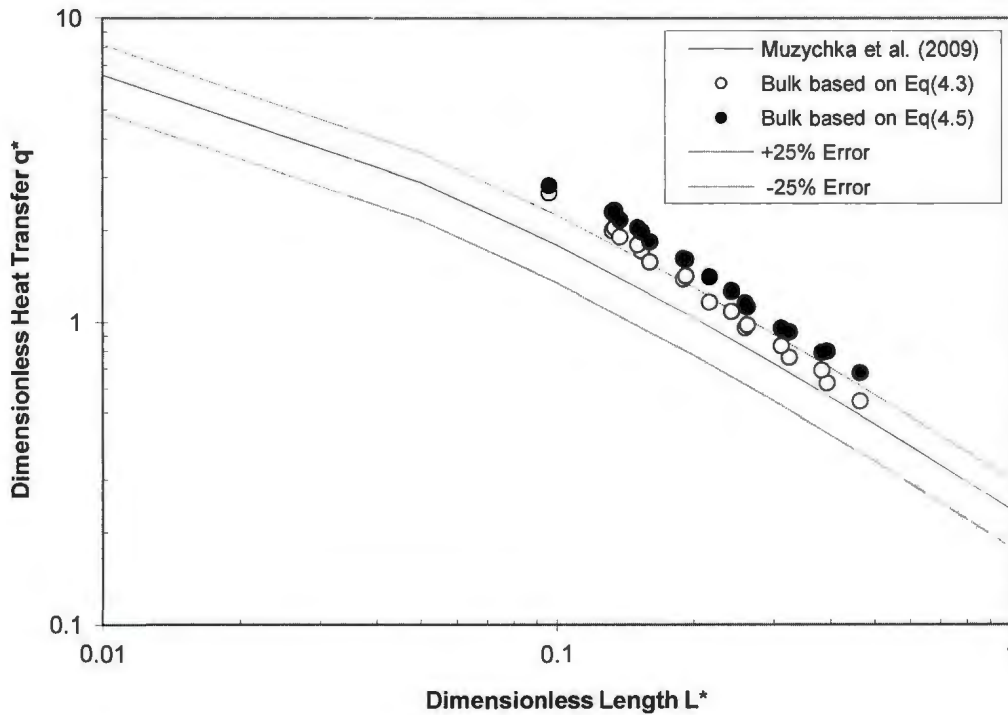


Figure 4.5 – Results for Two-Phase Water-Air (Short Slugs) in Square Sink.

Analysis of Figure 4.5 clearly shows open circle data based on Eq. (4.3) and solid circle data based on Eq. (4.5) result in overall heat transfer enhancement over the entire range of dimensionless length values considered for water-air segmented flow with short slug lengths. Continue to note that the solid circle data points are more accurate for segmented flow, while the actual result lies somewhere between both data sets. The highest enhancement occurring over the proposed model by Muzychka et al. (2009) is 44% for the open circle data and 63% for the solid circle data. The average enhancement over the model for the entire range of dimensionless length is 26% for the open circle data and 46% for the solid circle data. Again, the true enhancement lies somewhere between both data sets, and the average mean enhancement when combining both data sets is 36%.

### 4.3.3 Spiral Sink Results

The experimental results obtained from the testing of the spiral sink will be presented in this section. All the results will be compared to the model proposed by Muzychka et al. (2009) for dimensionless heat transfer in the channel with square cross-sectional area, given by Eq. (4.18). Since the slug length was shown to be a controlling factor in the dimensionless heat transfer enhancement due to segmented flow through experimentation with the Square Sink, it was chosen to run the shorter slugs (higher thermal performance) for all segmented flow tests with the Spiral Sink. However, single phase flow results are still necessary as a baseline to compare the two-phase segmented flow results with. Additionally, due to the poor performance of canola oil, it was left out of the testing of the Spiral Sink. Instead, several new interests arose. First, what would be the result of running the fluid both ways through the Spiral Sink. This required two sets of tests for single phase water and two-phase segmented flow of water-air. The first set of tests would run the working fluid through the Spiral Sink with the inlet being the middle port of the spiral, and the working fluid would exit out the side port. This was termed running the fluid forwards through the Spiral Sink. The second set of tests would run the working fluid the opposite way, with the fluid entering the side port and leaving through the middle port. This was termed running the fluid backwards through the Spiral Sink.

The first experiment conducted was single phase flow of water forwards through the Spiral Sink (i.e. the middle port being the inlet and side port being the outlet). The flow rate of water was varied 17 times between 2.5 ml/min to 120 ml/min and the Reynolds numbers corresponding to this range of flow rates were  $59 < Re < 2268$ . As with single phase flow of water in the Square Sink, the last data point having a flow rate of 120 ml/min and a Reynolds number of 2268 was in the turbulent flow regime, while all other 16 data points were in the laminar flow regime. The power input to the Spiral Sink was set 7.5 Watts and was recorded at each steady state condition due to a small drift in the value. The experimental results are presented as a plot of  $q^*$  vs.  $L^*$  given by Figure 4.6.

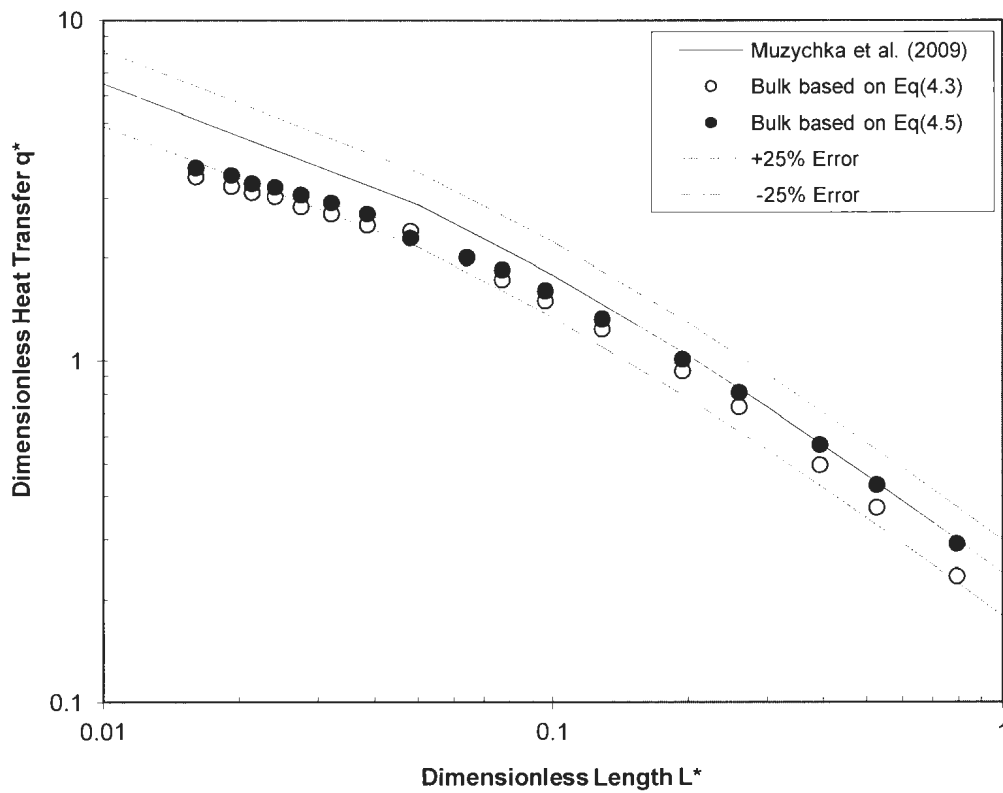


Figure 4.6 – Results for Single Phase Water in Spiral Sink (Forwards).

The experimental results in Figure 4.6 are surprising because published literature such as Horvath et al. (1973) claimed that coiled or spiralling channels enhance heat transfer above that of straight channels, but the experimental data points for both sets of data, reduced using Eq. (4.3) and Eq. (4.5), fall below the model proposed by Muzychka et al, (2009). Even the solid circle data which is considered an over prediction of the system for single phase flows falls short of the model line. On a positive note the data for both open and solid circles follows the same trend as the model line, and like the single phase flow of water in the Square Sink, the Spiral Sink experimental results seem to pull away from the model at lower values of dimensionless length,  $L^* < 0.04$ . The reason why both data sets pull away from the model over all values of dimensionless length cannot be due to experimental error because the results from the single phase flow of water through the Square Sink agreed too well with the model. The difference between the Spiral Sink results is most likely due to system geometry. The Spiral Sink has completely different

geometry and the fluid feels the effects of centrifugal forces as it flows around the spiral channel, whereas the model proposed doesn't account for this, in fact the only similarity between the Spiral Sink and the model is that the cross-sectional area is square. Therefore, these results for single phase water (forwards) through the Spiral Sink will act as reference point to which two-phase segmented flow (forwards) through the Spiral Sink will be compared with. The experimental results for the Spiral Sink on average under predict the model by 22% for the open circle data and 15% for the solid circle data. A larger plot of Figure 4.6 can be found in Appendix B.

The second set of experiments conducted using the Spiral Sink was single phase flow of water backwards through the sink (i.e. the side port being the inlet and the middle port being the outlet). The inlet tubing from the syringe pumps to the heat sink was switched to the side port and the outlet tubing to the discharge tank was switched to the middle port, thus reversing the flow direction. The flow rate of water was varied 17 times ranging from 2.5 ml/min to 120 ml/min and the corresponding Reynolds numbers were  $59 < Re < 2120$ . As with the last set of experiments, only the flow rate of 120 ml/min was within the turbulent flow regime and all other 16 points fell within the laminar flow regime. The power input was again set initially at 7.5 Watts and recorded when the steady state conditions were. The experimental results presented as a plot of  $q^*$  vs.  $L^*$  for single phase flow of water through the Spiral Sink backwards are shown in Figure 4.7. As with the experimental results for single phase flow of water (forwards), the experimental results for single phase flow of water (backwards) through the Spiral Sink shown in Figure 4.7 are just as surprising.

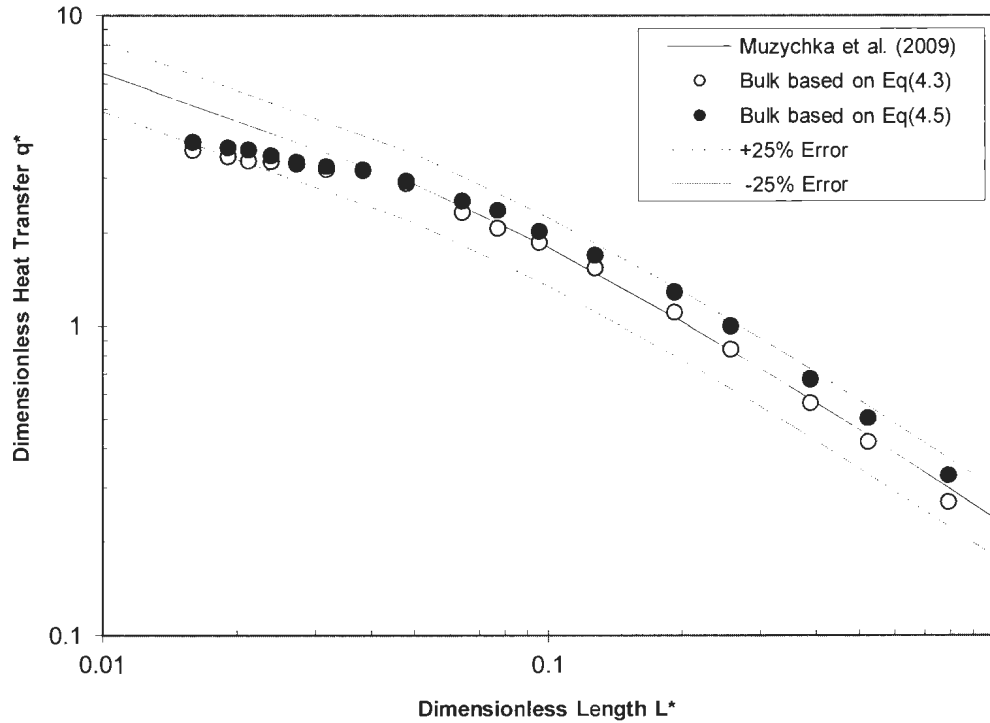


Figure 4.7 – Results for Single Phase Water in Spiral Sink (Backwards).

Observing the open and solid circle data points it can be seen that both sets of data follow the model closely until the dimensionless length becomes  $L^* < 0.04$  where both sets of data pull away from the model. Again, this trend has been shown for all single phase flow of water through both heat sink systems. The open circle data points on average under predict the model by 10% whereas the solid circle data points predict the model with 0% average difference. The most interesting feature to note is that the dimensionless heat transfer obtained has a dependency on the direction of flow through the sink (i.e. being forwards or backwards). This will be addressed later in this chapter. These results for single phase flow of water (backwards) through the Spiral Sink will act as a reference point to which the two-phase segmented flow (backwards) results will be compared too. A larger plot of Figure 4.7 as can be found in Appendix B.

The third set of experimental runs conducted with the Spiral Sink was two-phase segmented flow of water-air (forwards) using the 0.0625 inch T-junction for the generation of short slug lengths. The flow rates of water and air were varied for 18 combinations of flow rates. The water flow rate ranged from 3.0 ml/min to 10.0 ml/min and the air flow rate ranged from 1.0 ml/min to 10.0 ml/min. The liquid Reynolds numbers corresponding to the combinations of flow rates ranged from  $79 < Re < 374$  which is well within the laminar flow regime. The power input to the sink was initially set at 2.5 Watts and was recorded at each steady state condition. The experimental results presented as a plot of  $q^*$  vs.  $L^*$  for two-phase segmented flow of water-air through the Spiral Sink (forwards) are shown in Figure 4.8.

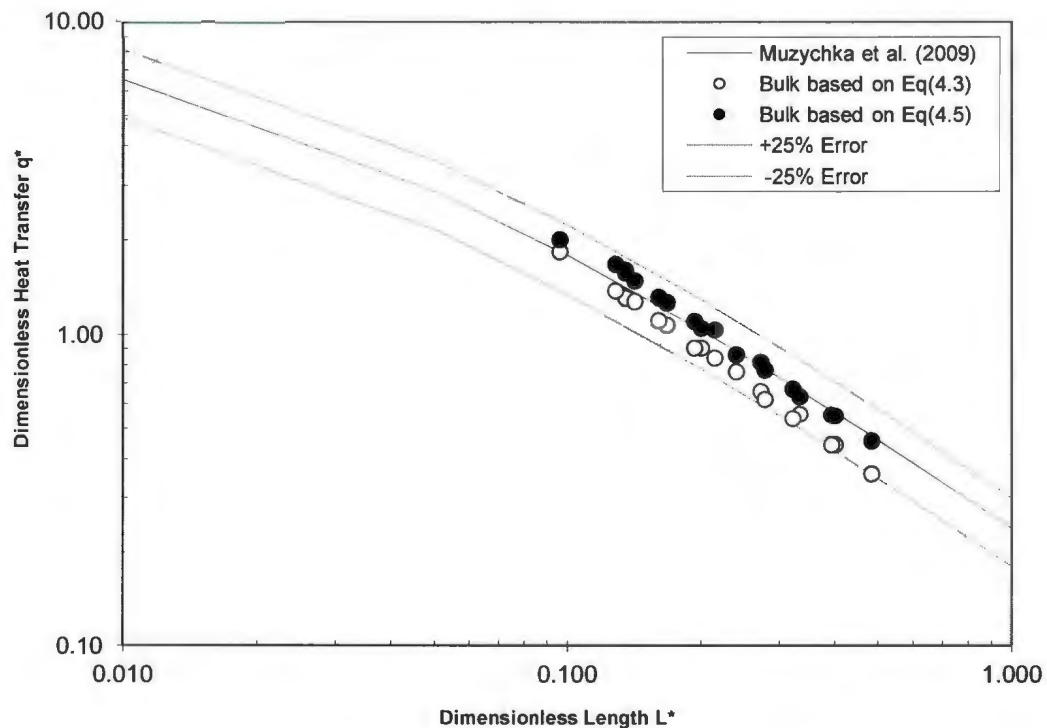


Figure 4.8 – Results for Two-Phase Water-Air in Spiral Sink (Forwards).

The results shown in Figure 4.8 for both open and solid circle data sets based on reduction of data using Eq. (4.3) and (4.5) again under predict the model on average. The open circle data points under predict the model by 13% on average, while the solid circle data points under predict the model by 1% on average. Note that the model is not a good

baseline reference for comparison, since it has already been shown that single phase flow through the Spiral Sink doesn't fall on the model line well. Therefore, the comparison between single phase flow and two-phase segmented flow for the Spiral Sink will be conducted using the single phase experimental results as the baseline for comparison. This comparison between single and two-phase flow will be conducted later in this chapter. As previously mentioned the solid circle data points are the better predictor for segmented flow since the open circle data points are based of experimental readings of alternating slug temperatures. The actual true value lies somewhere between the open circle data and solid circle data. If a mean average value is taken then the two-phase segmented flow in the Spiral Sink (forwards) under predicts the model on average by 7%. A larger plot of Figure 4.8 as well as a plot of  $Nu$  vs.  $L^*$  can be found in Appendix B.

The final set of experimental runs conducted in the Spiral Sink was two-phase segmented flow of water-air (backwards) using the 0.0625 inch T-junction for generating shorter slug lengths. Again the inlet and outlet ports were switched on the Spiral Sink to allow the flow to reverse directions through the sink. The flow rates of water and air were varied for 18 combinations of flow rates. The water flow rate ranged from 3.0 ml/min to 10.0 ml/min and the air flow rate ranged from 1.0 ml/min to 10.0 ml/min. The liquid Reynolds numbers corresponding to the combinations of flow rates ranged from  $79 < Re < 391$  which is well within the laminar flow regime. The power input to the sink was initially set at 2.5 Watts and was recorded at each steady state condition. The experimental results presented as a plot of  $q^*$  vs.  $L^*$  for two-phase segmented flow of water-air through the Spiral Sink (backwards) are shown in Figure 4.9.

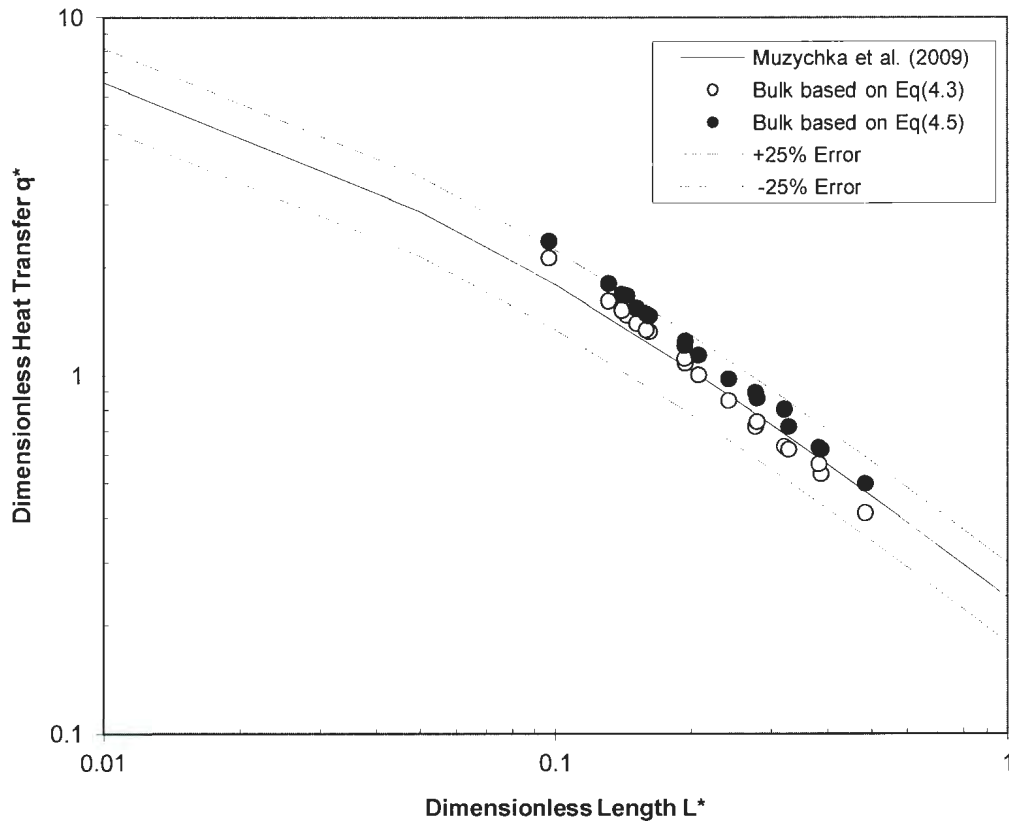


Figure 4.9 – Results for Two-Phase Water-Air in Spiral Sink (Backwards).

The experimental results clearly show that both sets of data, open and solid circles based on the reduction of data using Eq. (4.3) and Eq. (4.5), follow the model trend well. Note that in Figure 4.9 the model line is not a good baseline reference for the two-phase segmented flow performance. As stated for the last experimental study, the two-phase segmented flow of water-air (backwards) will instead be compared to the single phase flow of water (backwards) through the Spiral Sink. This comparison will be conducted later in this chapter. With respect to the model proposed by Muzychka et al. (2009) the open circle data over predicts the model by 1% on average while the solid circle data over predicts the model by 16% on average over all values of dimensionless length. Again, the actual true value lies somewhere between the open and solid circle results and taking a mean average value of the two data sets leads to an overall dimensionless heat transfer

enhancement of 8.5% over the model. A larger plot of Figure 4.9 as well as a plot of Nu vs.  $L^*$  can be found in Appendix B.

#### 4.3.4 Effect of Slug Length

The effect of liquid slug length on heat transfer enhancement can be analyzed by comparing the results from both water-air segmented flows in the Square Sink utilizing different orifice size T-junctions. By taking the square root of the sum of the flow rates squared as a reference for both long and short slugs, the dimensionless heat transfer may be plotted against this reference and the effect of slug length can be observed.

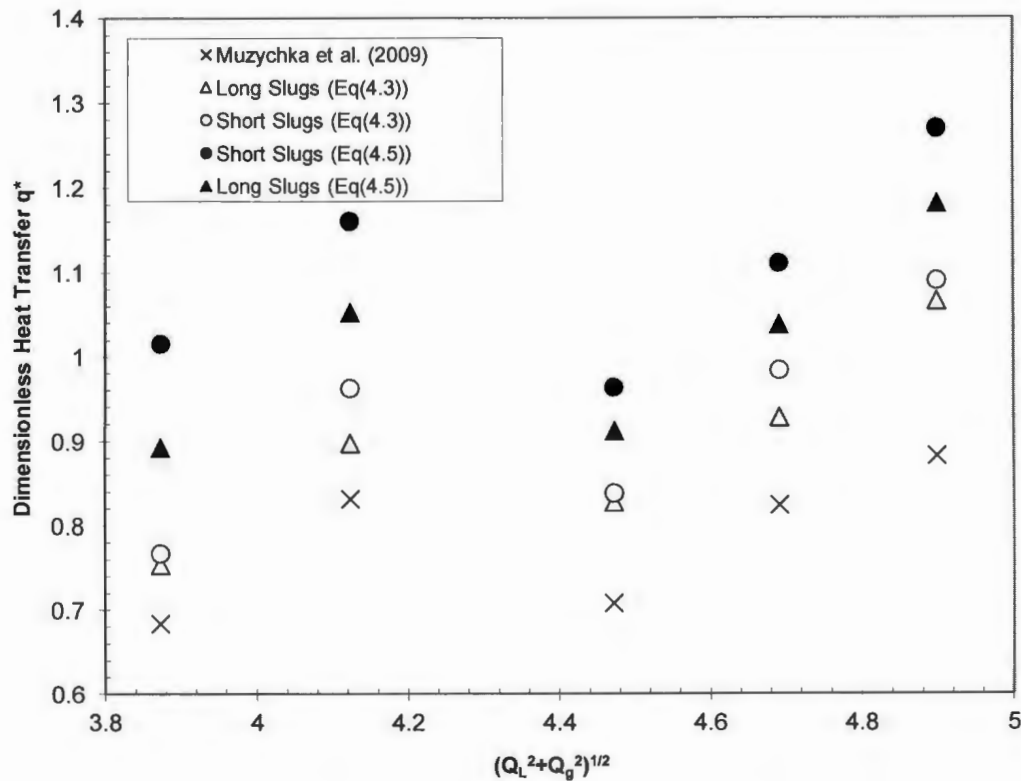


Figure 4.10 – Comparison of Long Slugs and Short Slugs in Square Sink using Two-Phase Water-Air Flow.

Five combinations of flow rates for water-air segmented flow that were the same for short and long slugs were examined. The flow rate combinations analyzed are: 3 water – 3 air, 3 water – 4 air, 4 water – 2 air, 4 water – 3 air, and 4 water – 4 air (all units are ml/min). The long liquid slugs ranged from 18 mm to 51 mm and the short liquid slugs ranged from 10 mm to 18 mm over the corresponding range of flow rates. A plot of dimensionless heat transfer versus the square root of the sum of the flow rates squared was constructed and is shown by Figure 4.10. Again the bulk heat transfer to the fluid will be considered using Eq. (4.3) and Eq. (4.5) during the reduction of data. It is clearly seen that the shorter slugs increase the dimensionless heat transfer when compared to the longer slugs at the same flow rates. Figure 4.10 also confirms that segmented flow in general increases the dimensionless heat transfer above the proposed model by Muzychka et al. (2009) for the Square Sink. The level of heat transfer enhancement over the model for the data sets used in this comparison is provided in tabular format in Table 4.1. A larger plot of Figure 4.10 is included in Appendix B.

**Table 4.1**  
**Effect of Slug Length on Heat Transfer Enhancement**

$Q_l$ (ml/min)	$Q_g$ (ml/min)	Long Slug Enhancement Eq(4.3)   Eq(4.5)	Short Slug Enhancement Eq(4.3)   Eq(4.5)
3.0	3.0	10%   31%	12%   49%
3.0	4.0	8%   27%	16%   40%
4.0	2.0	17%   29%	18%   36%
4.0	3.0	13%   26%	19%   35%
4.0	4.0	21%   34%	24%   44%

As can be seen in Table 4.1, the short slug segmented flow out performs the long slug segmented flow when comparing the dimensionless heat transfer enhancement at equal flow rate combinations. The short slug segmented flow has a mean average heat transfer enhancement of 18% and 41% when using Eq. (4.3) and Eq. (4.5) in the reduction of data. The long slug segmented flow has a mean average heat transfer enhancement of 14% and 29% when using Eq. (4.3) and Eq. (4.5) in the reduction of data.

As previously stated, when it comes to the analysis of segmented flow, the actual enhancement lies somewhere between these values. By taking a mean average between the results obtained using Eq. (4.3) and Eq. (4.5) one gets an average heat transfer enhancement over the model of 29% for short slugs and 22% for long slugs for the five data sets used in this comparison. Therefore it can be concluded that slug length is a controlling factor in the dimensionless heat transfer enhancement due to segmented flow and this agrees with the published literature.

#### **4.3.5 Effect of Flow Direction in Spiral Sink**

The effect of flow direction in the Spiral Sink will now be discussed. It was initially theorized that the Spiral Sink would give better dimensionless heat transfer values when run in the forward mode. This was due to the thought that the highest temperature of the heat sink occurs at very center for the uniform wall flux boundary condition, therefore putting the coolest fluid into the middle inlet (forwards) would lead to higher overall thermal performance. The effect of flow direction in the Spiral Sink can be analyzed by plotting the dimensionless data from the forwards and backwards experiments together for comparison. This will be done for both single and two-phase flow. The single phase and two-phase data for both flow directions are plotted as  $q^*$  vs.  $L^*$  and are shown in Figure 4.11 and Figure 4.12, respectively. Regardless of whether the data is reduced using Eq. (4.3) or Eq. (4.5), examination of Figure 4.11 and Figure 4.12 show clearly that the Spiral Sink operates in the opposite fashion initially expected. If the open data (both circles and triangles) or the solid data (both circles and triangles) are examined individually all the triangles have higher dimensionless heat transfer than their corresponding circles. The mean average enhancement of single phase flow (backwards) when compared to single phase flow (forwards) is 10% for open data and 18% for solid data.

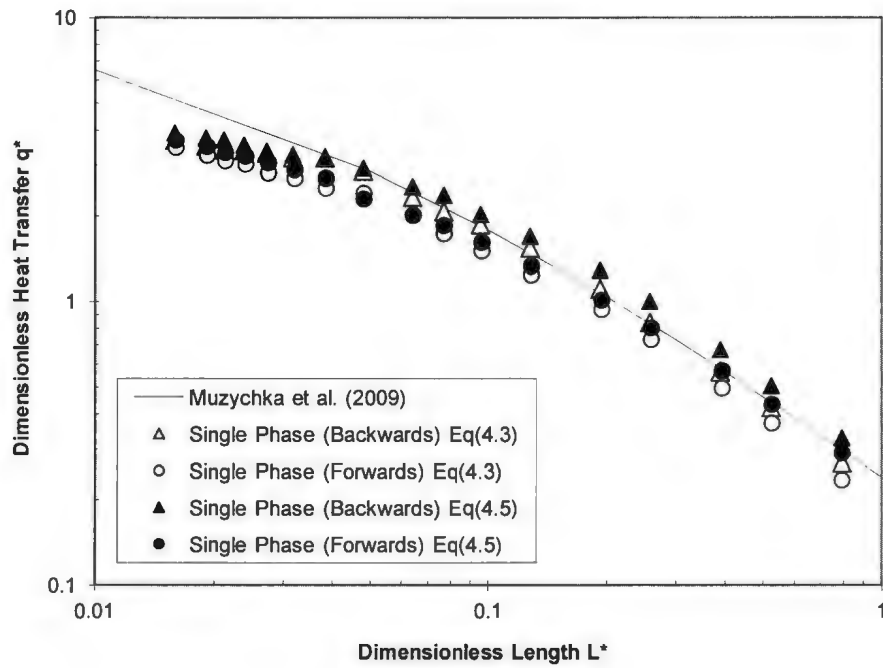


Figure 4.11 – Comparison of Flow Direction in Spiral Sink for Single Phase Flow.

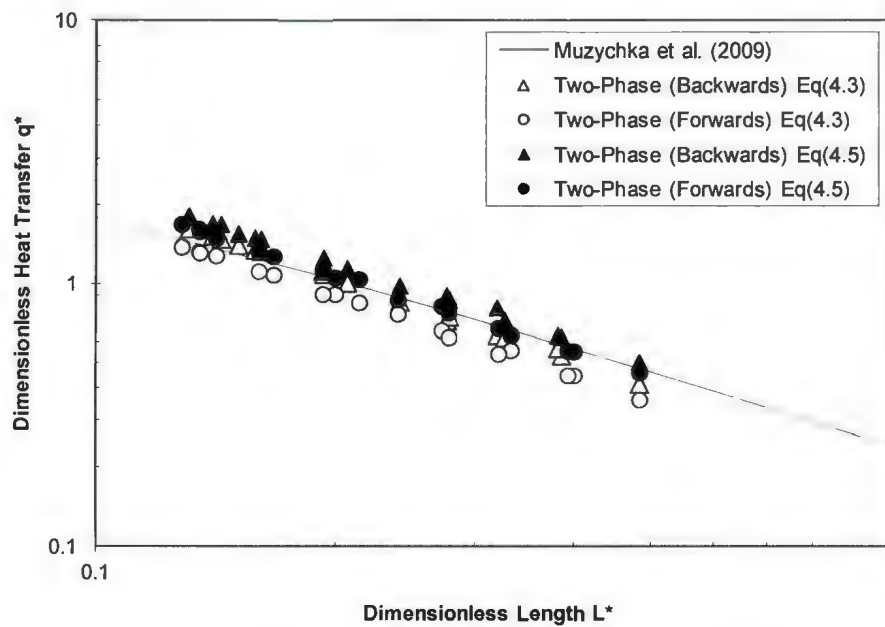


Figure 4.12 – Comparison of Flow Direction in Spiral Sink for Two-Phase Flow.

The mean average enhancement of two-phase segmented flow (backwards) when compared with two-phase segmented flow (forwards) is 17% for open data and 12% for solid data. Therefore the Spiral Sink shows thermal enhancement in backward mode when compared to forward mode at equal flow rates for all values of dimensionless length. This is true for both single and two-phase flows in the Spiral Sink. Detailed plots of Figure 4.11 and Figure 4.12 can be found in Appendix B.

#### **4.3.6 Comparison of Single and Two-Phase Flow**

The comparison of dimensionless heat transfer between single and two-phase segmented flow will be conducted and discussed in this section. The comparison will be presented in graphical format by plotting the single and two-phase flow experimental data for the Square Sink tests and the Spiral Sink tests separately. The single phase flow of water compared to the two-phase flow of water-air (short slugs) in the Square Sink will be analyzed first. The experimental results using Eq. (4.3) in the reduction of data are plotted together as  $q^*$  vs.  $L^*$  and are shown in Figure 4.13.

Analysis of Figure 4.13 concludes that the two-phase segmented flow of water-air outperforms the single phase flow of water in the Square Sink. For similar values of dimensionless length the dimensionless heat transfer values obtained when using two-phase segmented flows are significantly higher. When comparing both data sets to the model proposed by Muzychka et al. (2009) as a baseline comparison, the two-phase segmented flow experimental data over predicts the model on average by 26% whereby the single phase flow experimental data under predicts the model on average by 10%. Therefore the two-phase segmented flow for this case on average shows a 40% enhancement over the single phase flow. Similar comparisons can be made for the following cases: single phase water and two-phase water-air in the Square Sink (long slugs), single phase oil and two-phase oil-air in the Square Sink (long slugs), single phase water and two-phase water-air in the Spiral Sink (short slugs & backwards), and single phase water and two-phase water-air in the Spiral Sink (short slugs & forwards). Plots of  $q^*$  vs.  $L^*$  for each of these cases based on data reduction using Eq. (4.3) and Eq. (4.5) are

included in Appendix B. To summarize all cases Table 4.2 was constructed and shows the average enhancement seen when comparing the dimensionless heat transfer from single phase flow to that of two-phase segmented flow.

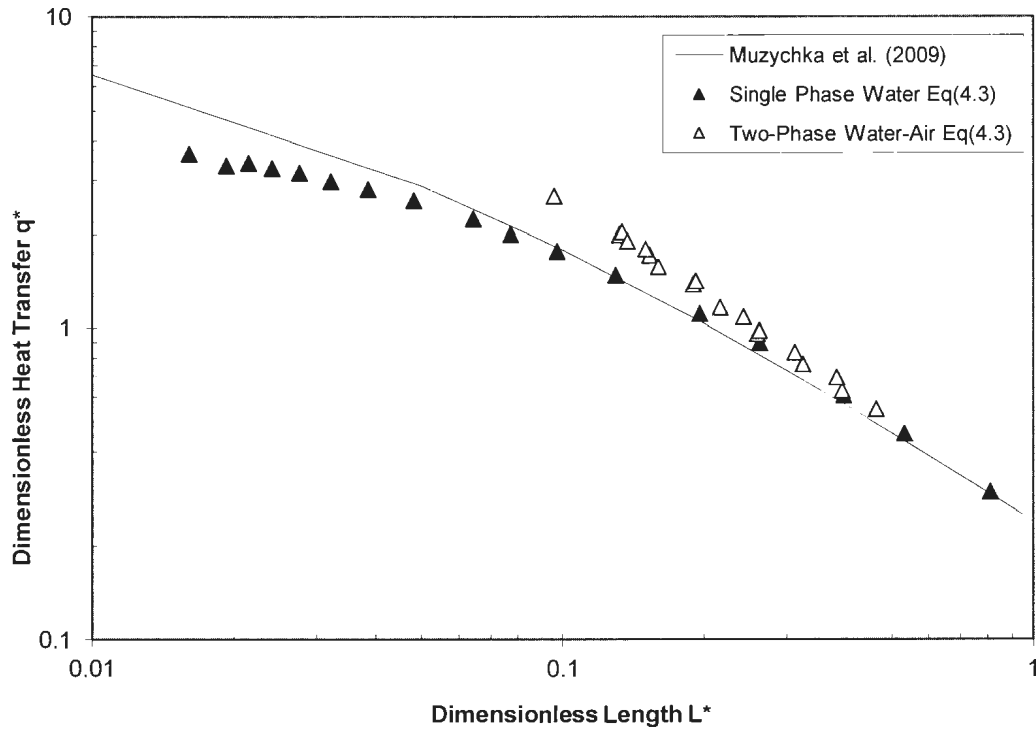


Figure 4.13 – Comparison of Single and Two-Phase Flow in the Square Sink.

Table 4.2

Comparison of Single and Two-Phase Flow

Sink	Comparison	Average Enhancement	
		Eq(4.3)	Eq(4.5)
Square Sink	Single Phase Water & Two-Phase Water-Air (Long Slugs)	+ 23%	+ 25%
	Single Phase Oil & Two-Phase Oil-Air (Long Slugs)	+ 6%	- 4%
	Single Phase Water & Two-Phase Water-Air (Short Slugs)	+ 40%	+ 39%
Spiral Sink	Single Phase Water & Two-Phase Water-Air (Forwards)	+ 12%	+ 16%
	Single Phase Water & Two-Phase Water-Air (Backwards)	+ 12%	+ 16%

Examination of Table 4.2 leads to several interesting conclusions. First, regardless of how the data is reduced (either by Eq. (4.3) or Eq. (4.5)) the Square Sink shows greater improvement in dimensionless heat transfer when segmenting the flow of water. The oil results however do not show significant improvement when segmenting the oil in the Square Sink and furthermore when the data reduction is conducted using Eq. (4.5) for bulk heat transfer the segmented oil-air degrades the average dimensionless heat transfer by 4% when compared to single phase oil. Additionally, segmenting the flow in the Spiral Sink leads to enhancement in dimensionless heat transfer, but the enhancement is not near as high as seen in the Square Sink. Again this must be the result of differences in geometry between the Square Sink and the Spiral Sink. It is theorized that perhaps the Square Sink having many 90° bends is affecting or disturbing the growth of the thermal boundary layer whereas the Spiral Sink smoothly transitions and perhaps does not affect the thermal boundary layer development. As stated previously, the true levels of dimensionless heat transfer enhancement lie somewhere between the average values predicted using Eq. (4.3) and Eq. (4.5) for segmented flow. If the mean average value is taken from the tabulated values in Table 4.2. then the average dimensionless heat transfer enhancement in the Square Sink over the entire range of dimensionless length is 24% for water with long slugs, 39.5% for water with short slugs, and 1% for oil with long slugs. Similarly the mean average dimensionless heat transfer enhancement in the Spiral Sink over the entire range of dimensionless length is shown to be 14% for water with short slugs in both the forward and backward directions. Note this does not mean the forward and backward flow directions have the same thermal performance, it simply means when comparing single phase to two-phase segmented flow in one direction, the increase in dimensionless heat transfer through segmentation is the same for that direction as when comparing the increase in the opposite direction. Again, this further shows that segmentation leads to an increase in dimensionless heat transfer and that shorter slugs show increased levels of enhancement.

### 4.3.7 Effect of Void Fraction

The effect of void fraction on dimensionless heat transfer enhancement during segmented flow will be discussed in this section. To analyze the effect of void fraction several flow rates having the same void fraction but different combinations of flow will be examined. A plot of dimensionless heat transfer versus liquid Reynolds number is constructed and for each value of void fraction the data from the corresponding flow combinations will be plotted. Analysis of the experimental results from two-phase segmented flow of water-air with long slug lengths in the Square Sink will be analyzed. Examination of the void fractions and flow rates indicate two void fraction values repeated for several combinations of flow, these values were  $\alpha_g = 66\%$  and  $\alpha_g = 50\%$ . The data from the flow combinations at these values of void fraction was used in construction of the plot of  $q^*$  vs.  $Re$  and is shown in Figure 4.14. The single phase data obtained for the Square Sink is also included as a reference line.

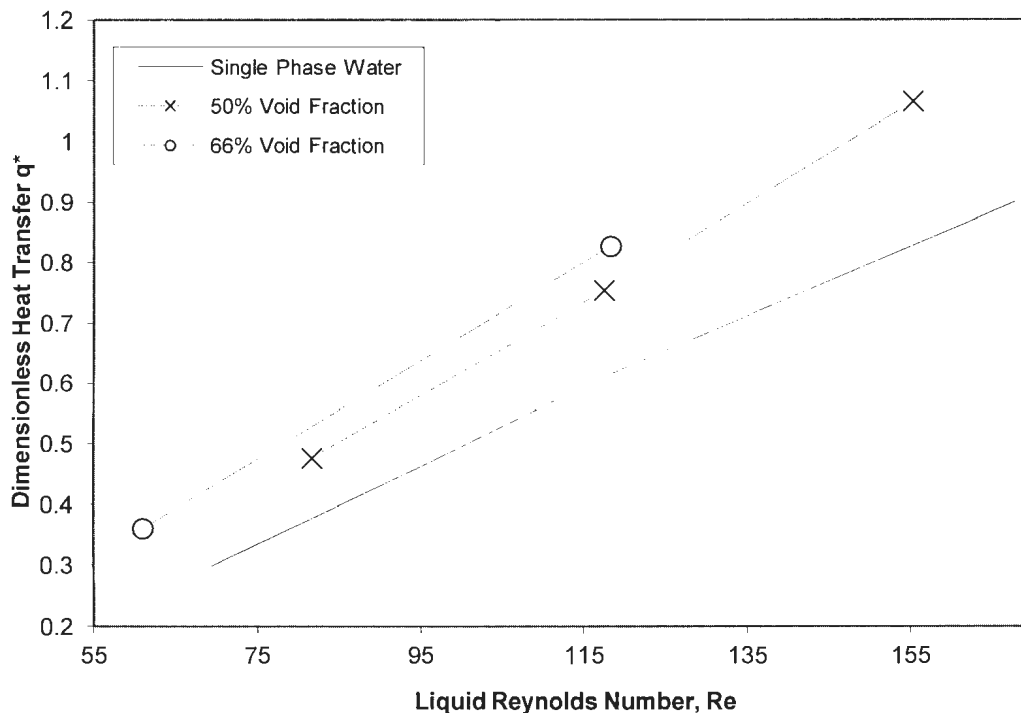
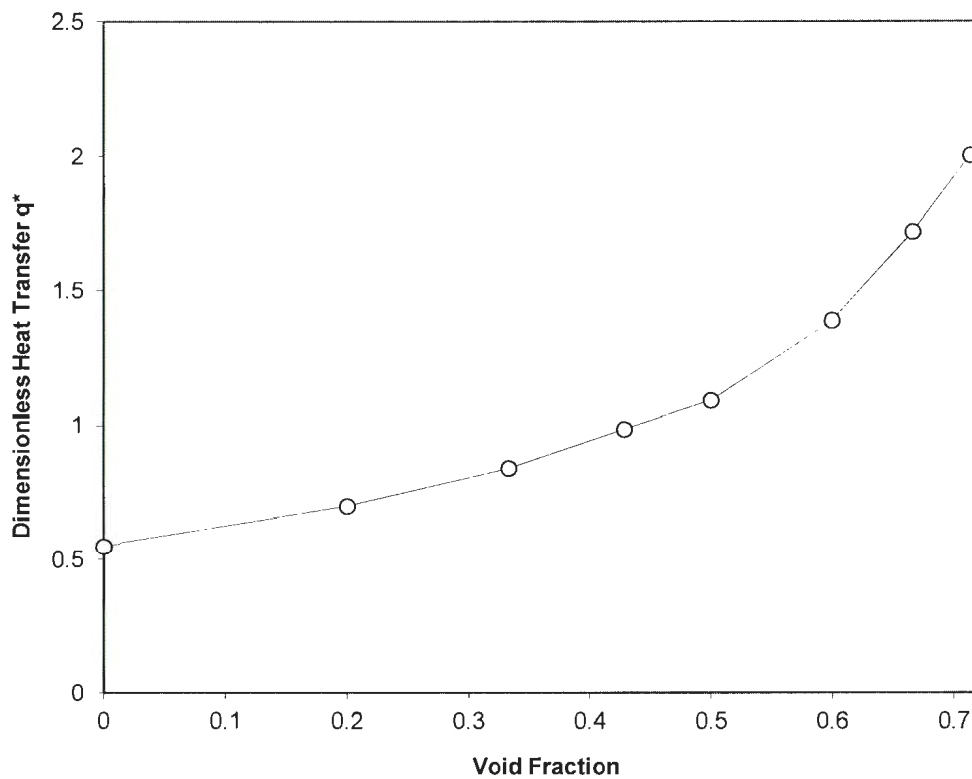


Figure 4.14 – Effect of Void Fraction on Dimensionless Heat Transfer in Square Sink.

From Figure 4.14 it is clearly shown that the dimensionless heat transfer is significantly improved by increasing the void fraction. With increased void fraction, the liquid slug length is decreased, resulting in a higher internal circulation speed. This would account for increased dimensionless heat transfer results obtained as the void fraction was increased. By considering a given flow rate of liquid phase and varying the gas flow rate (thus varying the void fraction) another plot of dimensionless heat transfer versus void fraction can be constructed. After reviewing the experimental data, the liquid flow rate with the most variation in gas flow rate occurred at 4.0 ml/min of the liquid phase during the two-phase segmented flow of water-air in the Square Sink using short slug lengths. This data was used to plot  $q^*$  vs.  $\alpha_g$  and is shown in Figure 4.15.



*Figure 4.15 – Effect of Void Fraction on a Constant Liquid Flow Rate in Square Sink.*

It can be concluded from Figure 4.15 that void fraction is a controlling factor in the dimensionless heat transfer due to segmented flow. This is ultimately due to the void

fraction controlling the liquid slug length and as shown previously (Section 4.3.4) a decrease in liquid slug length leads to an increase in enhancement of dimensionless heat transfer. This agrees well with published literature where the void fraction and slug length were studied. Such studies include the work of Horvath et al. (1973), Vrentas et al. (1978), and Fries et al. (2008). Detailed plots of Figures 4.14 and 4.15 can be found in Appendix B.

#### 4.3.8 Effect of Liquid Film Thickness

The liquid film thickness surrounding the gas phase in two-phase segmented flow will be discussed in this section. It is important to compare the liquid film thickness to the thermal boundary layer thickness, especially for high Prandtl number fluids such as oil. If the thermal boundary layer is significantly smaller than the liquid film thickness, then an enhancement in dimensionless heat transfer may not occur due to the thermal boundary layer not penetrating into the circulations present in liquid slugs.

**Table 4.3**  
**Liquid Film Thickness and Thermal Boundary Layer Thickness**  
**for Oil-Air Segmented Flow in Square Sink.**

Flow Rates $Q_{oil} - Q_{air}$ (ml/min)	Capillary Number Ca	Film Thickness (mm)	Thermal Boundary Layer Thickness (mm)
3.0 - 0.5	0.09	0.091	0.369
3.0 - 1.0	0.11	0.097	0.350
3.0 - 2.0	0.14	0.107	0.320
3.0 - 3.0	0.17	0.113	0.302
3.0 - 4.0	0.14	0.108	0.317
4.0 - 0.5	0.12	0.101	0.339
4.0 - 1.0	0.13	0.105	0.325
4.0 - 2.0	0.16	0.113	0.303
4.0 - 3.0	0.20	0.121	0.283
4.0 - 4.0	0.23	0.126	0.271

This analysis requires the calculation of Capillary number given by Eq. (4.16), liquid film thickness given by Eq. (4.15) and thermal boundary layer thickness given by Eq. (4.18) for each steady state set of experimental data. Then the comparison of thermal boundary layer and liquid film can be made. The experimental data from the two-phase segmented flow of oil-air and water-air (long slugs) in the Square Sink will be examined to address this concern. The results for oil-air segmented flow are shown in Table 4.3 and the results for water-air segmented flow are shown in Table 4.4.

**Table 4.4**  
**Liquid Film Thickness and Thermal Boundary Layer Thickness**  
**for Water-Air Segmented Flow in Square Sink.**

<b>Flow Rates</b> <b><math>Q_{\text{water}} - Q_{\text{air}}</math></b> <b>(ml/min)</b>	<b>Capillary</b> <b>Number</b> <b>Ca</b>	<b>Film</b> <b>Thickness</b> <b>(mm)</b>	<b>Thermal Boundary</b> <b>Layer Thickness</b> <b>(mm)</b>
3.0 - 1.0	0.0009	0.007	0.499
3.0 - 2.0	0.0010	0.008	0.472
3.0 - 3.0	0.0012	0.008	0.443
3.0 - 4.0	0.0015	0.009	0.411
3.0 - 6.0	0.0017	0.010	0.387
4.0 - 1.0	0.0010	0.007	0.468
4.0 - 2.0	0.0012	0.008	0.437
4.0 - 3.0	0.0015	0.009	0.413
4.0 - 4.0	0.0016	0.010	0.402
4.0 - 6.0	0.0021	0.012	0.370
4.0 - 8.0	0.0025	0.013	0.345
4.0 - 10.0	0.0029	0.015	0.328
5.0 - 5.0	0.0022	0.012	0.372
5.0 - 8.0	0.0028	0.014	0.343
5.0 - 10.0	0.0031	0.015	0.330
6.0 - 6.0	0.0026	0.013	0.350
6.0 - 8.0	0.0030	0.015	0.333
10.0 - 10.0	0.0044	0.019	0.295

The reduced experimental data appearing in Table 4.3 and Table 4.4 show that over the entire range of each experiment, the liquid film thickness is smaller than the thermal boundary layer thickness, therefore the film and circulations in liquid slugs are playing a role in the enhancement of the dimensionless heat transfer. Originally it was thought that the poor performance of oil may be due to the liquid film thickness being much larger than the thermal boundary layer thickness, but this is indeed not the case. In fact the thermal boundary layer thickness isn't far off that of water for the same combinations of liquid-gas flow rate in a segmented flow. If the flow rate of 3.0 ml/min liquid and 3.0 ml/min gas is examined for each segmented flow case in Tables 4.3 and 4.4, the thermal boundary layer thickness of oil is 0.302 mm and of water is 0.443 mm. Therefore the poor performance of oil is due to properties other than large liquid film thickness.

#### **4.3.9 Comparison of the Square Sink and Spiral Sink**

This section will detail the comparison between heat sink efficiencies by comparing the dimensionless heat transfer with the pressure drop for each heat sink. At this point it would seem that the Square Sink is out-performing the Spiral Sink in terms of thermal efficiency, but to conclude that the Square Sink is overall more efficient than the Spiral Sink or vice versa the pressure drop (power requirements) must also be considered when comparing the thermal performances. To conduct this analysis a normalized pressure will be defined by Eq. (4.20):

$$\Delta p^* = \frac{dp}{dp_{\max}} \quad (4.20)$$

By plotting  $q^*$  vs.  $\Delta p^*$  for the Square Sink and Spiral Sink (forwards and backwards) then the system that is overall more efficient can be determined. For the comparison data from the two-phase segmented flow of water-air in both Square and Spiral Sinks (using Short Slugs) will be used. The plot of  $q^*$  vs.  $\Delta p^*$  is shown in Figure 4.16.

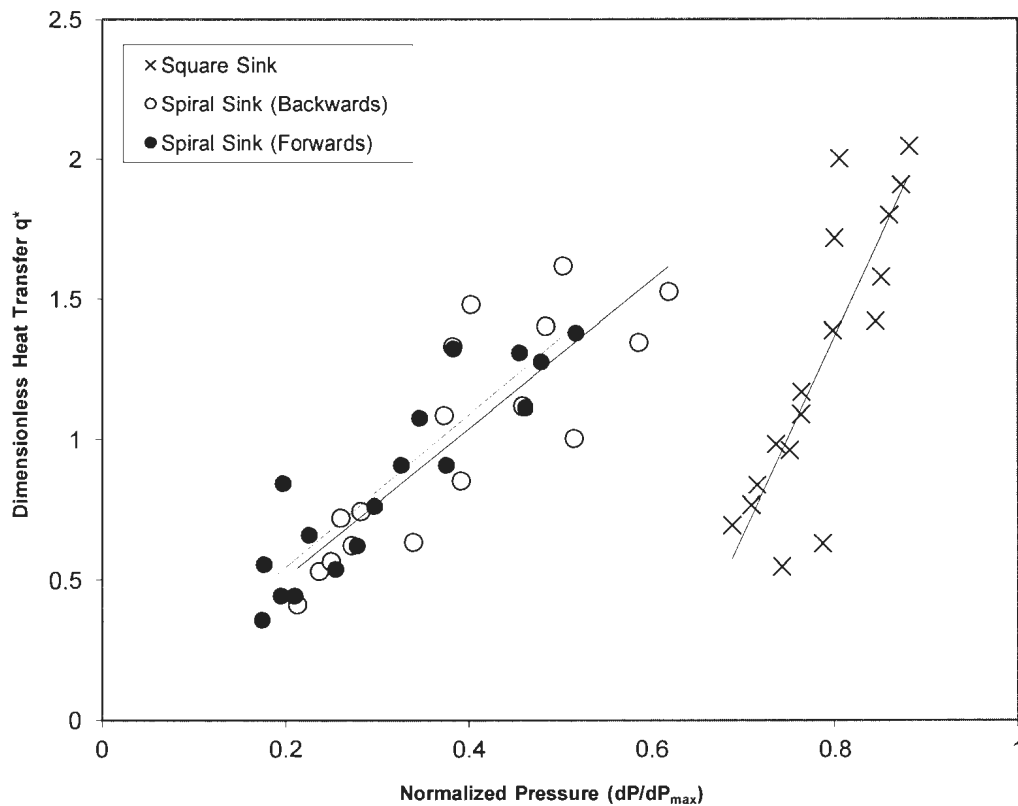


Figure 4.16 – Efficiency of Square Sink vs. Spiral Sink.

In Figure 4.16 three sets of experimental data are presented and trend lines have been added to each data set. The upper trend line passing through the Spiral Sink data belongs to the forward tests while the lower trend line belongs to the backward tests. From Figure 4.16 several conclusions can be drawn, firstly the Spiral Sink in forward mode operates with higher overall efficiency than in backward mode. This confirms the initial belief that the Spiral Sink would be more efficient in forward mode with the cold fluid entering the middle inlet where the heat sink was hottest. Secondly it is shown that for either direction the Spiral Sink is operating in, it is more efficient than the Square Sink, for lower normalized pressures the Spiral Sink gives higher dimensionless heat transfer values.

This higher efficiency is obvious when the normalized pressure value of 0.7 is examined, the Square Sink has a dimensionless heat transfer value of 0.5 while the Spiral Sink has a dimensionless heat transfer value closer to 1.5. Therefore, while all experimental data based on thermal performance pointed in the direction that the Square Sink was better, once power requirements such as pressure were considered it turns out that the Spiral Sink run in forward mode is overall more efficient. A larger plot of Figure 4.16 is included in Appendix B.

#### **4.4 Summary**

In this chapter the reduction of experimental data into dimensionless groups was discussed and the experimental results for the Square Sink and Spiral Sink were presented. Results for the Square Sink on single phase water, single phase oil, two-phase water-air (long slugs), two-phase oil-air (long slugs) and two-phase water-air (short slugs) were presented. Then results for the Spiral Sink on single phase water and two-phase water-air (short slugs) in both flow directions through the spiral were presented. Following the presentation of experimental data, the effect of slug length and void fraction was discussed. Then issues with liquid film thickness and thermal boundary layer thickness were addressed followed by a comparison of the overall efficiencies of the Square Sink and Spiral Sink. The Spiral Sink was found to operate with the greater overall efficiency in forward mode once the pressure drop was considered.

## **Chapter – 5**

### **Conclusion and Recommendations**

#### **5.1 Conclusion of Present Study**

The present study examined the use of two-phase segmented flow as a working fluid in the cooling of two mini-channel heat sinks. An introduction to two-phase flow was presented with respect to flow patterns and flow maps followed by an introduction to two-phase segmented flow. The use of mini-channel and micro-channel devices was reviewed and applications were given. A literature review on two-phase segmented flow was then presented with respect to published literature spanning the last sixty years. The fabrication of two mini-channel heat sinks was detailed; these heat sinks were termed the Square Sink and Spiral Sink. The experimental objectives, apparatus, setup, and procedure then followed. Next an uncertainty analysis was conducted for the dimensionless groups used in the reduction of data. Finally the reduction of data was discussed and the experimental results were presented.

The results from single phase flow of fluids were compared to the two-phase segmented flow results. For the Square Sink the mean average improvement in dimensionless heat transfer when using two-phase segmented flow was reported as 24% for water-air with long slugs, 39.5% for water-air with short slugs, and 1% for oil-air with long slugs. For the Spiral Sink the mean average improvement in dimensionless heat transfer when using two-phase segmented flow was reported as 14% for water-air with short slugs in both the forward and backward flow directions. All experimental data was presented graphically as plots of  $q^*$  vs.  $L^*$  and are also found in Appendix B.

A discussion on the effect of slug length was presented and it was shown that shorter liquid slugs lead to higher dimensionless heat transfer values when compared to longer liquid slugs at equivalent flow rates. The effect of void fraction was discussed and it was shown that as the void fraction increased so did the dimensionless heat transfer due to the decrease in liquid slug length. Finally the Square Sink and the Spiral Sink were compared to determine which had the best overall efficiency. The normalized pressure drop was considered along with the dimensionless heat transfer results and it was found that the Spiral Sink run in the forwards flow direction had the best overall performance.

## 5.2 Recommendations for Future Work

This section will detail recommendations for future work with regards to using two-phase segmented flow as a working fluid in cooling mini-channel heat sinks. The ideas detailed here were inspired by literature review and experiences during the present study. These are meant to be suggestions on how the experiments performed may be made easier and how the analysis of data could differ.

The first recommendation would be the creation of a gas stabilizing entrance block for the gas phase used in the segmented flow. This idea was taken from a paper published by Fries et al. (2008). Essentially a series of meandering channels with small diameter are used to increase the pressure drop and create a stable gas injection into the T-junction where the segmented flow would mature. A simple sketch of such a device is shown in Figure 5.1.

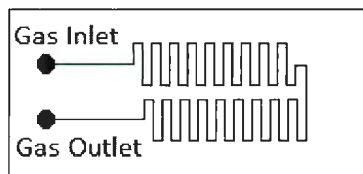


*Figure 5.1 – Conceptual Gas Stabilizing Block.*

The second recommendation would be to add a method for controlling the liquid slug length. Through the use of a micro electronic valve and a compressed gas tank, the valve could be set to different frequencies and the liquid slug length could be varied. Such micro electronic valves are available through CLIPPARD Inc. and are inexpensive. The valve would have to be controlled through the use of a programmable logic controller whereby the frequency of valve state could be programmed and adjusted.

The third recommendation would be the redesign of the heat sinks to include a bolt pattern around the outside edge of each base plate and cover plate. In the current study a clamp and glue were used to seal the base plate to the cover plate, this method was rather crude and several heating strips were destroyed in the process of tightening the clamp. With the addition of an outside bolt pattern, the need for clamping and glue would be eliminated and the ease of assembling and de-assembling each heat sink would be greatly improved.

The fourth recommendation would be to design a proper insulating compartment for the heat sinks. As shown in the experimental data from the current study, the results obtained by reducing the data based on bulk fluid temperature and losses to the environment differed (this is referring to the use of Eq. (4.3) and Eq. (4.5) from Chapter 4 in the reduction of data). For a completely insulated and controlled experiment the results from the two methods of data reduction should be very close together, thus a proper insulating compartment would reduce the error between both approaches.

The fifth recommendation would be a suggestion to get several heat sinks created so that glass slides could be glued over duplicate heat sinks for flow visualization experiments either with high-speed cameras or PIV analysis. This way the exact liquid slug lengths occurring during experiments could be deduced from the images rather than by the ratio of cross-sectional areas used in the current study.

The sixth recommendation would be to design the new heat sinks with the liquid and gas ports directly on the sinks themselves. This would ensure that segmented flows would develop directly inside the heat sink rather than externally. In the present study, the two-phase flow rates examined were picked because stable segmented flows that did not break up occurred over the range used. However, several other flow rates leading to excellent segmented flows could not be used because the slug trains would break up when passing through thermocouple and pressure junctions. If the segmented flow was created directly on the heat sink, this issue would be solved. Additionally, by pressure fitting a syringe needle into the sink itself very small segmented flows could be created with liquid slug lengths close to 2 mm long.

The seventh recommendation would be to measure the temperature of the segmented flow at the outlet of the heat sink by some means other than a thermocouple junction. For the segmented flow, the liquid slug passes over the thermocouple increasing the temperature while the gas slug passes over the thermocouple decreasing the temperature and therefore producing an overall average reading. This was ultimately the reason why the data was reduced two different ways in Chapter 4. A better way to measure the liquid temperature would be to somehow separate the two-phases quickly at the outlet and get a measurement from the liquid phase by itself. A small gas-liquid separator could be designed and put into place at the outlet of the heat sink and then the liquid phase alone could run through a thermocouple junction giving the temperature measurement desired.

## References

- Awad, M.M., and Muzychka, Y.S., "Bounds on Two Phase Frictional Pressure Gradient in Minichannels and Microchannels", *Heat Transfer Engineering*, Vol. 28, pp. 720-729, 2007.
- Bahrami, M., Yovanovich, M. M., Culham, J. R., "Pressure Drop of Fully-Developed, Laminar Flow in Microchannels of Arbitrary Cross-Section", *Transactions of the ASME*, Vol. 128, pp. 1036-1044, 2006.
- Bejan, A., "Convection Heat Transfer", Wiley, 2005
- Bretherton, F., "The Motion of Long Bubbles in Tubes", *Journal of Fluid Mechanics*, Vol. 10, pp. 166-188, 1961.
- Cavallini, A., Del Col, D., Doretti, L., Matkovic, M., Rossetto, L., and Zilio, C., "Two-Phase Frictional Pressure Gradient of R236ea, R134a and R410A inside Multiport Minichannels", *Experimental Thermal and Fluid Science*, Vol. 29, no. 7, pp. 861-870, 2005.
- Chen, W.L., Twu, M.C., and Pan, C., "Gas-Liquid Two-Phase Flow in Microchannels", *Int. J. Multiphase Flow*, Vol. 28, pp. 1235-1247, 2002.
- Chisholm, D., "A Theoretical Basis for the Lockhart-Martinelli Correlation for Two Phase Flow", *International Journal of Heat and Mass Transfer*, Vol. 10, pp. 1767-1778, 1967.
- Chung, P.M.Y., and Kawaji, M., "The Effect of Channel Diameter on Adiabatic Two-Phase Flow Characteristics in Microchannels", *Int. J. Multiphase Flow*, Vol. 30, no. 7-8, pp. 735-761, 2004.

Churchill, S.W. and Usagi, R., "A General Expression for the Correlation of Rates of Transfer and Other Phenomena", *American Institute of Chemical Engineers*, Vol. 18, pp. 1121-1128, 1972.

Field, B.S., and Hrnjak, P., "Adiabatic Two-Phase Pressure Drop of Refrigerants in Small Channels", *Heat Transfer Engineering*, Vol. 28, no. 8-9, pp. 704-712, 2007.

Fries, D., Trachsel, F., von Rohr, P.R., "Segmented Gas-Liquid Flow Characterization in Rectangular Channels", *International Journal of Multiphase Flow*, Vol. 34, pp. 1108-1118, 2008.

Garimella, V., Poh-Seng, L., "Thermally Developing Flow and Heat Transfer in Rectangular Microchannels of Different Aspect Ratios", *International Journal of Heat and Mass Transfer*, Vol. 49, pp. 3060-3067, 2006.

Hassan, I., "Thermal-Fluid MEMS Devices: A Decade of Progress and Challenges Ahead", *Journal of Heat Transfer*, Vol. 128, pp. 1221-1233, 2008

Hassan, I., Vaillancourt, M., Pehlivan, K., "Two-Phase Flow Regime Transition in Microchannels: a Comparative Experimental Study", *Microscale Thermophysical Engineering*, Vol. 9, pp. 165-182, 2005.

Horvath, C., Solomon, B.A., Engasser, J.M., "Measurement of Radial Transport in Slug Flow Using Enzyme Tubes", *Industrial and Engineering Chemistry, Fundamentals*, Vol. 12, no. 4, pp. 431-439, 1973.

Hughmark, G.A., "Holdup and Heat Transfer in Horizontal Slug Gas-Liquid Flow", *Chemical Engineering Science*, Vol. 20, pp. 1007-1010, 1965.

Kawaji, M., and Chung, P. M. Y., "Adiabatic Gas-Liquid Flow in Microchannels", *Microscale Thermophysical Engineering*, Vol. 8, pp. 239-257, 2004.

Kawaji, M., Mori, K., and Bolintineanu, D., "The Effects of Inlet Geometry on Gas-Liquid Two-Phase Flow in Microchannels", *Proc. ICMM2005, 3rd International Conference on Microchannels and Minichannels*, Toronto, Ontario, ICMM2005-75087, 2005.

Kline, S.J., and F. A. McClintock, "Describing Uncertainties in Single-Sample Experiments", *Mech. Eng.*, p. 3, January 1953.

Kolb, W.B., and Cerro, R.L., "Coating the Inside of a Capillary of Square Cross Section", *Chem. Eng. Science*, Vol. 46, pp. 2181-2195, 1991.

Kreutzer, M.T., Kapteijn, F., Moulijn, J.A., Kleijn, C.R., Heiszwolf, J.J., "Inertial and Interfacial Effects on Pressure Drop of Taylor Flow in Capillaries", *AIChE Journal*, Vol. 51, no. 9, pp. 2428-2440, 2005.

Lakehal, D., Larrignon, G., and Narayanan, C., "Computational Heat Transfer and Two Phase Flow Topology in Miniature Tubes", *Microfluidics and Nanofluidics*, Vol. 4, no. 4, pp. 261-271, 2006.

Narayanan, C., and Lakehal, D., "Two-Phase Convective Heat Transfer in Miniature Pipes Under Normal and Microgravity Conditions", *Journal of Heat Transfer*, Vol. 130, pp. xx-xx, 2008.

Lee, H.J., and Lee, S.Y., "Pressure Drop Correlations for Two Phase Flow within Horizontal Rectangular Channels with Small Heights", *Int. J. Multiphase Flow*, Vol. 27, no. 5, pp. 783-796, 2001.

Lockhart, R.W. and Martinelli, R.C., "Proposed Correlation of Data for Isothermal Two Phase Flow, Two Component Flow in Pipes", *Chemical Engineering Progress*, Vol. 45, pp. 39-48, 1949.

Mishima, K.H.T., "Some Characteristics of Air-Water Two-Phase Flow in Small Diameter Vertical Tubes", *Int. J. Multiphase Flow*, Vol. 22, pp. 703-712, 1996.

Mohseni, K. and Baird, E.S., "Digitized Heat Transfer Using Electrowetting on Dielectric", *Nanoscale and Microscale Thermophysical Engineering*, Vol. 11, pp. 99-108, 2007.

Monde, M., and Mitsutake, Y., "Enhancement of Heat Transfer Due to Bubble Passing Through a Narrow Vertical Rectangular Channel", *Heat Mass Transfer*, Vol. 31, pp. 77-82, 1995.

Muzychka, Y.S. and Awad, M.M., "Two-Phase Flow Modelling in Microchannels and Minichannels", *ICNMM2008, Sixth International ASME Conference on Nanochannels, Microchannels, and Minichannels*, Darmstadt, Germany, June 23-25, ICNMM2008-62134, 2008

Muzychka, Y.S., Walsh, E., and Walsh, P., "Heat Transfer Enhancement Using Laminar Gas-Liquid Segmented Fluid Streams", *Proceedings of InterPack 2009*, San Francisco, July 19-23, 2009

Muzychka, Y.S. and Yovanovich, M.M., "Laminar Forced Convection Heat Transfer in the Combined Entry Region of Non-Circular Ducts", *Journal of Heat Transfer*, Vol. 126, pp. 54-62, 2004.

Ohtake, H., Koizumi, Y., and Takahashi, H., "Frictional Pressure Drops of Single-Phase and Gas-Liquid Two-Phase Flows in Circular and Rectangular Microchannels", *Proceedings of ICMM2005, 3rd International Conference on Microchannels and Minichannels*, ICMM2005-75147, Toronto, Ontario, 2005.

Oliver, D.R. and Wright, S.J., "Pressure Drop and Heat Transfer in Gas-Liquid Slug Flow in Horizontal Tubes", *British Chemical Engineering*, Vol. 9, pp. 590-596, 1964.

Oliver, D.R. and Young Hoon, A., "Two Phase Non-Newtonian Flow: Part 1 Pressure Drop and Holdup", *Transactions of the Institution of Chemical Engineers*, Vol. 46, pp. 106-115, 1968.

Oliver, D.R. and Young Hoon, A., "Two Phase Non-Newtonian Flow: Part 2 Heat Transfer", *Transactions of the Institution of Chemical Engineers*, Vol. 46, pp. 116-122, 1968.

Prothero, J. And Burton, A.C., "The Physics of Blood Flow in Capillaries: 1 The Nature of the Motion", *Biophysical Journal*, Vol. 1, pp. 565-579, 1961.

Przybylski, R., "Canola Oil: Physical and Chemical Properties", [www.canolacouncil.org/uploads/Chemical1-6.pdf](http://www.canolacouncil.org/uploads/Chemical1-6.pdf), pp. 1-6, 2000.

Taylor, G.I., "Deposition of a Viscous Fluid on the Wall of a Tube", *Journal of Fluid Mechanics*, Vol. 10, pp. 161-165, 1961.

Tran, T.N., Chyu, M.-C., Wambsganss, M.W., and France, D.M., "Two-Phase Pressure Drop of Refrigerants during Flow Boiling in Small Channels: An Experimental Investigation and Correlation Development", *Int. J. Multiphase Flow*, Vol. 26, no. 11, pp. 1739-1754, 2000.

Ua-Arayaporn, P., Fukagata, K., Kasagi, N., and Himeno, T., "Numerical Simulation of Gas-Liquid Two Phase Convective Heat Transfer in a Micro Tube", *ECI International Conference on Heat Transfer and Fluid Flow in Microscale*, Castelvecchio Pascoli, September 25-30, 2005.

Ungar, E.K., and Cornwell, J.D., "Two-Phase Pressure Drop of Ammonia in Small Diameter Horizontal Tubes", *17th AIAA Aerospace Ground Testing Conference*, AIAA 92-3891, Nashville, TN, 1992.

Vrentas, J.S., Duda, J.L., and Lehmkuhl, G.D., "Characteristics of Radial Transport in Solid-Liquid Slug Flow", *Industrial and Engineering Chemistry, Fundamentals*, Vol. 17, no. 1, pp. 39-45, 1978.

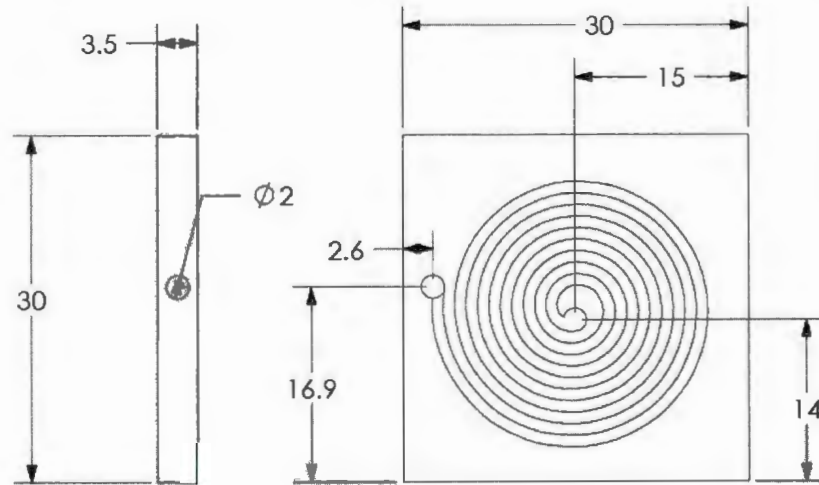
Walsh, P., Walsh, E., and Muzychka, Y.S., "Laminar Slug Flow – Heat Transfer Characteristics With A Constant Flux Boundary", *Proceedings of the ASME Summer Heat Transfer Conference*, San Francisco, July 19-23, 2009.

Wang, B. X., Peng, X. F., Peterson, G. P., Ma, H. B., "Experimental Investigation of Heat Transfer in Flat Plates with Rectangular Microchannels", *International Journal of Heat and Mass Transfer*, Vol. 38, no. 1, pp. 127-137, 1995.

Yu, Z., Hemminger, O., and Fan, L.S., "Experiment and Lattice Boltzmann Simulation of Two Phase Gas-Liquid Flows in Microchannels", *Chemical Engineering Science*, Vol. 62, pp. 7172-7183, 2007.

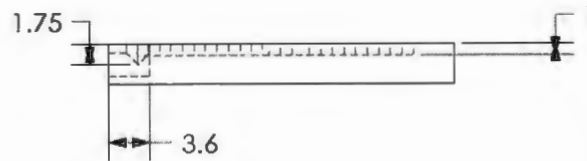
Zhang, L., Koo, J., Jiang, L., Asheghi, M., Goodson, K., Santiago, J., and Kenny, T. W., "Measurements and Modeling of Two-Phase Flow in Microchannels With Nearly Constant Heat Flux Boundary Conditions", *Journal of Microelectromechanical Systems*, Vol. 11, no. 1, pp. 12-19, 2002.

**Appendix A**  
**Heat Sink Technical Drawings**



Note:

- All cuts to be made in polished side
- Channel cut width = 1 mm
- Channel cut depth = 1 mm
- Inlet hole cut to 1.75 mm depth
- Design has only 1 inlet port
- Quantity: 1



Spiral Sink Base Plate



**PROPRIETARY AND CONFIDENTIAL**  
 THE INFORMATION CONTAINED  
 IN THIS DRAWING IS THE SOLE PROPERTY OF  
 MEMORIAL UNIVERSITY OF NEWFOUNDLAND  
 ANY REPRODUCTION IN PART OR AS A WHOLE  
 WITHOUT THE WRITTEN PERMISSION OF  
 MEMORIAL UNIVERSITY OF NEWFOUNDLAND  
 IS PROHIBITED.

UNLESS OTHERWISE SPECIFIED:

DIMENSIONS ARE IN MM  
 TOLERANCES:  
 FRACTIONAL N/A  
 ANGULAR: MACH  $\pm 0.1^\circ$  BEND  $\pm 1^\circ$   
 ONE PLACE DECIMAL  $\pm 0.1$   
 TWO PLACE DECIMAL  $\pm 0.01$

INTERPRET GEOMETRIC  
 TOLERANCING PER:

MATERIAL  
**Stainless Steel**

FINISH

NAME DATE

DRAWN BG Sep 09

CHECKED

ENG APPR.

MFG APPR.

Q.A.

COMMENTS:

TITLE:

**Spiral Pattern Rev 1**

SIZE DWG. NO.

**A 6**

REV

**A**



THIRD  
 ANGLE  
 PROJECTION

SCALE: 2:1 -

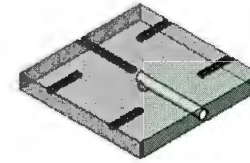
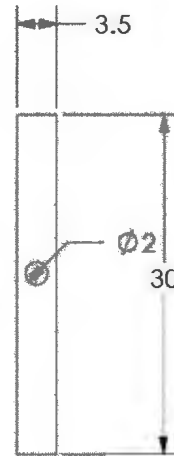
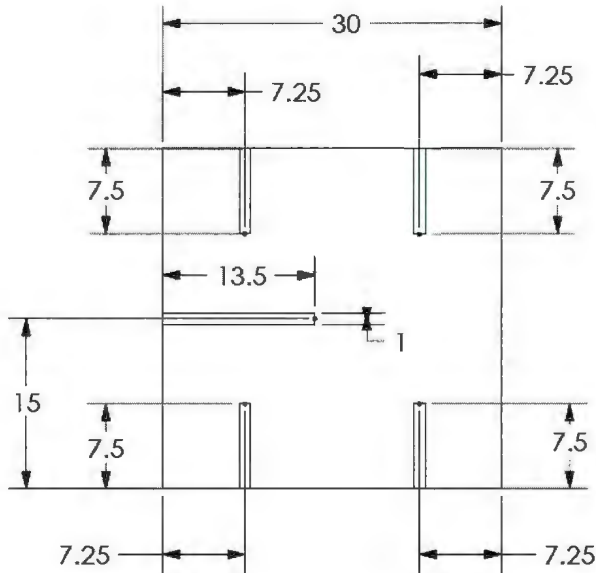
SHEET 1 OF 1

NEXT ASSY

USED ON

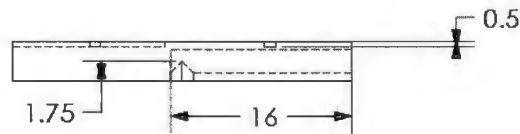
APPLICATION

DO NOT SCALE DRAWING



**Note:**

- All cuts to be made in **NON** - polished side
- Channel cut width = 1 mm
- Channel cut depth = 0.5 mm
- Inlet port cut 1.75 mm from **bottom**
- Quantity: 1



**PROPRIETARY AND CONFIDENTIAL**  
 THE INFORMATION CONTAINED  
 IN THIS DRAWING IS THE SOLE PROPERTY OF  
 MEMORIAL UNIVERSITY OF NEWFOUNDLAND.  
 ANY REPRODUCTION IN PART OR AS A WHOLE  
 WITHOUT THE WRITTEN PERMISSION OF  
 MEMORIAL UNIVERSITY OF NEWFOUNDLAND  
 IS PROHIBITED.

UNLESS OTHERWISE SPECIFIED:  
 DIMENSIONS ARE IN MM  
 TOLERANCES:  
 FRACTIONAL N/A  
 ANGULAR: MACH  $\pm 0.1^\circ$  BEND  $\pm 1^\circ$   
 ONE PLACE DECIMAL  $\pm 0.1$   
 TWO PLACE DECIMAL  $\pm 0.01$

INTERPRET GEOMETRIC  
 TOLERANCING PER:

MATERIAL  
**Stainless Steel**

FINISH

NEXT ASSY USED ON

APPLICATION

DO NOT SCALE DRAWING

NAME DATE  
 BG Sep 09

CHECKED  
 ENG APPR.  
 MFG APPR.

Q.A.  
 COMMENTS:

TITLE:

**Cover Rev 1**

SIZE DWG. NO.

**A 8**

REV

**A**

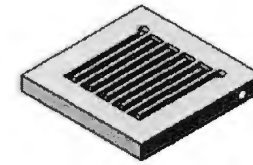
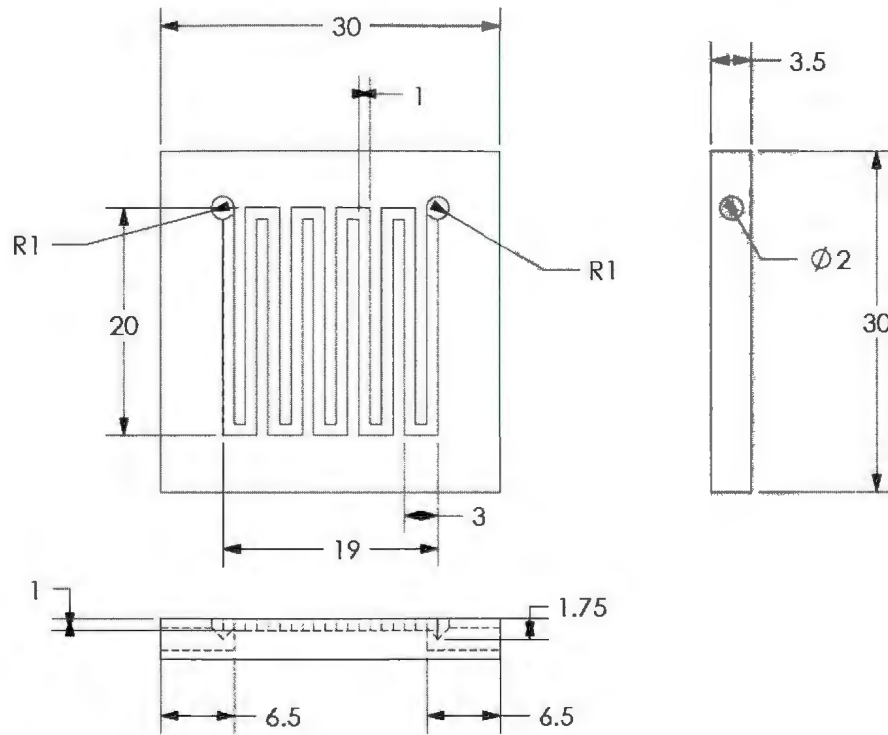


THIRD  
 ANGLE  
 PROJECTION

SCALE: 2:1 -

SHEET 1 OF 1

**Spiral Sink Cover Plate**



**Note:**

- All cuts to be made in polished side
- Channel cut width = 1 mm
- Channel cut depth = 1 mm
- Inlet channels cut to 1.75 mm depth
- Quantity: 1

**Square Sink Base Plate**



**PROPRIETARY AND CONFIDENTIAL**  
 THE INFORMATION CONTAINED  
 IN THIS DRAWING IS THE SOLE PROPERTY OF  
 MEMORIAL UNIVERSITY OF NEWFOUNDLAND.  
 ANY REPRODUCTION IN PART OR AS A WHOLE  
 WITHOUT THE WRITTEN PERMISSION OF  
 MEMORIAL UNIVERSITY OF NEWFOUNDLAND  
 IS PROHIBITED.

NEXT ASSY USED ON APPLICATION

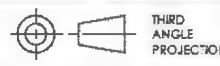
UNLESS OTHERWISE SPECIFIED:  
 DIMENSIONS ARE IN MM  
 TOLERANCES:  
 FRACTIONAL N/A  
 ANGULAR: MACH ±0.1° BEND ±1°  
 ONE PLACE DECIMAL ±0.1  
 TWO PLACE DECIMAL ±0.01

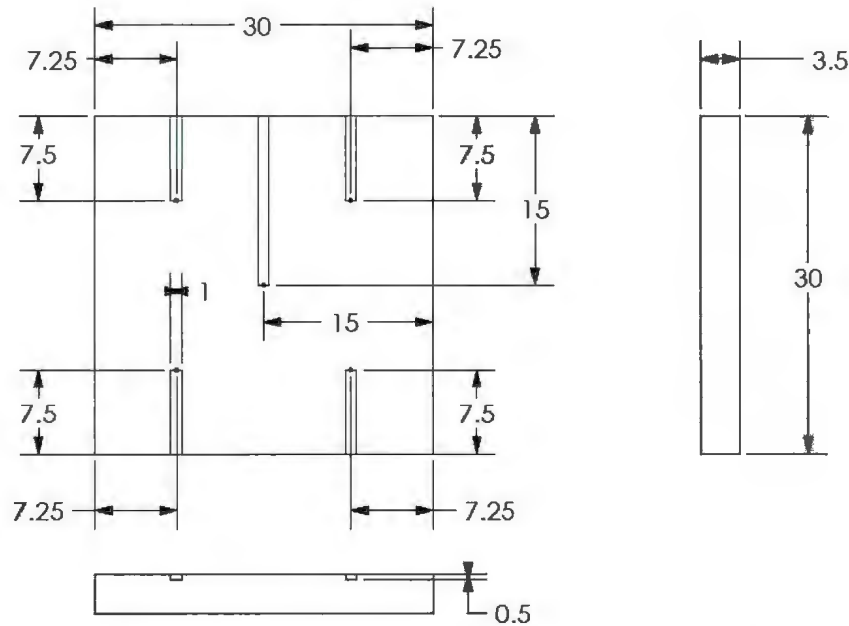
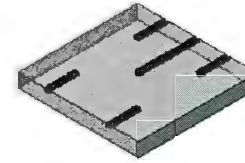
INTERPRET GEOMETRIC TOLERANCING PER:  
 MATERIAL: **Stainless Steel**  
 FINISH: DO NOT SCALE DRAWING

NAME DATE  
 DRAWN BG Sep 09  
 CHECKED  
 ENG APPR.  
 MFG APPR.  
 Q.A.  
 COMMENTS:

TITLE:  
**Square Pattern Rev 1**

SIZE DWG. NO. REV  
**A 2 A**  
 SCALE: 2:1 SHEET 1 OF 1





**Note:**

- All cuts to be made in **NON** - polished side
- Channel cut width = 1 mm
- Channel cut depth = 0.5 mm
- Quantity: 1

**Square Sink Cover Plate**

116



**PROPRIETARY AND CONFIDENTIAL**  
 THE INFORMATION CONTAINED  
 IN THIS DRAWING IS THE SOLE PROPERTY OF  
 MEMORIAL UNIVERSITY OF NEWFOUNDLAND.  
 ANY REPRODUCTION IN PART OR AS A WHOLE  
 WITHOUT THE WRITTEN PERMISSION OF  
 MEMORIAL UNIVERSITY OF NEWFOUNDLAND  
 IS PROHIBITED.

NEXT ASSY USED ON

APPLICATION

UNLESS OTHERWISE SPECIFIED:

DIMENSIONS ARE IN MM  
 TOLERANCES:  
 FRACTIONAL N/A  
 ANGULAR: MACH ±0.1° BEND ±1°  
 ONE PLACE DECIMAL ±0.1  
 TWO PLACE DECIMAL ±0.01

INTERPRET GEOMETRIC  
 TOLERANCING PER:

MATERIAL  
**Stainless Steel**

FINISH

DO NOT SCALE DRAWING

DRAWN

CHECKED

ENG APPR.

MFG APPR.

Q.A.

COMMENTS:

NAME DATE

BG Sep 09

TITLE:

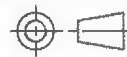
**Cover Rev 0**

SIZE DWG. NO.

**A 7**

REV

**A**



THIRD  
 ANGLE  
 PROJECTION

SCALE: 2:1 -

SHEET 1 OF 1

# **Appendix B**

## **Experimental Plots**

Figure 4.1 – Results for Single Phase Water in Square Sink.

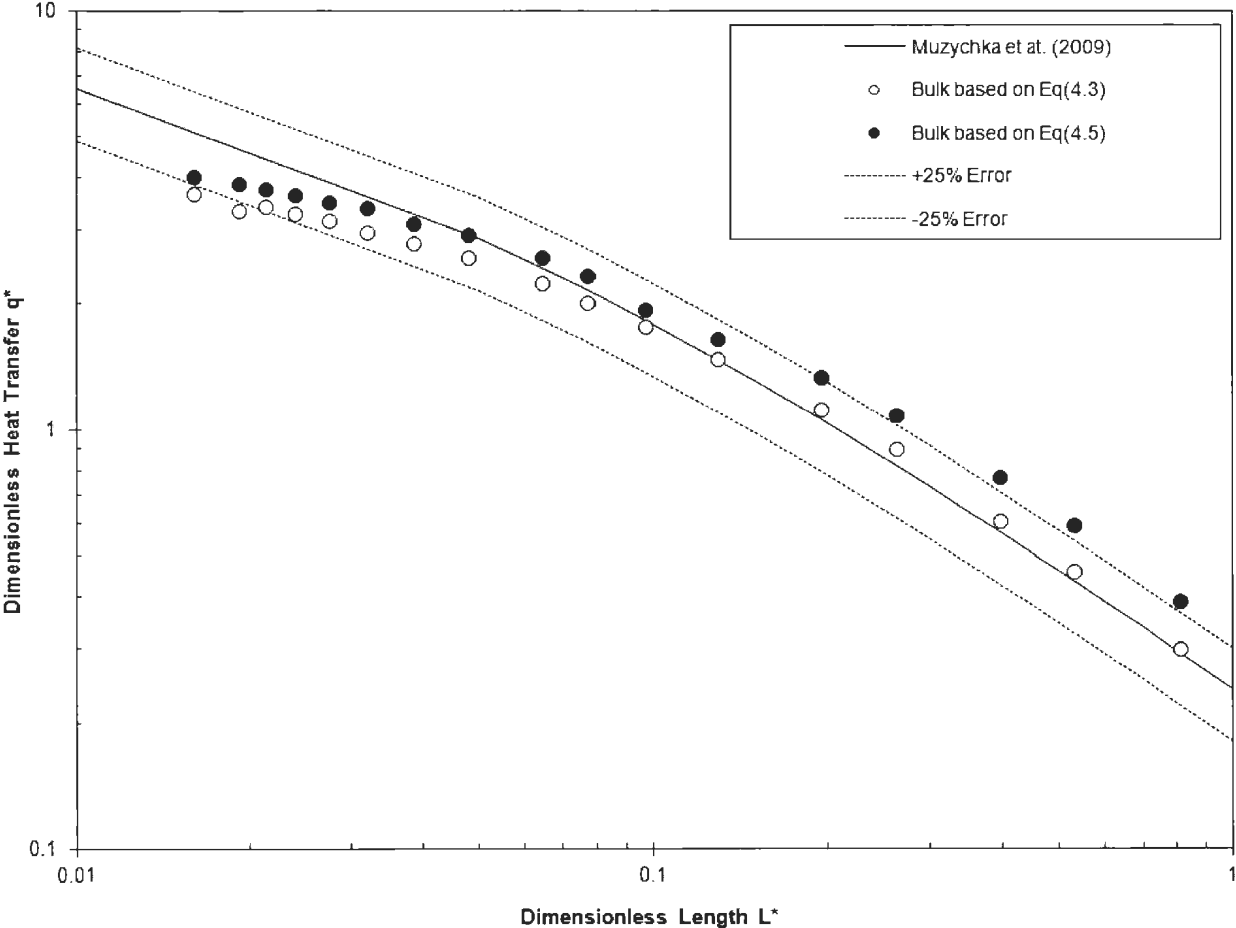


Figure 4.2 – Results for Two-Phase Water-Air (Long Slugs) in Square Sink.

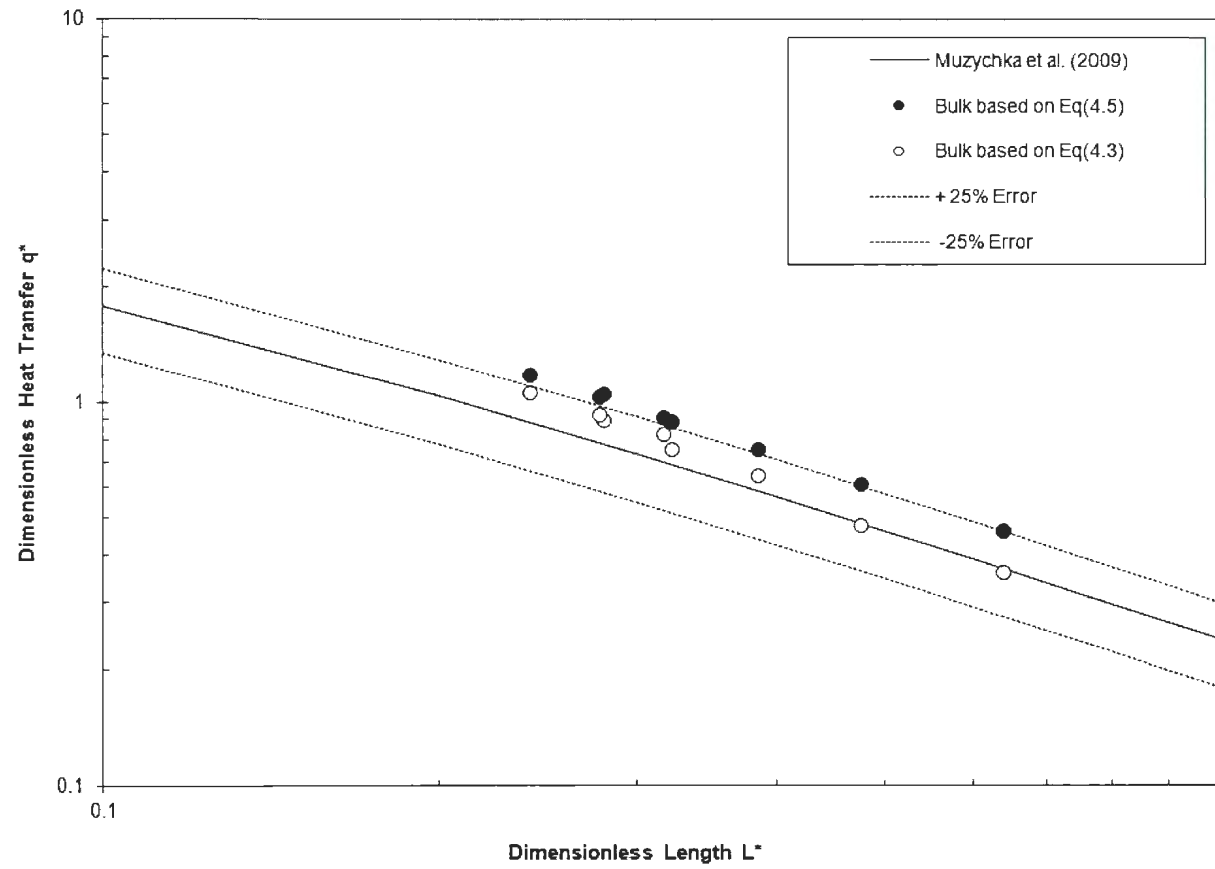


Figure 4.3 – Results for Single Phase Oil in Square Sink.

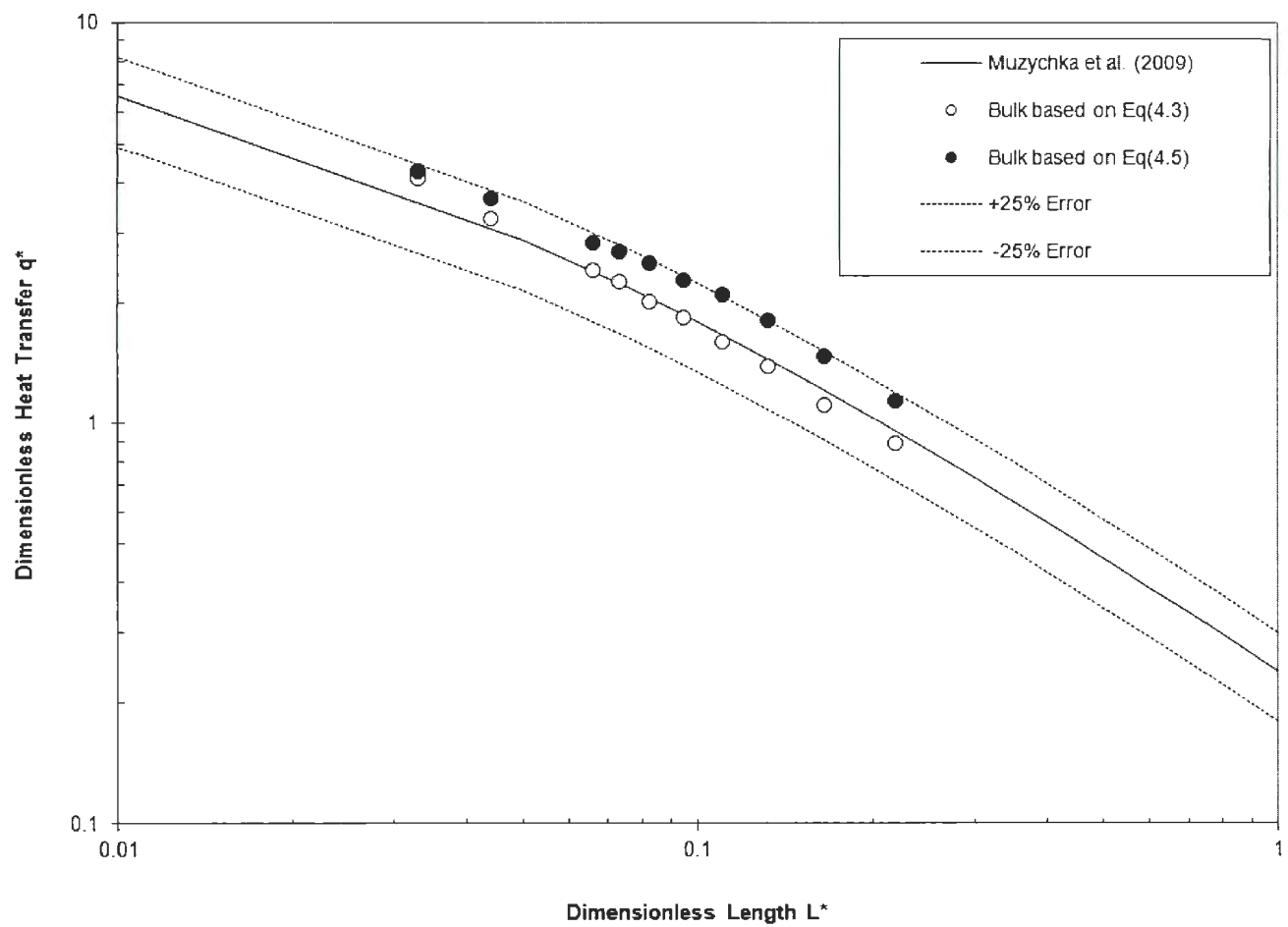


Figure 4.4 – Results for Two-Phase Oil-Air in Square Sink.

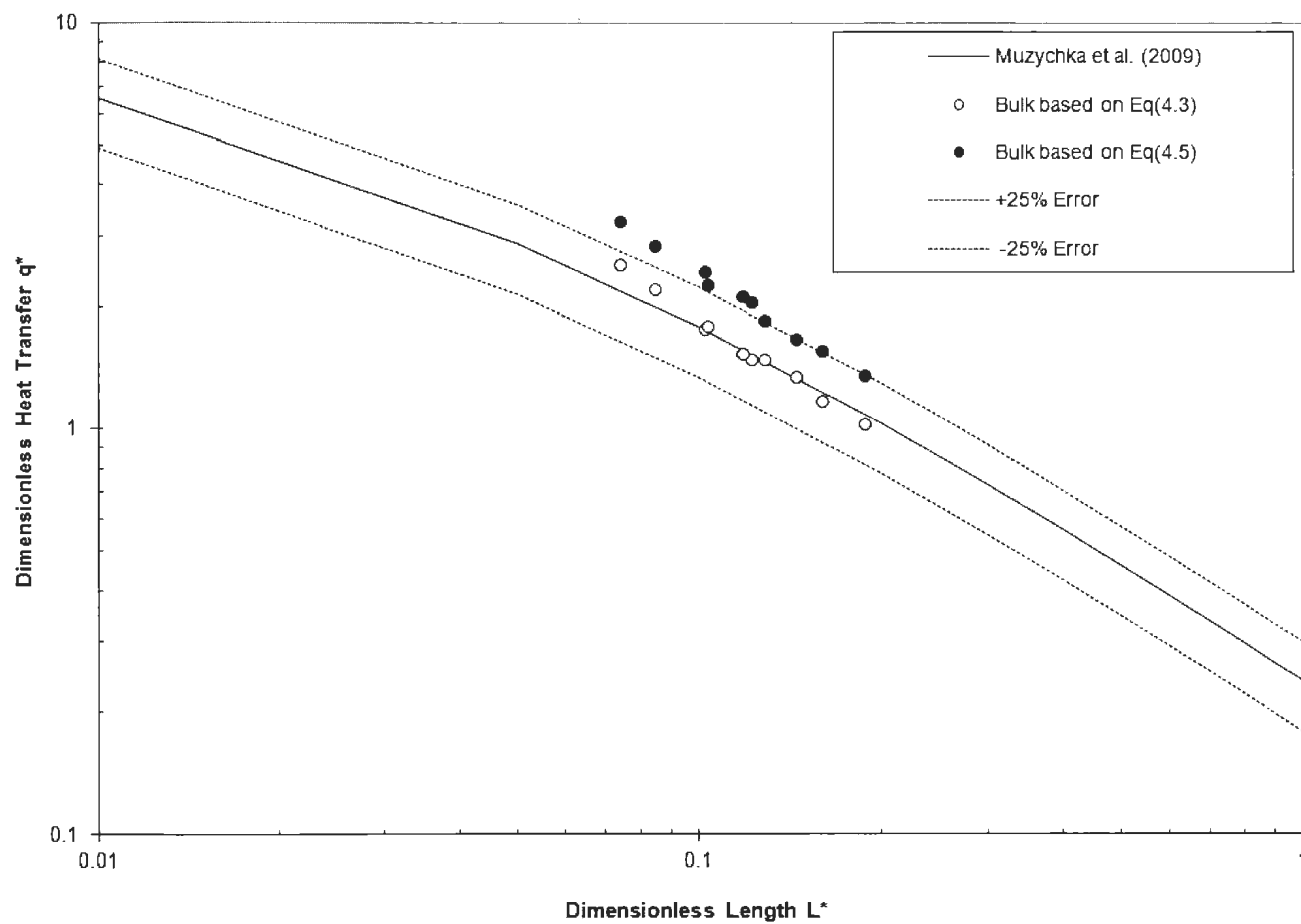


Figure 4.5 – Results for Two-Phase Water-Air (Short Slugs) in Square Sink.

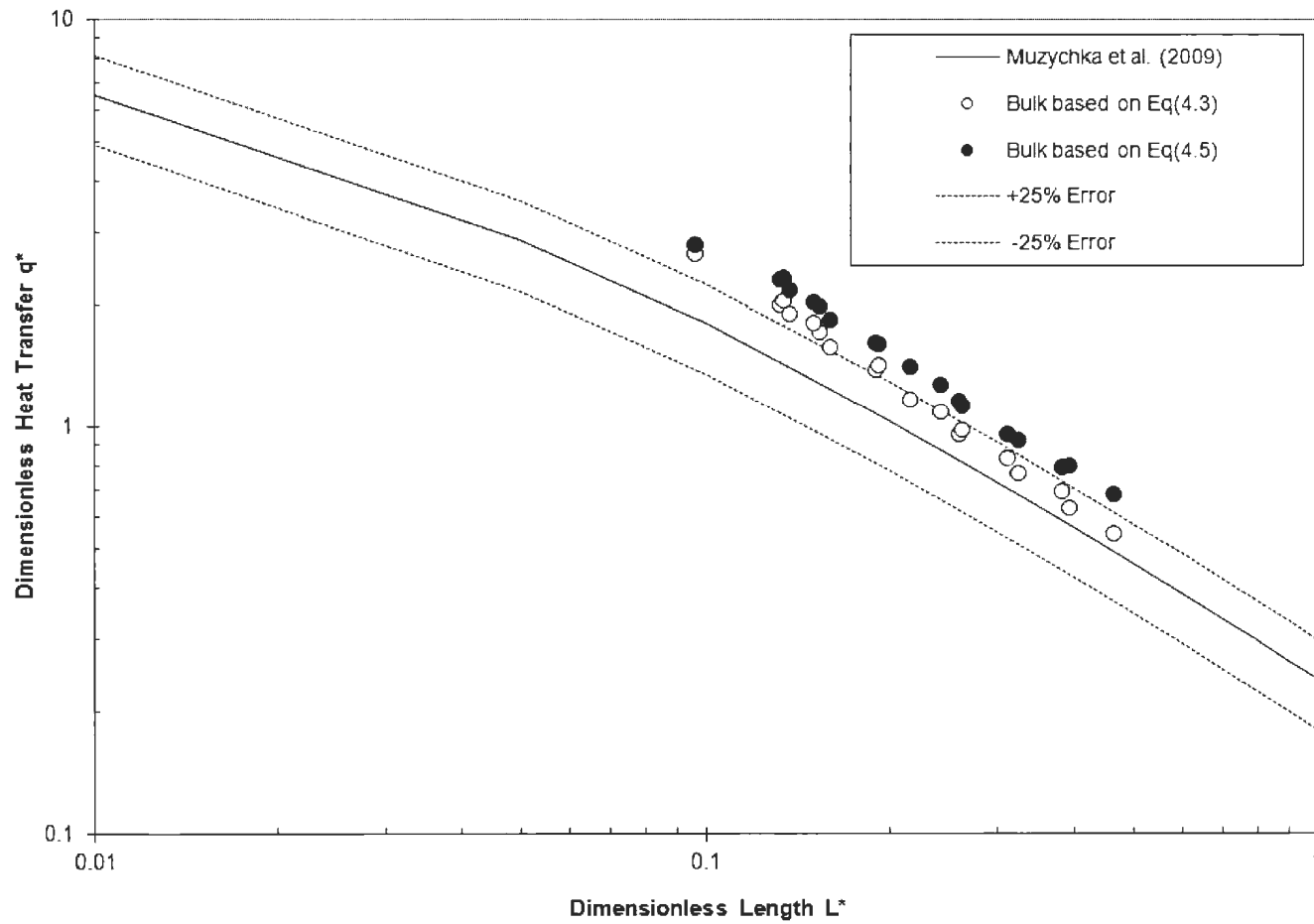


Figure 4.6 – Results for Single Phase Water in Spiral Sink (Forwards).

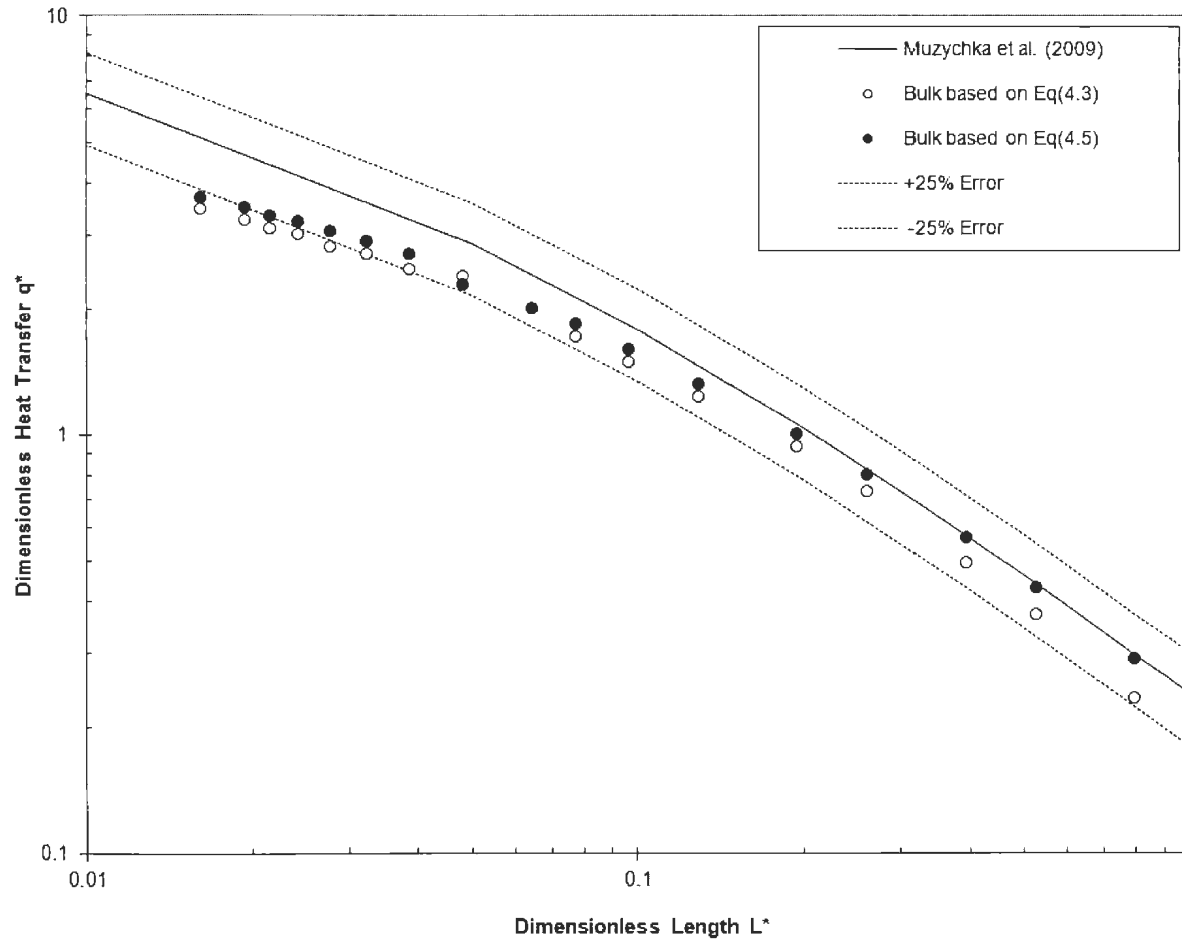


Figure 4.7 – Results for Single Phase Water in Spiral Sink (Backwards).

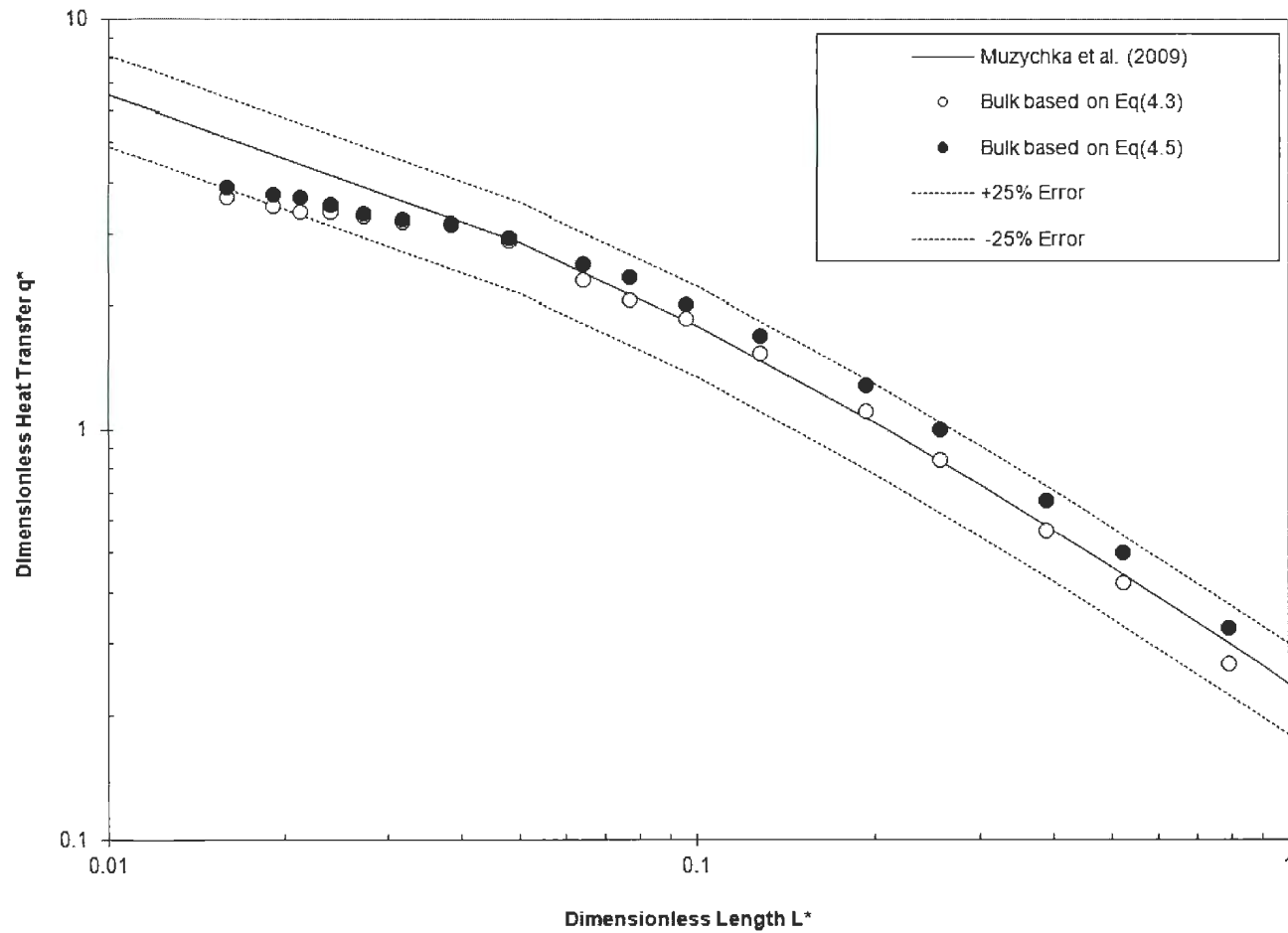


Figure 4.8 – Results for Two-Phase Water-Air in Spiral Sink (Forwards).

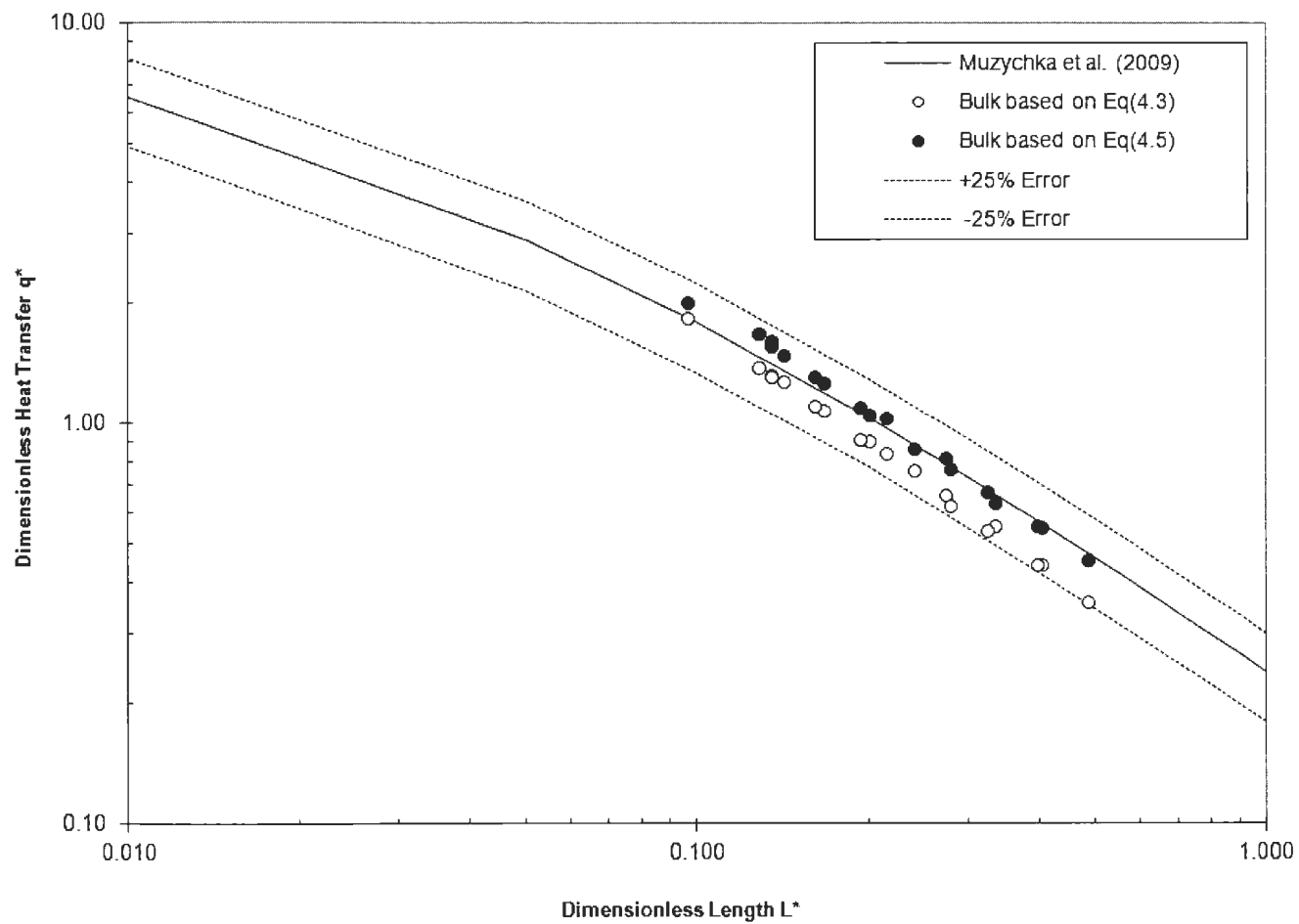




Figure 4.10 – Comparison of Long Slugs and Short Slugs in Square Sink using Two-Phase Water-Air Flow.

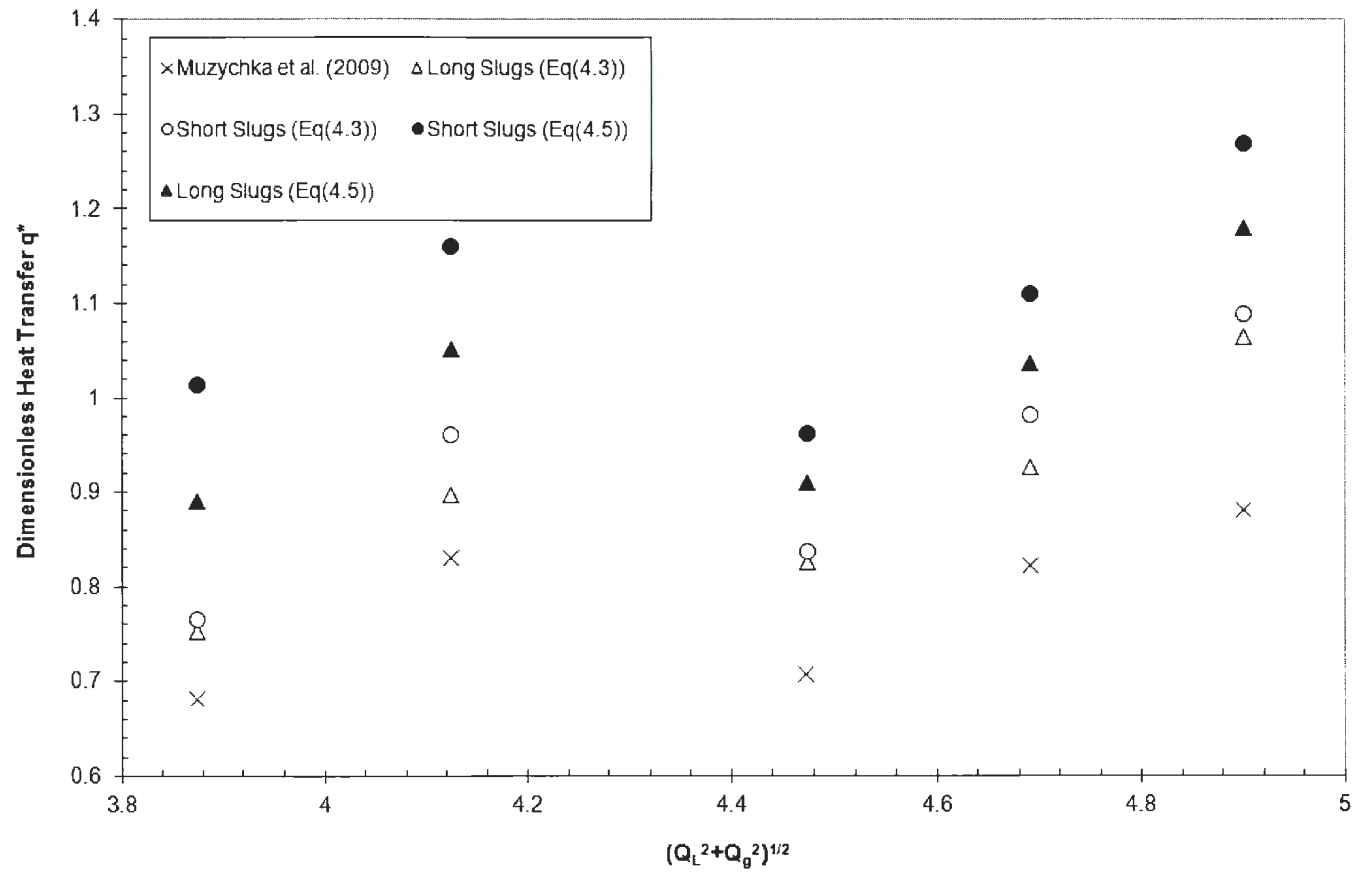


Figure 4.11 – Comparison of Flow Direction in Spiral Sink for Single Phase Flow.

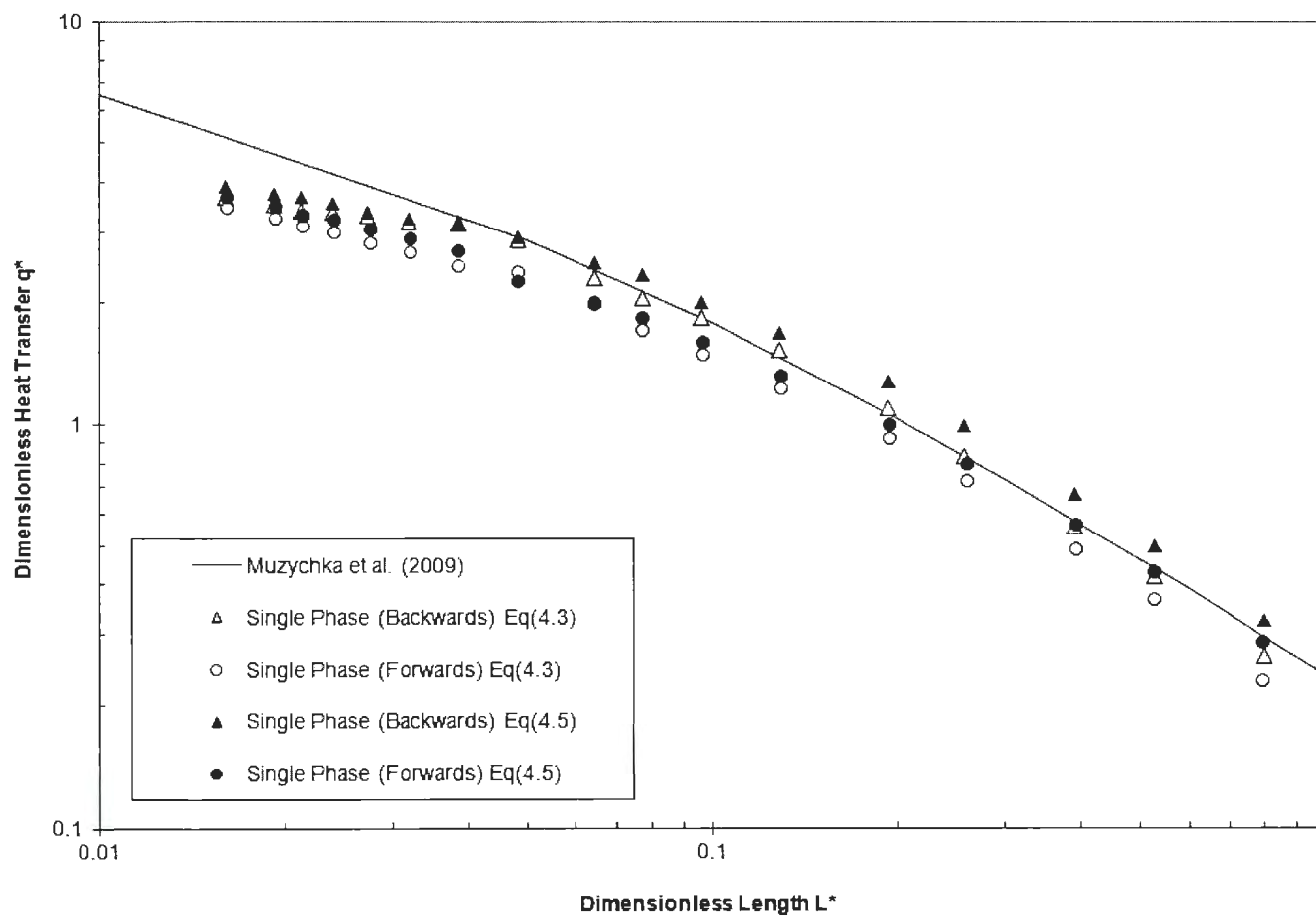


Figure 4.12 – Comparison of Flow Direction in Spiral Sink for Two-Phase Flow.

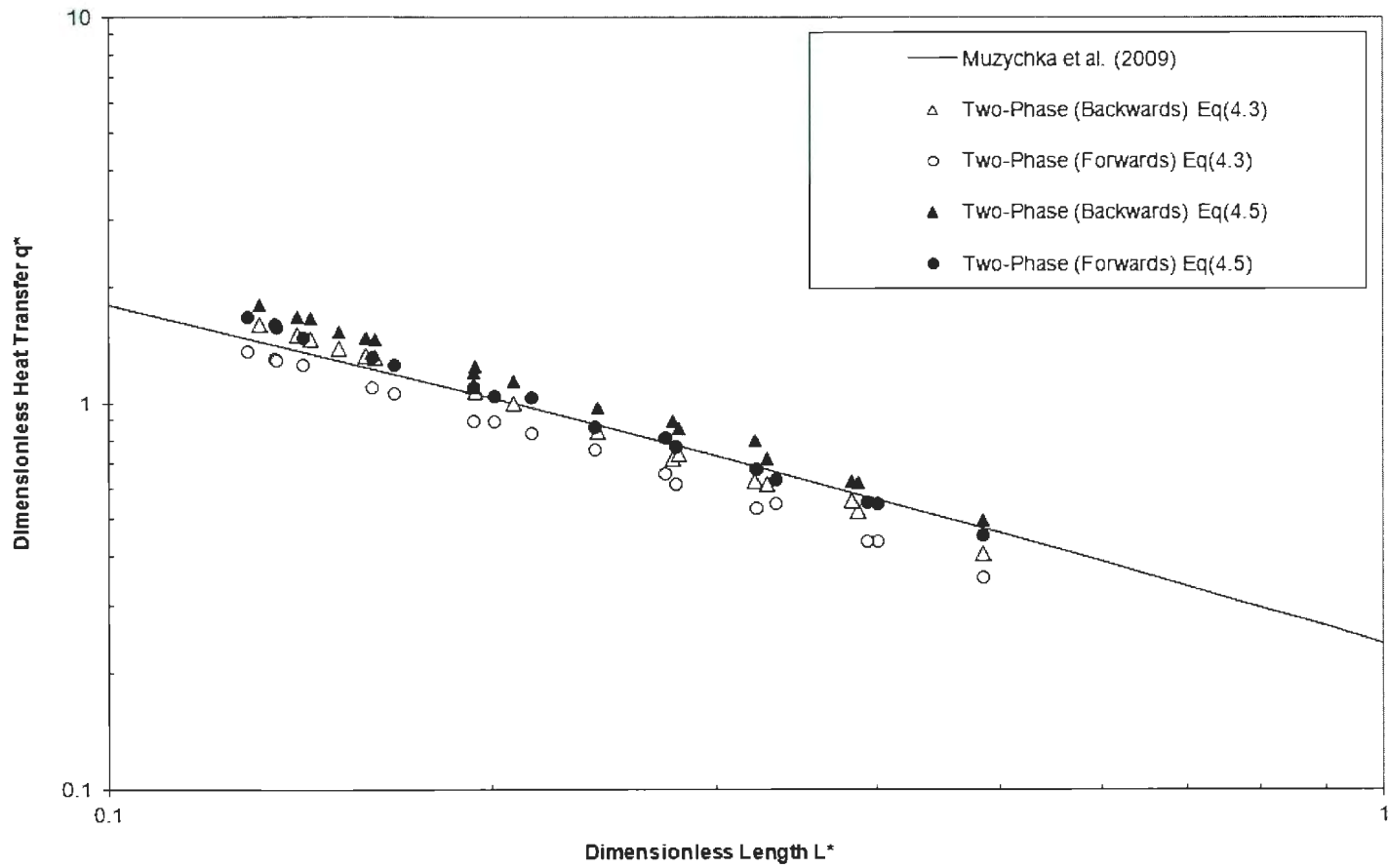


Figure 4.13 – Comparison of Single and Two-Phase Flow in the Square Sink.

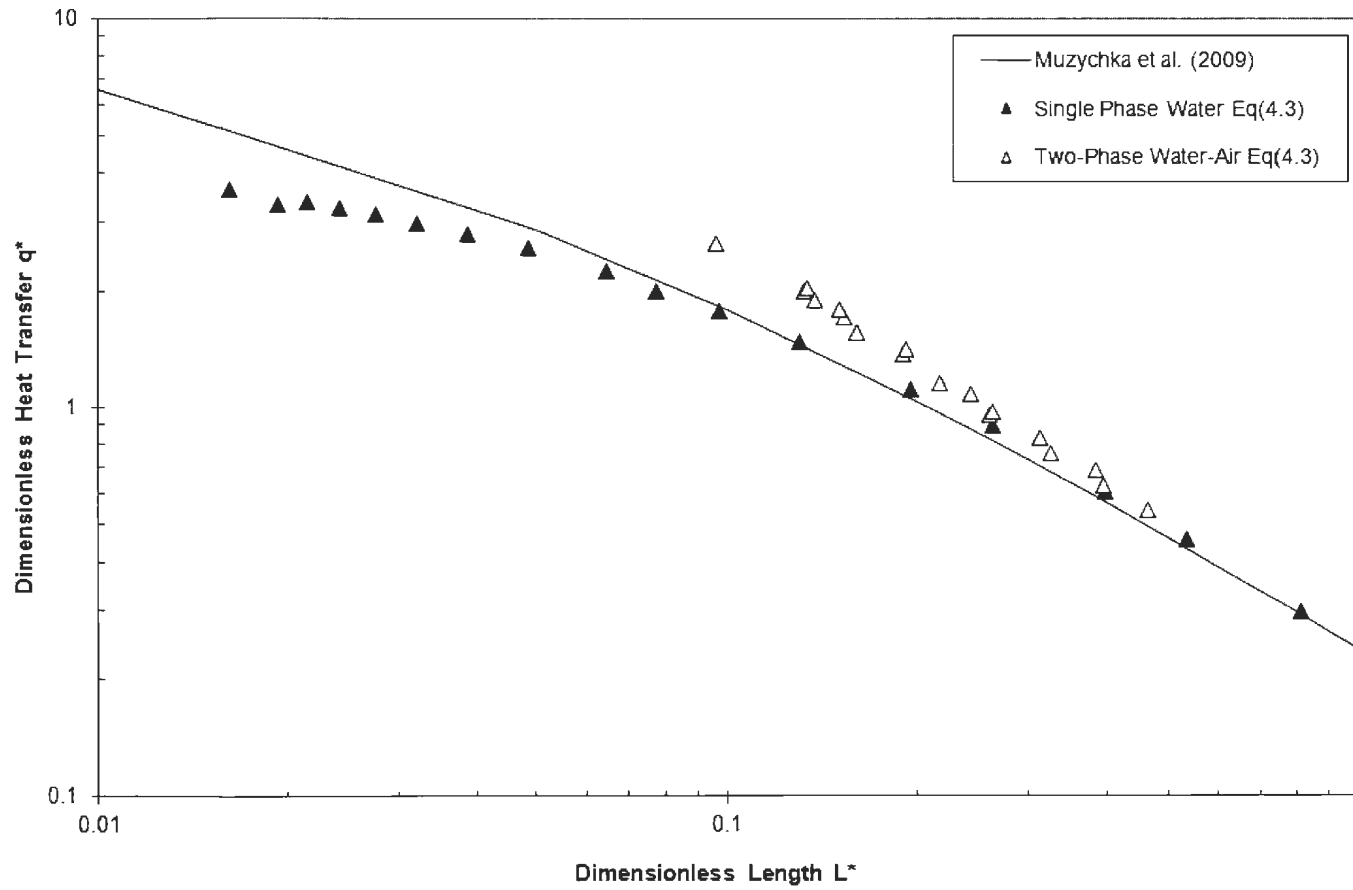


Figure 4.14 – Effect of Void Fraction on Dimensionless Heat Transfer in Square Sink.

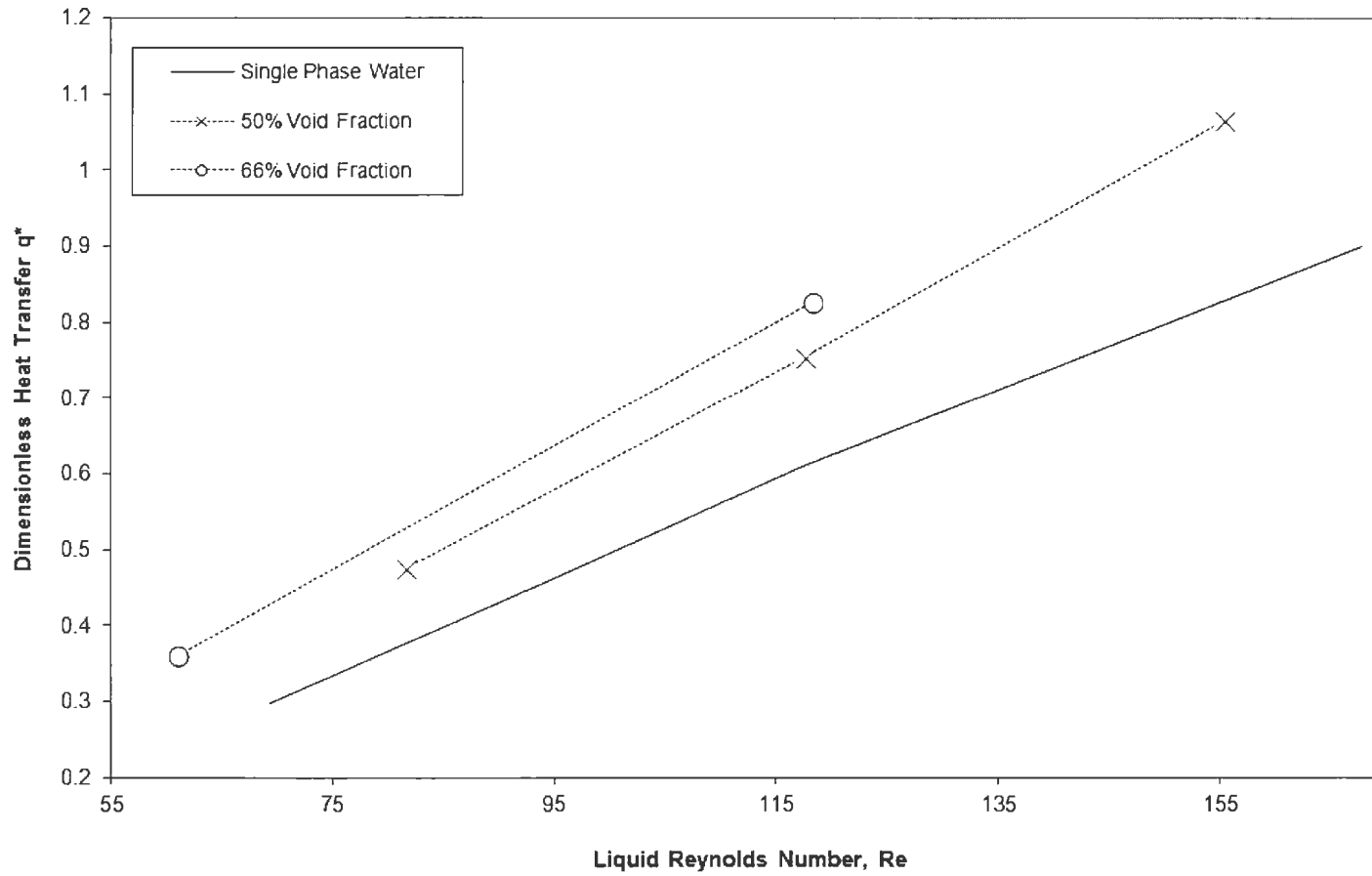


Figure 4.15 – Effect of Void Fraction on a Constant Liquid Flow Rate in Square Sink.

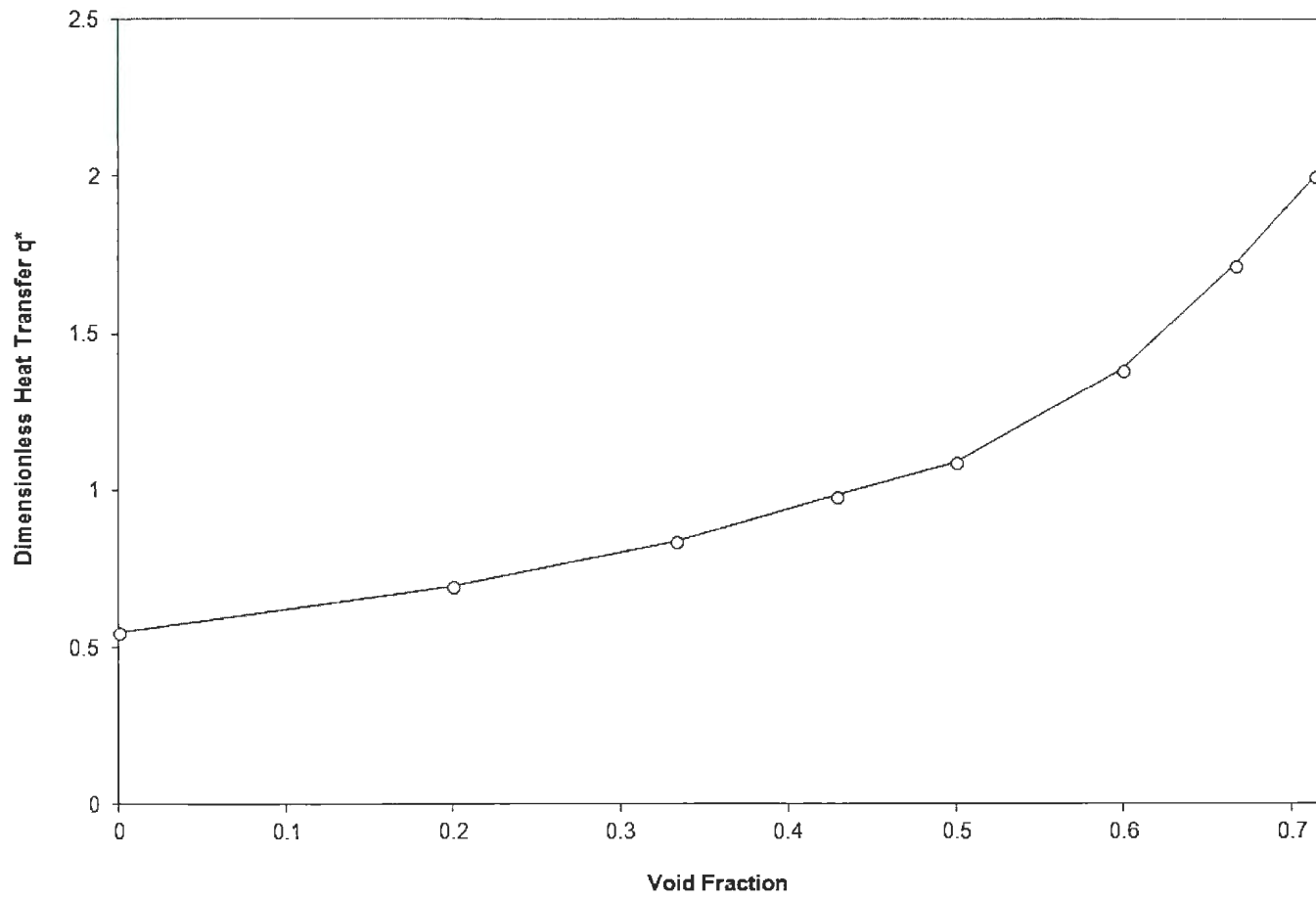


Figure 4.16 – Efficiency of Square Sink vs. Spiral Sink.

